

Data Fusion based Physical Layer Protocols for Cognitive Radio Applications

A Thesis

Submitted for the Degree of
Doctor of Philosophy
in the Faculty of Engineering

Submitted by
Venugopalakrishna Y. R.



Electrical Communication Engineering
Indian Institute of Science, Bangalore
Bangalore – 560 012 (INDIA)

June 2016

TO

My parents

Smt. C. R. Kamalamma and Sri. Y. C. Ramakrishnaiah

and

my grandparents

Acknowledgements

I begin by acknowledging the help and efforts of my supervisors, Prof. Chandra R. Murthy and Prof. D. Narayana Dutt. Prof. Murthy has guided and helped me in every step of my Ph.D. journey. From him, I have learnt the process of doing research, starting from problem formulation till writing papers. His signature research enterprise, the lab meeting, was instrumental in acquiring the knowledge of various research areas and tools in the paradigm of signal processing and wireless communications, apart from improving my presentation skills. He provided me ample opportunities to work on various industry collaboration projects and also offered financial assistance to attend conferences and workshops. Also, whenever he found me slow, he made sure that I catch the right pace. Prof. Dutt did all one can to prop up my self-confidence and enthusiasm. And, his suggestions during our individual meetings has helped in refining my research work. I am thankful to both Prof. Murthy and Prof. Dutt for all their support and encouragement.

Strong organizational support makes any task easy. It would have been hard to complete my Ph.D. without the support of course instructors, faculty of the dept., examiners of my comprehensive exam, staff of ECE dept., hostel and mess of IISc. I am grateful to all of them. Particularly, I am indebted to Prof. Neelesh B. Mehta and Prof. Manoj Verma for all the help.

I was fortunate to be part of the SPC Lab, because of my lab-mates: Bharath, Sanjeev, Deepa, Gana, Nanda, Krishna Chaythanya (KC), J. Chandrasekhar, Karthik Velugoori, Sowmya, Parthajit, Nissar, Srinivas, Ranjitha, Sneha, Abhay, Santhosh, Suma, Raghavendra Akula, Reuben, Anup, Manesh, Nirmal, Mohit, Saurabh, Geethu, Sinchu, Mishfad, Prashant, Harish, Vinnu, Vinuthna, Manoj, Vishnu, Satya, Karthik, Raksha, Raktim, Anuva, Govind, Pratikshya, Venkatesh, Chethan, Monika, Sai thoota, Shilpa,

Ribhu, Lekshmi, Sireesha, Ram, Ashok, Bala, Mohan, Namrata, Anjana and Kowshik. I thank them for all the help and for their comments and suggestions during lab meetings. In particular, I thank my collaborators Sneha, Harish, Dr. Prasant Misra, Dr. Jay Warrior and Namrata. And, I must acknowledge the help of my friends Sanjeev, Ranjitha, KC, Parthajit and Prem in measuring receive signal strengths of WiFi transmitters at various locations in football ground (under the hot sun). This helped in strengthening our work on communication footprint identification. The interactions with Srinivas, Bharath, Parthajit, Sanjeev, Abhay and Saurabh were very helpful in furthering my research. Also, Bharath helped me in the preparation of my comprehensive exam. I am thankful to Saurabh and Karthik Bharadwaj, my co-travelers for Globecom and ICC.

I must recount some extra-curricular activities. I enjoyed our chats during coffee breaks, as they offered some relaxation from the anxiety of achieving research goals. The main entertainers were Parthajit, Sanjeev, Bharath, Nanda, Abhay, Ranjitha and Nagesh. Our trips to Sambalpur, Hogenkal, Bettagere, Mangalore, Madhugiri, Devarayana Durga, and Makali Durga are memorable. Late evening chats with my hostel-mates Bharath, Prashanth, Srinidhi, Keshava, Sushrutha, Naveen, Sainath and Pradeepa were fruitful. The evening sanskrit classes by Sri. Ananda were delightful. Visits to Gokhale Institute of Public Affairs offered me solace, and my partner in crime was Sanjeev. Lately, I have enjoyed lunch sessions with Chethan, Monika, Ashok, Sai, Ribhu, Sireesha, Shilpa, Mohit and Saurabh. I thank all these friends who made these activities happen. Also, I am indebted to Sri. Shatavadhani Ganesh, Sri. Ramaswamy, Sri. Belagere Krishna Shastri, Sri. Mathoor Krishnamurthi, Sri. Gururaja Karajagi and many other scholars for their lectures and performances on various topics, which included Mankutimmana kagga, Avadhana, Upanishads, Yegdagella Aithe, Literature, Vidura-neeti, etc. Thanks to Parthajit and Sanjeev for enriching discussions on these topics.

I thank my parents Ramakrishnaiah, Kamalamma, wife Ashwini, sisters Jyothi, Hema, grandparents Chikkabelavangala Ramakrishnegowda, Jayamma, Yennegere Channagangaiyah, Revamma, niece Sadhana, nephew Amogha, and son Revantha (alias Chanakeshava) for their unconditional love and support. Finally, I am grateful to my uncles Thimmegowda, Muniraju, Krishnamurthy, aunts Siddagamma, Indiramma, Gangamma, Puttagowramma, Shashikala, brothers-in-law Girish, Manjunath, parents-in-law Appajigowda, Sowbhagya, and their families.

Abstract

This thesis proposes and analyzes data fusion algorithms that operate on the physical layer of a wireless sensor network, in the context of three applications of cognitive radios: 1. Cooperative spectrum sensing via binary consensus; 2. Multiple transmitter localization and communication footprint identification; 3. Target self-localization using beacon nodes.

For the first application, the problem of achieving binary consensus among a set of nodes using physical layer communication over noisy wireless links is considered. The channel state information (CSI) available at the nodes are imperfect due to practical estimation errors. Two schemes for updating the majority bit estimates at the nodes are contrasted: a linear minimum mean squared error (LMMSE) based scheme and a co-phased combining scheme. The evolution of network consensus is modeled as a Markov chain, and the average transition probability matrix (TPM) is analytically derived for the co-phased combining scheme, whereas, for LMMSE based scheme, the average TPM is computed through Monte Carlo simulations. The co-phased combining scheme is found to perform better at low to intermediate pilot SNRs, in addition to being analytically tractable and having lower computational complexity, compared to the LMMSE-based scheme. Also, to further characterize the consensus behavior, the probability of accurate consensus, the second eigenvalue of the TPM, the average hitting time to the first consensus state, and the average consensus duration are derived for the co-phased combining scheme. The power allocation between the pilot and data symbols is optimized, subject to a total power constraint. It is found that the optimal power allocation can lead to a significant improvement in the consensus performance. Monte Carlo simulation results validate the theoretical results, and provide insights into the complexity and performance trade-offs involved.

Next, the problem of whitespace identification is considered. Whitespace identification is a crucial step in the practical implementation of cognitive radios, where the problem is to determine the communication footprint of active primary transmitters in a given geographical area. To do this, a number of sensors are deployed at known locations chosen uniformly at random within the given area. The sensors' individual decisions regarding the presence or absence of a signal at their location is transmitted to a fusion center, which then combines the received information to construct the spatial spectral usage map. Under this model, several innovations are presented in this work to enable fast identification of the available whitespace. First, using the fact that a typical communication footprint map is a sparse image, two novel compressed sensing based reconstruction methods are proposed to reduce the number of transmissions required from the sensors compared to a round-robin querying scheme. Second, a new method based on a combination of the K -means algorithm and a circular fitting technique is proposed for determining the number of primary transmitters. Third, the design procedure to determine the power thresholds for signal detection at sensors is discussed. The proposed schemes are experimentally compared with the round-robin scheme in terms of the average error in footprint identification relative to the area under consideration. Simulation results illustrate the improved performance of the proposed schemes relative to the round-robin scheme.

Finally, an algorithm is proposed for self-localization of a target node using power measurements from beacon nodes transmitting from known locations. The geographical area is overlaid with a virtual grid, and the problem is treated as one of testing overlapping subsets of grid cells for the presence of the target node. The benefit of considering the problem in this framework is that it then becomes one of group testing, where, in each test, subsets of individuals (grid locations) are tested for the presence of defective individuals (targets). From the vast literature on group testing, a column matching algorithm is considered for devising the target localization algorithm. The average probability of localizing the target within a grid cell is derived using the tools from Poisson point processes and order statistics. This quantity is used to determine the minimum required node density to localize the target within a grid cell with high probability. The proposed design procedure is validated using the Monte Carlo simulations.

Glossary

AP	: Access Point
BLE	: Bluetooth Low Energy
cdf	: Cumulative Distribution Function
CH	: Calinski-Harbasz
COTS	: Commercial Off-the-shelf
CSI	: Channel State Information
CR	: Cognitive Radio
FC	: Fusion Center
FCC	: Federal Communications Commission
HSA	: Hierarchical Spectrum Access
i.i.d.	: Independent and Identically Distributed
ISM	: Industrial, Scientific and Medical
IoT	: Internet-of-Things
LMMSE	: Linear Minimum Mean Squared Error
LR	: Likelihood Ratio
LLR	: Log-Likelihood Ratio
M2M	: Machine-to-Machine
MC	: Markov Chain
MEC	: Minimum Enclosing Circle
ML	: Maximum Likelihood
MIMO	: Multiple-Input Multiple-Output
MSE	: Mean Squared Error
NGT	: Non-Adaptive Group Testing
NP	: Neyman Pearson
OMP	: Orthogonal Matching Pursuit
OSA	: Opportunistic Spectrum Access
pdf	: Probability Density Function
PMSE	: Program Making and Special Event
PPP	: Poisson Point Process
PU	: Primary User

r.v.	:	Random Variable
RF	:	Radio Frequency
RSS	:	Receive Signal Strength
SNR	:	Signal-to-Noise Ratio
SU	:	Secondary User
TPM	:	Transition Probability Matrix
UWB	:	Ultra-Wideband
WSD	:	White Space Device
WSN	:	Wireless Sensor Network
QoS	:	Quality of Service

Contents

Acknowledgements	i
Abstract	iii
Glossary	v
1 Introduction	1
1.1 Hierarchical Spectrum Access and Cognitive Radios	3
1.2 Spectrum Sensing	4
1.2.1 Cooperative Spectrum Sensing	5
1.3 Geo-location Database Approach	7
1.4 Contributions of the Thesis	9
1.5 List of Publications	11
2 Performance Analysis of Co-phased Combining for Achieving Binary Consensus over Fading Wireless Channels with Imperfect CSI	13
2.1 System Model and Problem Set-up	17
2.2 Majority Bit Detection	19
2.3 Performance Analysis	22
2.3.1 Probability of Detecting the Majority Bit	24
2.3.2 Average Transition Probability Matrix	26
2.3.3 Average Hitting Time	28
2.3.4 Average Consensus Duration	29
2.3.5 Data Power and Pilot Power Allocation	30
2.4 Simulation Results	31

2.5	Conclusions	39
3	Multiple Transmitter Localization and Communication Footprint Identification using Energy Measurements	43
3.1	Problem Setup	46
3.2	Proposed Transmitter Localization and Communication Footprint Identification Schemes	49
3.3	Design Issues	54
3.3.1	Estimation of the Number of Primary Transmitters	54
3.3.2	Sensor Detection Thresholds	54
3.4	Simulation Results	58
3.4.1	Monte-Carlo Simulations	58
3.4.2	Experimental Results	67
3.5	Conclusions	69
4	Target Self-Localization Using Beacon Nodes: A Column Matching Algorithm and Performance Analysis	71
4.1	System Model and Problem Setup	75
4.2	A Column Matching Algorithm for Localization	77
4.3	Performance Analysis	80
4.3.1	Probability of Localizing the Target within a Grid Cell	81
4.3.2	Optimal Beacon Density	88
4.4	Numerical Results	89
4.4.1	Monte Carlo Simulations	89
4.4.2	Experimental Results	94
4.5	Conclusion	95
5	Conclusion	98
A		103
A.1	Proof of Lemma 1	103
A.2	The Probability Density Function of the Difference of Two Nakagami Random Variables	104

A.3	Derivation of \bar{p}_l for the Co-phased Combining Scheme	106
A.4	Second Largest Eigenvalue of the Average TPM for $N = 3$ Sensors	107
A.5	Derivation of $\bar{p}^{(M)}$ and $\bar{p}^{(1)}$ for the Co-phased Combining Scheme	108
A.6	Proof that the Average Probability \bar{P}_{ij} is Strictly Positive	109
B		111
B.1	Approximate Mean Square Error in Localization	111
Bibliography		112

List of Figures

1.1	Distributed and cooperative spectrum sensing via consensus	7
1.2	Geolocation Database Approach	8
2.1	Illustration of the physical layer consensus protocol.	19
2.2	Second largest eigenvalue vs. Data SNR (denoted by SNR_d) for different pilot SNRs (denoted by SNR_p), with $N = 8$ nodes.	31
2.3	Average consensus duration vs. Data SNR, with $N = 8$, and for different pilot SNRs.	33
2.4	Average hitting time Vs. Data SNR, with $N = 8$, and for different pilot SNRs.	34
2.5	Probability of accurate consensus vs. number of consensus cycles, starting from an initial state of '00011111'.	36
2.6	Probability of accurate consensus vs. number of consensus cycles, for number of nodes, $N = 4, 15,$ and 22	37
2.7	Second largest eigenvalue vs. Data SNR for the co-phased combining scheme at a pilot SNR of 0 dB, when the sensors' self-bit is taken into account.	38
2.8	Average consensus duration vs. ratio of data power to pilot power under a total power constraint.	39
2.9	Average hitting time vs. ratio of data power to pilot power under a total power constraint.	40
2.10	Probability of accurate consensus vs. number of consensus cycles for the co-phased combining scheme when the path-loss between sensors is taken into account.	41

2.11	Probability of accurate consensus vs. number of consensus cycles for the co-phased combining scheme for an $N = 15$ sensor network which is not fully connected.	42
3.1	Primary footprint and alarming area in reconstruction schemes, <i>Scheme 1</i> and <i>Scheme 2</i>	51
3.2	Identification of number of clusters using CH, Hartigan and proposed methods	59
3.3	Comparison of the round-robin scheme, <i>Scheme 1</i> and <i>Scheme 2</i> , considering (a) the path loss model and (b) a combined path loss and log-normal shadowing model	61
3.4	Percentage success of support recovery for ℓ_1 and OMP based CS reconstruction Vs. number of transmission instants (M) for different values of the SNR per sensor	62
3.5	Aerial view of the football field showing the placement of Wi-Fi AP . . .	68
4.1	Illustration of the measurement process for target sensor localization. . .	78
4.2	Illustration of the beacon power contours intersecting line segment \mathcal{S} . .	80
4.3	Depiction of the intersections on line segment \mathcal{S} as uniform ordered variates and their spacings.	83
4.4	Illustration of the multiple power contours from beacons intersecting line segment \mathcal{S}	86
4.5	Product of the node density and beacon radius required to localize the target within a grid cell with probability 0.9 vs beacon radius for various dimensions of grid cell, when the target node employs single power threshold.	90
4.6	Node density required to localize the target within a grid cell with probability p vs the grid cell size, when the beacon node employs $M = 5$ threshold intervals.	91
4.7	Probability of localizing the target within a grid cell vs product of the node density and number of threshold intervals.	92

4.8	MSE in localization vs number of beacon nodes for different power levels on a 10×10 grid, with each grid cell of area 1 m^2 . The dimensions of area of interest \mathcal{A} is $10\text{m} \times 10\text{m}$	93
4.9	Depiction of the experimental setup, with beacon nodes placed along the boundary of the room.	95
4.10	MSE in localization vs number of beacon nodes for experimental setup.	96

List of Tables

3.1	Algorithm for estimating the number of transmitters	55
3.2	Evaluation of the threshold selection procedure when all $T_{max} = 4$ transmitters are emitting at $P_{max} = -1dBm$ power	64
3.3	Evaluation of the threshold selection procedure when $T_{max} = 4$ transmitters are emitting powers drawn from $\mathcal{U}(P_{min}, P_{max})$	65
3.4	Percentage success of support recovery for OMP based CS reconstruction in presence of synchronization errors for <i>Scheme 1</i> , with $L = 960$	66
3.5	Percentage success of support recovery for OMP based CS reconstruction in presence of synchronization errors for <i>Scheme 2</i> , with $L = 960$	67
3.6	Evaluation of threshold selection procedure with experimental data	69
4.1	Localization accuracy to within 1, 2, or 3 or more grid cells for various combinations of number of beacon nodes, K , and number of power levels per beacon node, M	94

Chapter 1

Introduction

The wireless radio spectrum is the primary infrastructure for various communication services like television and radio broadcasting, mobile and data communication, satellite communication, military applications, air-traffic control, emergency services, etc. Dedicated frequencies are allocated to these services to ensure that they do not interfere with each other, thereby ensuring good quality of service (QoS). However, in the last decade, fueled by market demand for multimedia services and rapid advancement in the device technology, the QoS requirement has increased many-fold in most of these sectors. For example, there is a demand for higher data rates in television broadcasting due to the high definition video technology. The demand for mobile data services has also exploded, far exceeding most predictions. It is estimated that, because of the proliferation of smart phones and Wi-Fi devices, the demand for mobile and wireless data services will grow by a factor of over 80 times, between 2012 and 2030 [1]. Although transmission techniques like multiple-input and multiple-output (MIMO), enhanced modulation and coding, coordinated multi-point transmission, small-cells, and

carrier aggregation can enhance the data rate, they are limited by factors like interference, hardware requirements, etc. Thus, the increasing data rate requirement can only be met by allocating larger bandwidth to a given sector. Also, the future need of bandwidth for emerging services like machine-to-machine (M2M) communication and Internet-of-Things (IoT), adds to the burden of the scarce spectrum. Therefore, it is essential to utilize and reuse the spectrum efficiently to meet the ever-increasing demand for data and related services.

The dedicated allotment of frequencies to different services is fundamentally inefficient, because, practically, the spectrum is not used at all times and at all locations by any one service [2]. Sharing the same frequency among various services in time and space would alleviate this problem. One of the most successful example of spectrum sharing is Wi-Fi on 2.4 GHz and 5 GHz industrial, scientific and medical (ISM) radio bands. In Wi-Fi, the access points (APs) use a detect-and-avoid mechanism before occupying a frequency sub-band, and the devices use a listen-before-speak approach to communicate. This happens over the unlicensed ISM bands using network layer protocols in a homogeneous environment, where all the devices are cooperating. However, replicating the same over the rest of the spectrum where bulk of the band is licensed and heterogeneous is quite a challenge. To this end, the hierarchical spectrum access [3] envisioned as part of cognitive radios by Joseph Mitola [4,5], is the future of spectrum sharing.

1.1 Hierarchical Spectrum Access and Cognitive Radios

The hierarchical spectrum access (HSA) model categorizes the licensed users and the unlicensed spectrum seekers as primary users (PU) and secondary users (SU), respectively. The secondary users are cognitive radios (CR), which are conceptualized as context-aware, autonomously reconfigurable intelligent radios, capable of adapting to the communication environment through learning. To share the spectrum, CRs must communicate by limiting their interference to the incumbent (primary) receivers. In [6], it was suggested that the CRs can opportunistically access a frequency band from a spectrum pool when primary users are absent. To do that, CRs should actively look for *spectrum holes* temporally and spatially. This is also known as *white space* detection. Another spectrum sharing paradigm under the HSA model is the underlay approach, where the CR users coexist with primary users by employing spread spectrum techniques [7] or ultra-wideband (UWB) [8] transmissions under the noise floor of primary receivers. The authors in [9] consider an improved underlay system by avoiding interference to the primary users. The CRs adapt their UWB transmissions by notching or suppressing their signals in the incumbent narrow-bands [10–13]. Again, this also involves detecting the occupancy of spectrum. Consequently, the task of finding the spectrum holes is an important block in CRs to enable opportunistic spectrum access (OSA) and spectrum underlay with interference avoidance. This has spiraled research in the area of *spectrum sensing*, which falls under the detection theory framework [14]. Also, to start with, the spectrum regulators have chosen a geo-location database based approach to enable CR operation in TV white spaces [15]. These topics are discussed in the next two sections.

1.2 Spectrum Sensing

The problem of detecting the presence or absence of PU is, at its core, a binary hypothesis testing problem. The received signal at the n^{th} time instant $y[n]$ under the two hypotheses is given by

$$\begin{aligned} H_0 : \quad & y[n] = w[n], \quad n = 1, 2, \dots, N, \\ H_1 : \quad & y[n] = x[n] + w[n], \quad n = 1, 2, \dots, N, \end{aligned} \quad (1.1)$$

where $x[n]$ is PU signal at the CR and $w[n]$ is the receiver noise, assumed independent and identically distributed (i.i.d.) as $\mathcal{CN}(0, \sigma^2)$. Under both the Neyman Pearson (NP) framework and Bayesian framework [14], the test statistic $\Lambda(\mathbf{y})$ is the likelihood ratio (LR), $\frac{\Pr(\mathbf{y}|H_1)}{\Pr(\mathbf{y}|H_0)}$, where $\mathbf{y} \triangleq [y[1] \ y[2] \ \dots \ y[N]]$. The test statistic is compared with a threshold η to decide between hypotheses H_0 and H_1 . The probability of detection, $P_D = \Pr(\Lambda(\mathbf{y}) \geq \eta | H_1)$, and the probability of false alarm, $P_{FA} = \Pr(\Lambda(\mathbf{y}) \geq \eta | H_0)$, are the key performance metrics of interest. In the literature, various (sub-optimal, but computationally efficient) sensing techniques like the energy detector, cyclo-stationary feature based detector and matched filter detector have been considered [16–19]. An energy detector [20, 21] compares measured energy in a finite interval $\sum_{i=1}^N (y[i])^2$ to the threshold η . The choice of η depends on the noise variance σ^2 . It has been shown that, the energy detector is asymptotically optimal when the symbols are i.i.d. and the probability density functions under both hypotheses are known [22, 23]. But, under noise variance uncertainty, the energy detector suffers from the so-called SNR wall

problem [24], i.e., there exists a lower limit on the detection SNR below which reliable detection is not possible, even if infinitely many samples are available. However, in practice, structure in the modulated symbols in the form of pilot signals, spreading codes, cyclic prefixes in OFDM, etc. can be exploited to circumvent the problem of SNR wall. This structure in the primary signals is exploited in auto-correlation function based detectors [25,26] and cyclo-stationary feature based detectors [18,27,28]. On the other hand, if the PU signal \mathbf{x} is perfectly known at the secondary detector, the output of the matched filter $Re[\mathbf{x}^H \mathbf{y}]$ is the test static, but this requires perfect timing and frequency synchronization with the PU transmitter. All these local sensing schemes require the CR receivers to be of high sensitivity compared to PU receivers, as they are based on sensing the PU transmitters, and not the PU receivers. This is a difficult requirement, as it is challenging to design wideband radios with high sensitivity. Due to this, the local sensing schemes suffer from what is known as the *hidden terminal problem*, where a CR may not detect the PU transmitter as the PU signal may be in a deep fade, but the CR's transmissions may not be blocked from the PU receiver. Cooperative decision making by a group of spatially distributed sensors offers the benefit of diversity, making it robust to the hidden terminal problem.

1.2.1 Cooperative Spectrum Sensing

In the paradigm of decentralized detection based cooperative sensing, a central node makes a unified decision by fusing the data from local sensors, and then broadcasts the decision back to the sensors. The data fusion is primarily carried out in two ways: soft combining and hard combining. In soft combining schemes, the sensors report their

individual log-likelihood ratios (LLRs) to the central node, where the sum of LLRs is used as the decision variable. Due to the energy constraints on the CR nodes, sending the real-valued, full-precision LLRs to the central node may be expensive. Thus, in hard combining, binary decisions are reported by local sensors, which are combined at the central node using a k -out-of- L rule, i.e., if at least k out of L sensors report a 1, then the PU is declared to be present. The cases of $k = 1$, $k = L$, and $k = \lceil L/2 \rceil$ are called as the OR rule, AND rule, and majority rule, respectively. When energy detection is employed at the local sensors, the majority rule turns out to be optimal in terms of probability of error, when the local P_{FA} is of the order of $1 - P_D$, whereas the AND rule is optimal when $P_{FA} \gg 1 - P_D$, and the OR rule is optimal in the $P_{FA} \ll 1 - P_D$ regime [29]. Hence, the majority rule is optimal in terms of CR network throughput in the desirable P_D range [30], and is shown to be robust to reporting channel errors [31].

Unlike the central node-based schemes described above, in distributed schemes, the L sensors converge to a consensus decision by repeated exchange of data among themselves. As depicted in Fig. 1.1, the L nodes sense a given frequency band to arrive at a local binary decision, and then they employ a consensus mechanism on a low-rate control channel to ascertain the presence of primary. If the frequency band is found free, L nodes form a secondary network on that band, otherwise they carry out the same procedure on another frequency band. The study of one such majority rule based distributed consensus scheme is a focus area of this thesis.

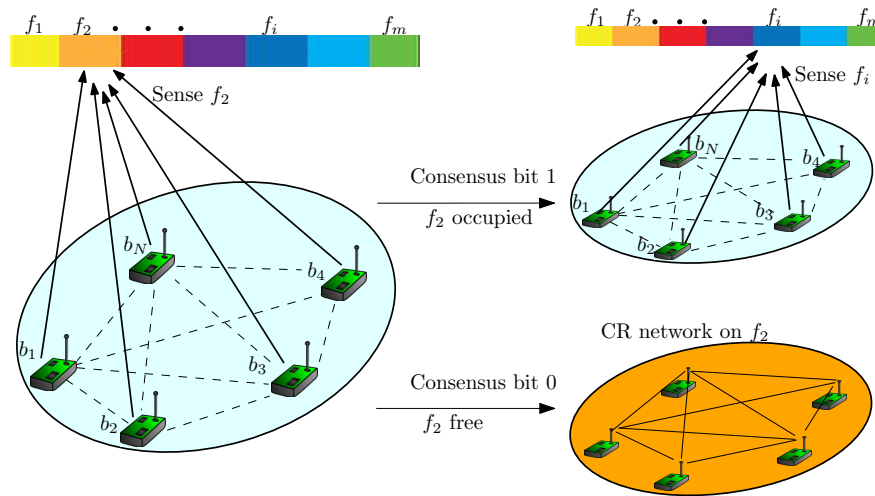


Figure 1.1: Distributed and cooperative spectrum sensing via consensus

1.3 Geo-location Database Approach

Universally, the VHF and UHF bands of the radio spectrum are allocated to terrestrial TV broadcasting because of their good propagation characteristics. In the USA, it was found that the terrestrial TV bands were, in reality, highly under utilized [2]. Hence, the Federal Communications Commission (FCC) has allowed unlicensed devices with geo-location capability to access the TV spectrum. These devices are required to use central databases to regulate the interference caused by them [32, 33]. This is done as follows. First, the spectrum-seeking white space device (WSD) communicates its location to the database. The database determines the allowable frequency bands and maximum transmit powers, and returns this information to the WSD. This process is pictorially shown in Fig. 1.2. The trials of this approach have been carried out to provide services like low cost broadband and public hot spots in the city of Wilmington, North Carolina, and for smart grids in Plumas County, California [33]. Similarly, Of-com in the UK has allowed the use of TV white spaces in the UHF band in 2014 [34].

In India, terrestrial TV white spaces are abundantly available as satellite TV is the primary means of broadcasting, and deployment of a test bed has been planned to provide broadband in rural areas of Palghar district of Maharashtra [35,36].

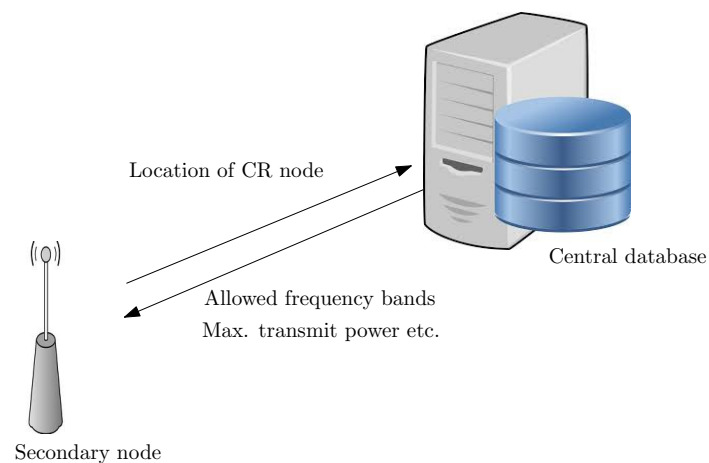


Figure 1.2: Geolocation Database Approach

Two important problems in this approach are localization of the WSDs, and the creation and maintenance of the database. The database should contain the information like TV station coordinates, their transmit powers, information about wireless microphone devices and program making and special event (PMSE) devices, their locations and time of usage, etc. To start with, FCC and Ofcom have placed a requirement on the frequency of database update as once in a day and every 2 hours, respectively. As a next step, Ofcom is aiming at WSDs that can avoid interference to other CRs along with PUs. It is planning to extend the geo-databases to a wide range of frequencies [1,34]. Therefore, in the long term, to extend the functionality of databases to facilitate mobility, better coordination among users, and improvement in QoS, it is important to create and maintain accurate and up-to-date databases. Thus, another focus area of this thesis is that of identifying the communication footprint of primary users.

Further, as mentioned earlier, the WSD needs to convey its location to the central database. In the absence of global positioning system (GPS), for example, in indoor environments, or when GPS capability is unavailable at the receiver, one can rely on the already available infrastructure for localizing the WSD. For e.g., in a fully-networked city, a set of cellular base-stations or the Wi-fi access points can be used to enable localization. Thus, this thesis considers an infrastructure based localization of WSDs using receive signal strength measurements. The contributions of the thesis are discussed in detail in the next section.

1.4 Contributions of the Thesis

This thesis develops novel physical layer algorithms for the following three applications of CR:

- A1. Cooperative sensing through physical layer binary consensus.
- A2. Efficient identification of the primary communication footprint.
- A3. Network assisted self-localization of CRs or WSDs.

The problem setup for applications A1-A3 consists of a set of sensors deployed uniformly at random locations in a geographical area. In case of A1 and A2, the sensors locally detect the presence or absence of the primary and employ binary signaling to transmit their local binary decisions to the other nodes or to a central node, respectively. For A3, where the goal is self-localization of target, these sensors are used as beacon transmitters. The transmissions by the beacon nodes are carried out on a noisy control channel. The signals received at the WSD from the beacon nodes is used for

self-localization of the WSD. The key contributions of the thesis in the three problem areas A1-A3 are elaborated upon in the following paragraphs.

In Chapter 2, the problem of achieving binary consensus among a set of wireless nodes using physical layer protocols is considered. A co-phased combining based scheme is studied under imperfect channel state information at the nodes due to practical estimation errors. The evolution of network consensus is modeled as a Markov chain, and the average transition probability matrix (TPM) is analytically derived for the co-phased combining scheme. The average hitting time to the consensus state and average consensus duration are derived, and the average stopping time of the consensus procedure is characterized. Also, the power allocation between the pilot and data symbols is optimized, subject to a total power constraint. It is found that optimizing power allocation significantly improves the consensus performance compared to naïve allocation schemes. The co-phased combining scheme is compared with a linear minimum mean squared error (LMMSE) based scheme in terms of the probability of accurate consensus, the second largest eigen value of the TPM, the average hitting time and the average consensus duration. The co-phased combining scheme is found to perform better at low-to-intermediate pilot SNRs compared to the LMMSE-based scheme.

The focus of Chapter 3 is the problem of spectrum cartography using 1-bit decisions from sensors deployed in a geographical area. Using the fact that a typical communication footprint is a sparse image, two novel compressed sensing based reconstruction methods are proposed to reduce the number of transmissions required from the sensors compared to a round-robin querying scheme. Second, a new method based on a combination of the K-means algorithm and a circular fitting technique is proposed for

determining the number of primary transmitters. Third, a design procedure to determine the power thresholds for signal detection at sensors is proposed. The proposed schemes are experimentally compared with the round-robin scheme in terms of the average error in footprint identification relative to the area under consideration. Simulation results illustrate the improved performance of the proposed schemes compared to the round-robin scheme.

In Chapter 4, an algorithm is proposed for self-localization of a target node using power measurements from beacon nodes transmitting from known locations. The geographical area is overlaid with a virtual grid, and the problem is treated as one of testing overlapping subsets of grid cells for the presence of the target node. The proposed algorithm is validated both by Monte Carlo simulations as well as using experimental data collected from commercially-off-the-shelf bluetooth low energy (BLE) beacon nodes.

1.5 List of Publications

1. Journal Publications

- (a) Venugopalakrishna Y. R., C. R. Murthy, and D. N. Dutt, "Multiple Transmitter Localization and Communication Footprint Identification using Energy Measurements," *Elsevier Physical Communication, Special Issue on Cognitive Radio*, vol.9, pp. 184–192, Dec. 2013.
- (b) Venugopalakrishna Y. R. and C. R. Murthy, "Performance Analysis of Co-phased Combining for Achieving Binary Consensus over Fading Wireless Channels with Imperfect CSI," *IEEE Trans. Signal Proc.*, vol.64, pp. 3262–3273, June 2016.

- (c) Venugopalakrishna Y. R. and C. R. Murthy, "Target Self-Localization Using Beacon Nodes: A Column Matching Algorithm and Performance Analysis," *submitted, IEEE Trans. Veh. Technol.*, June 2016.

2. Conference Publications

- (a) Venugopalakrishna Y. R., C. R. Murthy, D. N. Dutt and S. L. Kottapalli, "Multiple Transmitter Localization and Communication Footprint Identification Using Sparse Reconstruction Techniques," *Proc. IEEE Int. Conf. Commun.*, Kyoto, Jun. 2011.
- (b) Venugopalakrishna Y. R. and C. R. Murthy, "Physical Layer Binary Consensus Over Fading Wireless Channels and With Imperfect CSI," *Proc. IEEE Global Commun. Conf.*, Austin, Dec. 2014.
- (c) Venugopalakrishna Y. R., C. R. Murthy, P. Misra, and J. Warrior, "A Column Matching Based Algorithm for Target Self-localization Using Beacon Nodes", *Proc. ACM/IEEE International Conference on Information Processing in Sensor Networks*, Apr. 2015.

Chapter 2

Performance Analysis of Co-phased Combining for Achieving Binary Consensus over Fading Wireless Channels with Imperfect CSI

This work considers the problem of achieving binary consensus among a set of nodes, where, starting with an initial binary value, the nodes exchange messages, with the goal of agreeing upon the majority value among them. Majority consensus has many applications, for example, in cooperative spectrum sensing in cognitive radios [37, 38] and throughput optimization in sensor networks [30]. The classical approach to achieving consensus considers error-free exchange of data between neighboring nodes in the form of packets. In wireless sensor networks (WSNs), one can avoid the control information overhead required for a packet [39] by broadcasting the binary symbols over the wireless medium. This constitutes achieving binary consensus in the physical layer itself. However, the estimation of the fading channel and the errors due to the noise at the receiver lead to a new set of challenges in achieving accurate consensus, due to the

unreliable communication between the nodes. In this context, our goal in this chapter is to study the performance of binary consensus protocols that involve bit exchanges among the nodes over fading wireless channels, when the channel state information (CSI) at the nodes is imperfect.

Most of the existing literature on consensus problems, starting from the thesis of Tsitsiklis [40] to the more recent studies involving gossip algorithms [41–47], is mainly concerned with distributed averaging. Here, the nodes attain consensus by repeatedly computing a weighted average of the values of their neighbors. This requires nodes to exchange real-valued estimates. On the other hand, several recent studies have also considered the transmission of quantized states to the neighbors and then attaining the average quantized consensus state [48–57]. However, all of these works consider message exchange over the network layer of the protocol stack. In contrast, the idea of achieving binary consensus over the physical layer itself has only been explored more recently [58–63]. The exchange of a real-valued test statistic over fading channels to arrive at consensus on the global average was considered in [54,58–60], with the goal of performing distributed hypothesis testing. In [61–63], the authors considered a scheme where the nodes iteratively broadcast their majority-bit estimates over a noisy channel in a round-robin manner and update their majority-bit estimates using the received signals, to achieve consensus among the nodes. Further, this scheme has been extended to networks with link failures in [63]. However, these studies assumed perfect CSI to be available at the nodes, which is impractical in low power sensor network applications.

In [61], the authors consider an AWGN channel, and use a sum of votes estimator at every node to detect the majority bit. The evolution of the network state is modeled as

a Markov chain, and the second largest eigenvalue of its transition probability matrix is used to characterize the consensus behavior. A key finding of this work is that the network asymptotically loses memory of the initial state. However, in the transient period, the network can be in accurate consensus with high probability and can stay in consensus for a long duration.

In [63], the authors studied binary consensus with i.i.d. fading channels between the nodes. A linear MMSE (LMMSE) estimator was proposed for updating the sum of votes at the nodes as a weighted combination of the received samples. The weights are computed based on the channel magnitudes, which were assumed to be perfectly known at the nodes. An alternative way to estimate sum of votes is to simply compute the sum of the co-phased received samples (akin to equal gain combining). To estimate the sum of votes, which is a key quantity in determining the majority bit update at the nodes, the physical layer protocols considered in this work and related literature are based on spatial diversity combining, of which, LMMSE-based scheme and co-phased combining scheme are robust across a wide range of SNRs. Other techniques, namely, maximum ratio combining and selective gain combining are not suitable under non-identical inputs [64]. Thus, the two schemes considered, the LMMSE-based scheme and the co-phased combining are the relevant protocols in the scope of this work. Furthermore, in the context of decentralized detection, the co-phased combining scheme is known to be robust to channel estimation errors [64].

In this work, we study the efficacy of the two aforementioned options for achieving binary consensus over i.i.d. fading channels. Specifically, and for the first time in the literature to the best of our knowledge, our analysis accounts for the effect of channel

estimation errors on physical layer consensus protocols. Further, while the analysis in [63] focused on the second largest eigenvalue of the average transition probability matrix (TPM) of the Markov chain, we analyze metrics that are more directly related to the consensus performance, such as the probability of detecting the correct majority bit, the time to reach first consensus, and the average consensus duration, all for the co-phased combining scheme. In addition, we study the allocation of power between the pilot and data symbols, under a total power constraint, to optimize the consensus performance. We also study the performance of the co-phased combining scheme when the network is not fully connected.

Our key findings are as follows. The co-phased combining scheme is simple from an implementation perspective, and also makes the average probability of detecting the correct majority bit analytically tractable. The latter is necessary for computing the average TPM of the Markov chain. The second largest eigenvalue of the TPM governs the consensus behavior of the underlying protocol. We also characterize the average hitting time and the average consensus duration, which jointly determine the time required for the network to achieve consensus with high probability. We also find that, while the co-phased combining scheme is simpler than the LMMSE scheme, somewhat surprisingly, it offers better performance at low to moderate SNRs. This is due to its lesser dependence on the channel estimates, which makes it a robust scheme in the presence of errors in estimation. Finally, we find that optimizing the power allocation between pilot and data symbols is important, as it can lead to a significant improvement in the consensus performance compared to naïve allocation schemes.

The rest of the chapter is organized as follows. We discuss the problem setup and

system model in the next section. We present the update rules employed after the bit exchange in Sec. 2.2. In Sec. 2.3, we derive the average probability of majority bit detection, average consensus duration and average hitting time for the proposed co-phased combining based scheme. In Sec. 2.4, we provide simulation results comparing the proposed and the existing consensus protocols. We conclude the chapter in Sec. 2.5.

Notation: In this chapter, we use boldface capital letters to denote matrices and boldface small letters to denote vectors. We use $(.)^T$ to denote the transpose of a matrix. The function $f_H(h)$ represents the probability density function (pdf) of a random variable H , and h denotes its realization.

2.1 System Model and Problem Set-up

Our setup consists of a fully-connected network with N nodes, with the nodes denoted by $\mathcal{S} \triangleq \{s_1, s_2, \dots, s_N\}$. Each node starts with an initial binary data bit $b_l(0) \in \{0, 1\}$, $l = 1, \dots, N$. The goal is for the nodes to achieve consensus on the bit value corresponding to the majority of their initial values. To this end, nodes broadcast their data bit in a round-robin manner over noisy fading channels. Then, nodes utilize the received signals to detect and update a local majority bit estimate. This process is repeated over multiple cycles, as consensus may not be attained in a single cycle of bit exchange and bit update due to the noisy communication between the nodes. The physical layer protocol considered in this work is schematically illustrated in Fig. 2.1.

In the t^{th} update cycle, node $s_k \in \mathcal{S}$ broadcasts a known pilot symbol followed by its current majority bit estimate, denoted by $b_k(t-1)$. This is received by the other $N-1$ nodes $s_l \in \mathcal{S} \setminus \{s_k\}$. The wireless channel from s_k to s_l , denoted by $h_{kl} \triangleq |h_{kl}|e^{j\theta_{kl}}$, is

assumed to be Gaussian $\mathcal{CN}(0, \sigma^2)$ distributed, remain constant over a given update cycle, and vary in an i.i.d. fashion across the nodes and across update cycles. We note that the consensus protocols considered in the sequel are directly applicable to non-i.i.d. fading channels. The performance the analysis can also be extended to the non-i.i.d. case, by using the techniques in recent work in the context of the outage analysis of relay selection schemes [65,66]. However, in the sequel, we restrict to the i.i.d. model for simplicity of exposition and because it is sufficient to bring out the critical importance of the system parameter settings, for example, the power allocation for the pilot and data symbols, on the performance of physical layer consensus protocols. The node s_l estimates the channel h_{kl} using the received pilot symbol

$$y_{kl}^{(p)} = h_{kl}\sqrt{E_p} + w_{kl}^{(p)}, \quad (2.1)$$

where E_p is the pilot power and $w_{kl}^{(p)} \sim \mathcal{CN}(0, \sigma_w^2)$ is the circularly symmetric complex additive white Gaussian noise at the receiver¹, with zero mean and variance σ_w^2 . The maximum likelihood estimate of the channel is given by $\hat{h}_{kl} = h_{kl} + w_{kl}^{(p)}/\sqrt{E_p}$. With BPSK signaling employed for broadcasting the data bits, the received signal at s_l is given by

$$y_{kl}^{(d)} = h_{kl}x_k\sqrt{E_d} + w_{kl}^{(d)}, \text{ where } x_k = 2b_k(t-1) - 1$$

and E_d is the data power and $w_{kl}^{(d)} \sim \mathcal{CN}(0, \sigma_w^2)$. At the end of a cycle, s_l has $N-1$ data samples $\{y_{kl}^{(d)}\}$ and corresponding channel estimates $\{\hat{h}_{kl}\}$, $k = 1, 2, \dots, N, k \neq l$. These samples are used to find the bit-update of the t^{th} cycle. The majority-bit update rules

¹The distance dependent effects can be accounted in the analysis by zero forcing the path loss factor at the receiver. This can be realized by substituting the noise variance term σ_w^2 with $\sigma_w^2 d_{kl}^\eta$ throughout the analysis. Here, d_{kl} is the distance between the sensor nodes s_k and s_l and η is the path loss exponent.

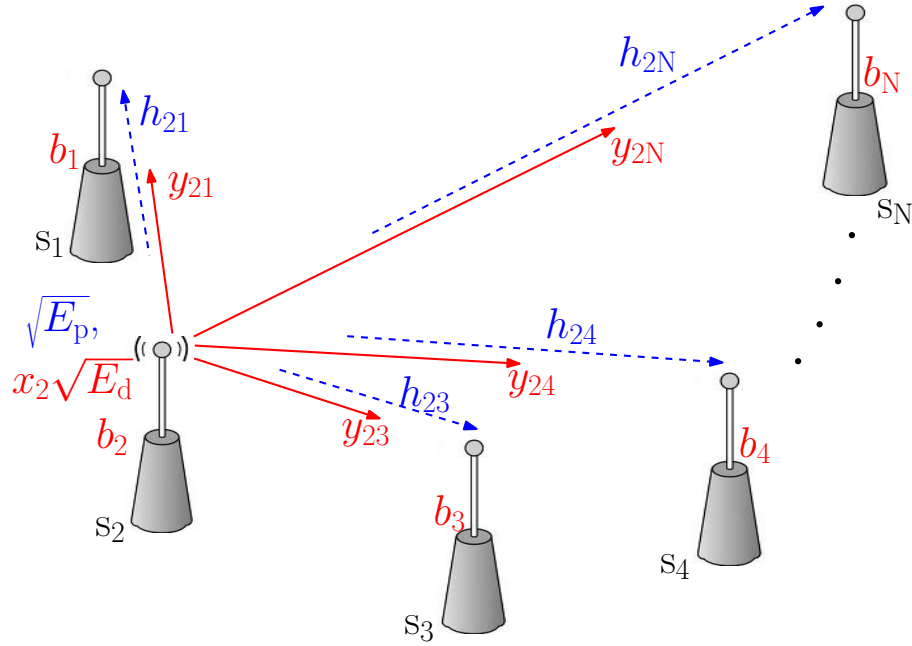


Figure 2.1: Illustration of the physical layer consensus protocol. Node s_2 broadcasts a pilot symbol followed by a BPSK data symbol $x_2 \in \{-1, +1\}$. In each bit-exchange cycle, all nodes employ the same mechanism, in a round-robin manner.

considered in this work are discussed in the next section. This is followed by a rigorous theoretical analysis of the consensus procedure.

2.2 Majority Bit Detection

In this section, we discuss the bit-update procedure at each node s_l . First, the received data $y_{kl}^{(d)}$ is pre-processed using an estimate of the phase of the channel h_{kl} , as follows:

$$r_{kl} = \text{Re}\{y_{kl}^{(d)} e^{-j\hat{\theta}_{kl}}\}, \quad k \in \{1, 2, \dots, N\}, \quad k \neq l,$$

$$r_{kl} = |h_{kl}| \cos \tilde{\theta}_{kl} x_k \sqrt{E_d} + v_{kl}, \quad (2.2)$$

where the estimated channel \hat{h}_{kl} is written as $\hat{h}_{kl} \triangleq |\hat{h}_{kl}|e^{j\hat{\theta}_{kl}}$, $\tilde{\theta}_{kl} \triangleq \theta_{kl} - \hat{\theta}_{kl}$ is the phase estimation error², and $v_{kl} \triangleq \text{Re}\{w_{kl}e^{-j\hat{\theta}_{kl}}\} \sim \mathcal{N}(0, \sigma_w^2/2)$ is the AWGN at the receiver. The samples $\{r_{kl}\}$, $k = 1, 2, \dots, N, k \neq l$ are used to detect and update the majority bit at node s_l .³ Since the sum of votes, $\Delta_l \triangleq \sum_{k=1, k \neq l}^N x_k$ is indicative of the majority bit at node s_l , where $x_k \in \{-1, +1\}$ is the BPSK symbol corresponding to $b_k(t-1)$, we use the majority bit decision rule:

$$g(\hat{\Delta}_l) \triangleq \begin{cases} 1 & \hat{\Delta}_l \geq 0 \\ 0 & \text{otherwise,} \end{cases} \quad (2.3)$$

where $\hat{\Delta}_l$ is an estimate of sum of votes, computed at node s_l . In this work, two schemes are considered for obtaining $\hat{\Delta}_l$: 1) an LMMSE-based scheme and 2) a co-phased combining scheme.

LMMSE-based scheme [63]

Here, a weighted linear combination of the processed samples $\{r_{kl}\}$ is considered as an estimate of Δ_l , i.e., $\hat{\Delta}_l^{(wc)} = \boldsymbol{\alpha}_l^T \mathbf{r}_l$, where $\boldsymbol{\alpha}_l \triangleq [\alpha_{1l} \ \alpha_{2l} \ \dots \ \alpha_{kl} \ \dots \ \alpha_{Nl}]_{k \neq l}^T$ and $\mathbf{r}_l \triangleq [r_{1l} \ r_{2l} \ \dots \ r_{kl} \ \dots \ r_{Nl}]_{k \neq l}^T$. Here, the superscript *wc* stands for weighted combining. The optimal weight vector $\boldsymbol{\alpha}_l^*$ is evaluated by solving the MMSE estimation problem

$$\boldsymbol{\alpha}_l^* = \arg \min_{\boldsymbol{\alpha}_l} \mathbb{E}[(\hat{\Delta}_l^{(wc)} - \Delta_l)^2]. \quad (2.4)$$

²The distribution of the channel phase error $|\tilde{\theta}_{kl}|$ is derived in [67] and is given by

$$F_{|\tilde{\theta}_{kl}|}(x) = 1 - \int_0^{\pi-x} \mathcal{L}_{kl} \left(\frac{\gamma_p \sin^2 x}{\sin^2 \beta} \right) \frac{d\beta}{\pi}, \quad 0 \leq x < \pi, \quad \text{where } \mathcal{L}_{kl}(s) = 1/(1 + s\mathbb{E}[|h_{kl}|^2]).$$

³For simplicity, we ignore the l^{th} sensor's own data bit, x_l . This is fine when the bit distribution across the nodes is such that any one node's data bit does not alter the majority vote. In Sec. 2.4, we will show through simulations that ignoring the self-bit only marginally affects the consensus performance.

On substituting the MMSE solution $\alpha_{kl}^* = \frac{|\hat{h}_{kl}|}{|\hat{h}_{kl}|^2 + \sigma_w^2/2}$, the sum of votes estimate can be expressed as

$$\hat{\Delta}_l^{(wc)} = \sum_{k=1, k \neq l}^N \left[\alpha_{kl}^* |h_{kl}| \cos \tilde{\theta}_{kl} x_k \sqrt{E_d} + \alpha_{kl}^* v_{kl} \right]. \quad (2.5)$$

We note that the above LMMSE-based scheme uses the estimated channels \hat{h}_{kl} to compute the combining weights, in contrast to the scheme in [63], which assumed the availability of perfect channel state information h_{kl} at the nodes.

Co-phased combining scheme

In this scheme, the sum of co-phased samples r_{kl} is used as an estimate of Δ_l , i.e.,

$$\hat{\Delta}_l^{(cc)} = \sum_{k=1, k \neq l}^N \left[|h_{kl}| \cos \tilde{\theta}_{kl} x_k \sqrt{E_d} + v_{kl} \right]. \quad (2.6)$$

The sum of votes estimate in (2.6) only requires the channel phase, while (2.5) depends on both the gain and the phase. Due to this, the consensus behavior of the two schemes in the face of fading and the imperfect CSI at the nodes can be different. It is of interest to study their relative performance.

Note that, $\hat{\Delta}_l^{(wc)}$ and $\hat{\Delta}_l^{(cc)}$ can be compactly expressed as

$$\hat{\Delta}_l = h \sqrt{E_d} + v, \quad (2.7)$$

where we term $h \triangleq \sum_{k=1, k \neq l}^N \beta_{kl} |h_{kl}| \cos \tilde{\theta}_{kl} x_k$ as the *effective channel-symbol*, and the noise $v \sim \mathcal{N}(0, \sigma_v^2)$ with $\sigma_v^2 = \sum_{k=1, k \neq l}^N (\beta_{kl})^2 \sigma_w^2/2$. The parameter $\beta_{kl} = \alpha_{kl}^*$ for the LMMSE-based scheme, and $\beta_{kl} = 1$ for the co-phased combining scheme.

2.3 Performance Analysis

We define the *state* of the network at time t as an ordered collection of decision bits (majority bit estimates), $[b_1(t) \ b_2(t) \ \dots \ b_N(t)]$. After each bit-update, the network can attain any one of the $M = 2^N$ possible states with a probability that depends solely on the previous state and the current received pilot and data samples at the nodes. That is, the network state evolves as a first order discrete-time Markov chain (MC). The accurate consensus state of the MC is either the all-ones state or the all-zeros state, depending on whether the initial majority bit is one or zero. This MC is time inhomogeneous, as the channels are time-varying across cycles. For time inhomogeneous MCs with independent random transition probability matrices across the time steps, the marginal state distribution of the MC, i.e., the state distribution averaged over the randomness of the transition probability matrices, is precisely that of a *time homogeneous MC* with the *average TPM* [68]. Therefore, the average of the TPM over the distribution of the channel states is used to analyze the consensus behavior of the network.⁴ The average state distribution vector at time t , denoted by $\bar{\pi}(t) \in [0, 1]^N$, is thus given by $\bar{\pi}(t) = (\bar{\mathbf{P}})^t \pi(0)$. Here, $\bar{\mathbf{P}} \triangleq [\bar{P}_{ij}]$ is the average TPM, $\pi(0)$ is the initial state distribution vector, and \bar{P}_{ij} is the average probability of transition (averaging over the channel state distribution) from state $\phi^{(j)}$ to state $\phi^{(i)}$ in one cycle, where $\{\phi^{(i)}, i \in \{1, 2, \dots, M\}\}$ represents the different possible states of the MC.

For example, when three sensor nodes are involved in the consensus procedure, the

⁴An alternative model, under slowly varying channels, is to assume that the channel stays fixed for the duration of the consensus cycles. In this case, we would work with the TPM conditioned on the joint channel states between the nodes. The resulting MC is time homogeneous, making the analysis easier than the case considered in this chapter.

states of the Markov chain are '000', '001', ..., '111'. Let, p_0, p_1 and p_2 denote the probability of detecting bit '1' at a sensor when two other sensors transmit bits '(0, 0)', '(0, 1)', and '(1, 1)', respectively. Then, by combining equivalent states (for e.g., state '001' is equivalent to '100' and '010'), a concise form of the average TPM is given by

$$\begin{bmatrix} p_2^3 & 3p_0p_2^2 & 3p_0^2p_2 & p_0^3 \\ p_1^2p_2 & p_1^2p_0 + 2p_1^2p_2 & p_1^2p_2 + 2p_1^2p_0 & p_1^2p_0 \\ p_1^2p_0 & p_1^2p_2 + 2p_1^2p_0 & p_1^2p_0 + 2p_1^2p_2 & p_1^2p_2 \\ p_0^3 & 3p_0^2p_2 & 3p_0p_2^2 & p_2^3 \end{bmatrix}. \quad (2.8)$$

Due to the additive noise term in (2.1), $0 < \bar{P}_{ij} < 1 \forall i, j \in \{1, 2, \dots, M\}$ (see Appendix A.6 for proof), and hence, the MC is irreducible and aperiodic. Thus, the stationary state distribution $\bar{\pi}_\infty \triangleq \lim_{t \rightarrow \infty} \bar{\pi}(t)$ is independent of the initial state [69], as $\bar{\pi}_\infty = \bar{\mathbf{P}}\bar{\pi}_\infty$ and $\mathbf{1}^T \bar{\pi}_\infty = 1$. However, the network can still achieve accurate consensus with high probability in the transient period of the MC.

From Perron's and Gershgorin's theorems [70], it is known that, for the positive stochastic matrix $\bar{\mathbf{P}}$, the largest eigenvalue λ_1 is 1 and is of multiplicity one, and the absolute value of all the other eigenvalues is strictly less than 1. The second largest eigenvalue λ_2 of $\bar{\mathbf{P}}$ characterizes the transient duration of the MC [71]. The closer λ_2 is to unity, the longer the transient period, and the higher the probability that the network attains and stays in consensus for a long duration. Thus, λ_2 , along with the probability of attaining accurate consensus starting from an arbitrary state, are important performance metrics for understanding the consensus behavior of the network.

In this work, two more quantities, the average hitting time and the average consensus duration, are analyzed. There are no absorbing states due to the noisy channels, and hence the average hitting time and average consensus duration are important metrics

to study the consensus behavior. The average hitting time is the average number of cycles required to attain the consensus for the first time starting from an initial state $\phi^{(j)}$. The average consensus duration is the average number of cycles for which the network will stay in consensus once it is attained. These metrics are used to compare the performance of the two bit-update procedures and quantify the effect of channel estimation errors on the consensus performance. Finally, the tradeoff between the power allowed for pilot and data symbols on the consensus behavior is studied.

As discussed above, the consensus behavior of the network is determined by the average TPM of the MC. However, in the presence of channel estimation errors, the average TPM is analytically intractable for the LMMSE-based scheme because of its dependence on the channel gain estimates. The analysis for the co-phased combining scheme is presented below.

2.3.1 Probability of Detecting the Majority Bit

The probability of correctly detecting the majority bit from the received data symbols is necessary to determine the TPM of the MC, and is critical to the consensus behavior of the network. Since the noise is Gaussian distributed, conditioned on K , the number of sensors transmitting a +1, the average probability \bar{p}_l of detecting the majority bit as '1' at node s_l is given by

$$\bar{p}_l = \mathbb{E} \left[\Pr\{\hat{\Delta}_l \geq 0 | H = h\} \right] = \int_{-\infty}^{\infty} \mathcal{Q} \left(\frac{-h\sqrt{E_d}}{\sigma_v} \right) f_H(h) dh, \quad (2.9)$$

where $f_H(h)$ is the pdf of the effective channel-symbol H and $\mathcal{Q}(\cdot)$ is the Gaussian Q -function.

Suppose a subset of the nodes, $\mathcal{K} \subseteq \mathcal{S} \setminus \{s_l\}$, $|\mathcal{K}| = K$, transmit $+1$, and the remaining $N - K - 1$ nodes in $\mathcal{K}^c \triangleq \mathcal{S} \setminus \{\mathcal{K}, s_l\}$ transmit -1 . Then, the effective channel-symbol h in (2.7) can be expressed as $h = h_p - h_n$, where $h_p \triangleq \sum_{s_k \in \mathcal{K}} |h_{kl}| \cos \tilde{\theta}_{kl}$ and $h_n \triangleq \sum_{s_k \in \mathcal{K}^c} |h_{kl}| \cos \tilde{\theta}_{kl}$. Let H_p and H_n be random variables corresponding to the realizations h_p and h_n , respectively. The pdf of the sum of K weighted i.i.d. Rayleigh r.v.s, H_p , is unfortunately not available in closed-form. However, it is well approximated by the pdf of a Nakagami r.v. with shape parameter, $m_1 = (\mathbb{E}[H_p^2])^2 / \text{Var}[H_p^2]$, and spread parameter, $\Omega_1 = \mathbb{E}[H_p^2]$. Similarly, h_n can be approximated as a Nakagami r.v. with shape and spread parameters m_2 and Ω_2 , respectively. At high pilot SNRs, the weights are of nearly unit magnitude and approximation error turns out to be particularly small. Also, as found through simulations, the approximation error reduces with increasing K . The derivation of $\mathbb{E}[H_p^2]$ and $\text{Var}[H_p^2]$, required for evaluating the parameters m_1, m_2, Ω_1 and Ω_2 , is presented in Lemma 1. The resulting analytical expression of the approximated pdf $f_H(h)$ is presented in Lemma 2.

Lemma 1. *For a given pilot SNR, $\text{SNR}_p \triangleq \sigma^2 E_p / \sigma_w^2$, and with the second moment of i.i.d. Rayleigh r.v.s H_{kl} , $\mathbb{E}[H_{kl}^2] = \sigma^2$, the mean and variance of the r.v. H_p^2 defined above are given by*

$$\mathbb{E}[H_p^2] = \frac{K\sigma^2(2 + (4 + (K-1)\pi)\gamma_p\sigma^2)}{1 + \gamma_p\sigma^2} \quad (2.10)$$

$$\begin{aligned} \text{Var}[H_p^2] &= K\mathbb{E}[G_{kl}^4] + 3K(K-1)(\mathbb{E}[G_{kl}^2])^2 \\ &\quad + K(K-1)(K-2)(K-3)(\mathbb{E}[G_{kl}])^4 \\ &\quad + 6K(K-1)(K-2)(\mathbb{E}[G_{kl}]^2\mathbb{E}[G_{kl}^2]) \\ &\quad + 4K(K-1)\mathbb{E}[G_{kl}^3]\mathbb{E}[G_{kl}] - (\mathbb{E}[H_p^2])^2, \end{aligned} \quad (2.11)$$

where $\gamma_p \triangleq E_p/\sigma_w^2$ and $G_{kl} \triangleq |H_{kl}| \cos \tilde{\theta}_{kl}$; and closed form expressions for $\mathbb{E}[G_{kl}]$, $\mathbb{E}[G_{kl}^2]$, $\mathbb{E}[G_{kl}^3]$ and $\mathbb{E}[G_{kl}^4]$ are provided in the proof.

Proof. See Appendix A.1. □

Lemma 2. *The pdf of the effective channel-symbol is given by*

$$f_H(h) = \frac{2 \left(\frac{m_1}{\Omega_1}\right)^{m_1} \left(\frac{m_2}{\Omega_2}\right)^{m_2} e^{-\frac{h^2 m_1 m_2}{m}}}{\Gamma(m_1)\Gamma(m_2) \left(\frac{m}{\Omega}\right)^{m_1+m_2-\frac{1}{2}}} \sum_{i=0}^{2m_1-1} \sum_{j=0}^{2m_2-1} \binom{2m_1-1}{i} \binom{2m_2-1}{j} \left(\frac{m_2 \Omega_1 h}{\sqrt{m \Omega}}\right)^{2m_1-1-i} \left(\frac{-m_1 \Omega_2 h}{\sqrt{m \Omega}}\right)^{2m_2-1-j} \Gamma\left(\frac{i+j+1}{2}, \frac{(m_1 \Omega_2 h)^2}{m \Omega}\right), \quad (2.12)$$

for $h \geq 0$, where $m \triangleq m_1 \Omega_2 + m_2 \Omega_1$, $\Omega \triangleq \Omega_1 \Omega_2$ and $\Gamma(\cdot, \cdot)$ is the upper incomplete Gamma function. For $h < 0$, $f_H(h)$ can be evaluated by swapping the parameters m_1, Ω_1 with m_2, Ω_2 , respectively.

Proof. See Appendix A.2. □

To obtain the result in Lemma 2, the parameters $2m_1$ and $2m_2$ are rounded-off to the nearest integers. The $f_H(h)$ given by Lemma 2 can now be substituted into (2.9) to evaluate \bar{p}_l as a single integral, this is discussed in Appendix A.3. Note that, the average probability \bar{p}_l is conditioned on K , the number of sensors transmitting +1, but this dependence is not explicitly indicated to keep the notation light.

2.3.2 Average Transition Probability Matrix

Suppose the network is in a state $\phi^{(j)}$ at time $t-1$ and $\phi^{(i)} \triangleq [b_1^{(i)} b_2^{(i)} \dots b_N^{(i)}]$ at time t . Let us denote the average probability of node s_l detecting bit '1' at time t , conditioned on $\phi^{(j)}$, by $\bar{p}_l^{(j)}$. At node s_l , the average probability of the bit being updated to $b_l^{(i)}$ is given by $b_l^{(i)} \bar{p}_l^{(j)} + (1-b_l^{(i)})(1-\bar{p}_l^{(j)})$. The update decisions $b_l^{(i)}$ at each of the nodes s_l , $l = 1, 2, \dots, N$,

are independent, as the receiver thermal noise and the wireless channels between the nodes are independent. Thus, the average probability of going from $\phi^{(j)}$ to $\phi^{(i)}$ in one cycle is given by

$$\bar{P}_{ij} = \prod_{l=1}^N \left[b_l^{(i)} \bar{p}_l^{(j)} + (1 - b_l^{(i)}) (1 - \bar{p}_l^{(j)}) \right], \quad (2.13)$$

for $i, j \in \{1, 2, \dots, M\}$. The average probability of going from $\phi^{(j)}$ to an all-one state $\phi^{(M)}$ or to an all-zero state $\phi^{(1)}$ is given by

$$\bar{P}_{Mj} = \prod_{l=1}^N \bar{p}_l^{(j)} \quad (2.14)$$

$$\bar{P}_{1j} = \prod_{l=1}^N (1 - \bar{p}_l^{(j)}). \quad (2.15)$$

We have thus determined the average TPM $\bar{\mathbf{P}}$ of the MC. Note that, the average probability of detecting bit ‘1’ conditioned on the all-zero state, $\bar{p}_l^{(1)}$, is the same for all the nodes. Thus, hereafter, $\bar{p}_l^{(1)}$ is denoted as $\bar{p}^{(1)}$, and similarly, $\bar{p}_l^{(M)}$ is denoted as $\bar{p}^{(M)}$. In [63], a simple approximation to the second largest eigenvalue λ_2 of the average TPM $\bar{\mathbf{P}}$ is shown to be $1 - 2\bar{p}^{(1)}$. This approximation is derived for the Rayleigh fading channel by linearizing the Q-function. Moreover, when $N = 2$ or 3 sensors, it can be shown that λ_2 is exactly $1 - 2\bar{p}^{(1)}$. The derivation of the second largest eigenvalue for $N = 3$ sensors is discussed in Appendix A.4. With larger N , the second eigen value would be much closer to 1. This is because, the probability of detecting bit 1 when all the nodes have bit 0, $\bar{p}^{(1)}$, tends to zero roughly exponentially with increasing N , and consequently, the second largest eigen value tends to 1. As mentioned earlier, the closer the second largest eigenvalue to unity, the better the consensus behavior of the network.

2.3.3 Average Hitting Time

Starting from a state $\phi^{(j)}$, the average number of cycles taken to reach a consensus state for the first time is termed as the average hitting time. The probability of reaching state $\phi^{(i)}$ for the first time starting from state $\phi^{(j)}$ after exactly n cycles, denoted by $f_{ij}^{(n)}$, can be recursively expressed as

$$f_{ij}^{(n)} = \sum_{\substack{k=1 \\ k \neq i}}^M \bar{P}_{kj} f_{ik}^{(n-1)}. \quad (2.16)$$

In other words, the R.H.S. of (2.16) represents probability of the network reaching any state $\phi^{(k)}$, $k = 1, 2, \dots, M, k \neq i$, in the first cycle, and reaching the state $\phi^{(i)}$ exactly after next $n - 1$ cycles. The vector of probabilities $\mathbf{f}_i^{(n)} \triangleq [f_{i1}^{(n)} \ f_{i2}^{(n)} \ \dots \ f_{ij}^{(n)} \ \dots \ f_{iM}^{(n)}]^T$, $j \neq i$ can be expressed as

$$\mathbf{f}_i^{(n)} = \mathbf{Q}^T \mathbf{f}_i^{(n-1)}, \quad (2.17)$$

where \mathbf{Q} is the TPM obtained by removing the i^{th} row and i^{th} column of average TPM $\bar{\mathbf{P}}$. Simplification of (2.17) leads to

$$\mathbf{f}_i^{(n)} = (\mathbf{Q}^T)^{n-1} \mathbf{f}_i^{(1)} = (\mathbf{Q}^T)^{n-1} \mathbf{p}_i^T, \quad (2.18)$$

where \mathbf{p}_i is i^{th} row of the average TPM $\bar{\mathbf{P}}$ with the $(i, i)^{th}$ entry removed. Then, the average hitting time is given by

$$\tau_h = \sum_{n=1}^{\infty} n f_{ij}^{(n)}. \quad (2.19)$$

Setting $\phi^{(i)}$ to be the appropriate consensus state, i.e., either the all zeros state or the all ones state depending on the initial distribution of the data bits, we can compute the average hitting time using the above equation.

2.3.4 Average Consensus Duration

The average consensus duration, τ_c , is the average number of cycles for which the network stays in the same consensus state once it has reached consensus. Suppose the network is in consensus at the end of t_0^{th} cycle. Let the random variable T_c represent the number of consecutive cycles for which the network stays in consensus. Assuming channel independence between any two cycles, the average probability (here, the averaging is over the channel states) that the network is in consensus for n consecutive cycles is simply given by

$$Pr\{T_c = n\} = (\bar{P}_c)^n(1 - \bar{P}_c), \quad (2.20)$$

where \bar{P}_c is the average probability of being in consensus after the next cycle once the network is already in consensus. The expected number of cycles for which the network stays in consensus is thus

$$\tau_c = \sum_{n=1}^{\infty} n(\bar{P}_c)^n(1 - \bar{P}_c) = \frac{\bar{P}_c}{1 - \bar{P}_c}. \quad (2.21)$$

The average probability \bar{P}_c for an all-one consensus state is given by $\bar{P}_{MM} = (\bar{p}^{(M)})^N$ (see (2.14)). Similarly, for the all-zero consensus state, $\bar{P}_c = \bar{P}_{11} = (1 - \bar{p}^{(1)})^N$. The average probabilities $\bar{p}^{(1)}$ and $\bar{p}^{(M)}$ are derived in Appendix A.5. Thus, we can use the above equation to obtain the average consensus duration of the network. Note that, the average hitting time decreases and average consensus duration increases with increase in data SNR, $\text{SNR}_d \triangleq \frac{E_d \sigma^2}{\sigma_w^2 / 2}$, and pilot SNR, $\text{SNR}_p \triangleq \frac{E_p \sigma^2}{\sigma_w^2}$. The SNR values determine the entries of the TPM via the Q-function, which determines the average probabilities of the different states. The average probabilities, in turn, determine the

average hitting time and the average consensus duration via the analysis presented in the chapter. Due to the intricate nature of the analysis, it is unfortunately difficult to directly relate the performance of the protocol to the data and pilot SNRs. Hence, we study the performance via simulations.

2.3.5 Data Power and Pilot Power Allocation

In a given consensus cycle, under a total power constraint, the optimization of the power allotted to the data and pilot transmission can be carried out, for example, by maximizing the average consensus duration, or, by minimizing the average hitting time. To do this, the average probability for the all-ones consensus state, \bar{P}_{MM} , equivalently, $\bar{p}^{(M)}$, can be used as the cost function. Therefore, the optimal data and pilot powers are obtained by solving

$$E_d^*, E_p^* = \arg \max_{E_d, E_p} \bar{p}^{(M)} \quad \text{subject to} \quad E_d + E_p = E. \quad (2.22)$$

As shown in Appendix A.5, the average probability $\bar{p}^{(M)}$ can be obtained in closed form as

$$\bar{p}^{(M)} = 0.5 + \sqrt{\frac{\gamma_d}{2\pi}} \frac{\Gamma(m_1 + 0.5)}{\Gamma(m_1) \sqrt{m_1/\Omega_1}} {}_2F_1 \left(0.5, m_1 + 0.5; 1.5; -\frac{\gamma_d}{2m_1/\Omega_1} \right), \quad (2.23)$$

where $\gamma_d = E_d/\sigma_v^2$, $\sigma_v^2 = \sigma_w^2(N-1)/2$ and ${}_2F_1$ is the Gaussian hypergeometric function. Note that the parameters of the Nakagami r.v. H_p , namely, $m_1 = (\mathbb{E}[H_p^2])^2/\text{Var}[H_p^2]$ and $\Omega_1 = \mathbb{E}[H_p^2]$, are functions of the pilot power E_p . Substituting (2.23) in (2.22) leads to a one dimensional optimization problem, which can be solved numerically to obtain the optimal values of E_d and E_p . The importance of optimizing the power allocation to

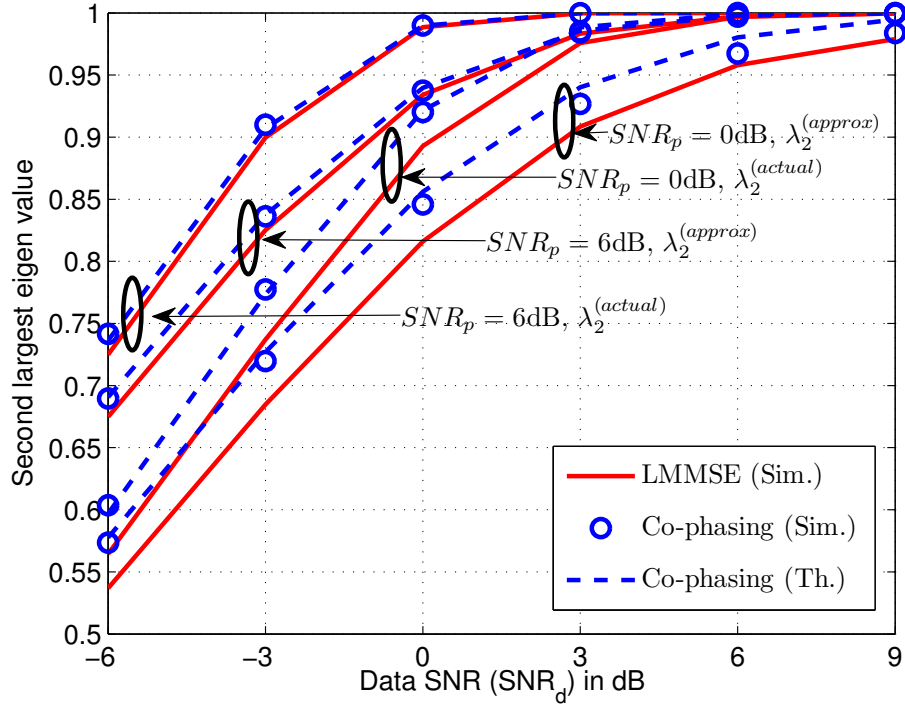


Figure 2.2: Second largest eigenvalue vs. Data SNR (denoted by SNR_d) for different pilot SNRs (denoted by SNR_p), with $N = 8$ nodes.

training and data symbols is illustrated in the next section.

2.4 Simulation Results

The simulation set-up consists of $N = 8$ sensor nodes. The receiver noise and the channels between the sensors are drawn i.i.d. from $\mathcal{CN}(0, 1)$. The average TPM is evaluated by averaging over 20,000 channel instantiations.

We start with presenting results on the second largest eigenvalue, λ_2 , of the average TPM of the state space of the Markov chain. In Fig. 2.2, the value of λ_2 obtained by the two schemes is compared, along with their approximation, $1 - 2\bar{p}^{(1)}$, presented in Sec. 2.3.2. It can be seen that λ_2 gets closer to 1 with increasing data and pilot SNRs. At lower pilot SNRs, the co-phased combining scheme outperforms the LMMSE-based

scheme from [63], i.e., λ_2 of the former is closer to 1 than the latter. This is because, the co-phased combining depends only on the channel phase estimates, whereas the LMMSE-based scheme depends on both magnitude and phase estimates of the channel. This leads to larger errors in the sum of votes estimate for the LMMSE-based scheme. However, with increasing pilot power, the two schemes result in nearly the same value of λ_2 . Also, we see that the approximate expression for λ_2 is a lower bound on the actual eigenvalue when $N = 8$, although it is accurate for the $N = 2$ and the $N = 3$ case. The approximation captures the relative behavior of the LMMSE and co-phasing schemes well. Finally, the excellent agreement between the theoretical and experimental values of λ_2 for the co-phased combining scheme is clear from the plot.

Next, we evaluate the average consensus duration performance of the two schemes, in Fig. 2.3. At low SNRs, the average consensus duration increases linearly, whereas at high SNRs, the increase in average consensus duration is roughly quadratic. At low to intermediate pilot SNRs, the co-phased combining scheme stays longer in consensus state than the LMMSE-based scheme, as expected. The overall consensus performance depends both on the pilot SNR and data SNR, and therefore, even with accurate channel estimates (high pilot SNRs), the co-phased combining scheme outperforms the LMMSE scheme at low to moderate data SNRs. The LMMSE-based scheme starts outperforming the co-phased combining scheme only at high pilot SNR and high data SNR. Also, for the co-phased combining scheme, the average consensus duration obtained through simulations matches the theoretical results obtained through (2.21).

The average hitting time and the average probability of accurate consensus performance of the two schemes is plotted in Figs. 2.4 and 2.5, respectively. In Fig. 2.4, the

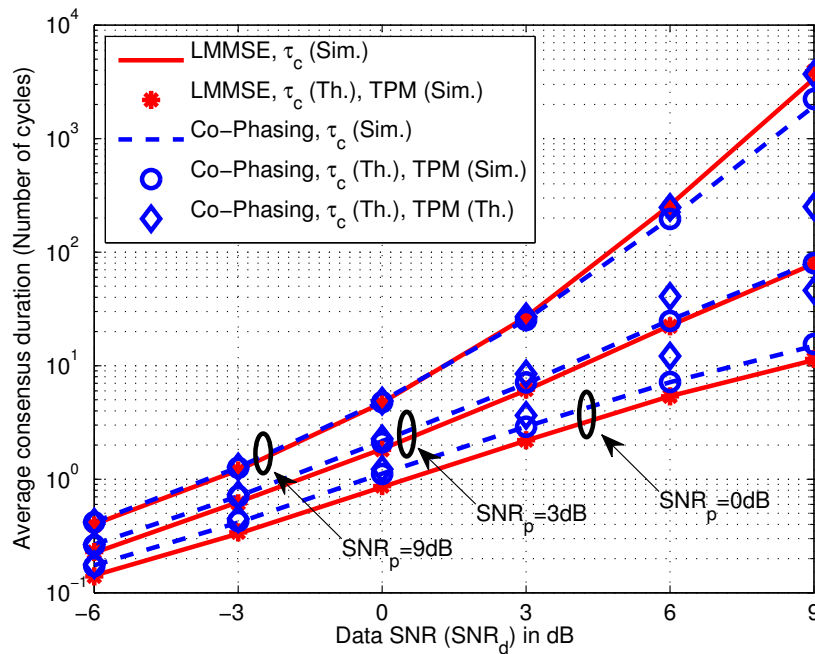


Figure 2.3: Average consensus duration vs. Data SNR, with $N = 8$, and for different pilot SNRs. The curves labeled τ_c (Th.), TPM (Sim.) correspond to the theoretical value of the average consensus duration computed using the TPM obtained from the Monte Carlo averaging, while the curves labeled τ_c (Th.), TPM (Th.) correspond to the theoretical value of the average consensus duration computed using the theoretical TPM.

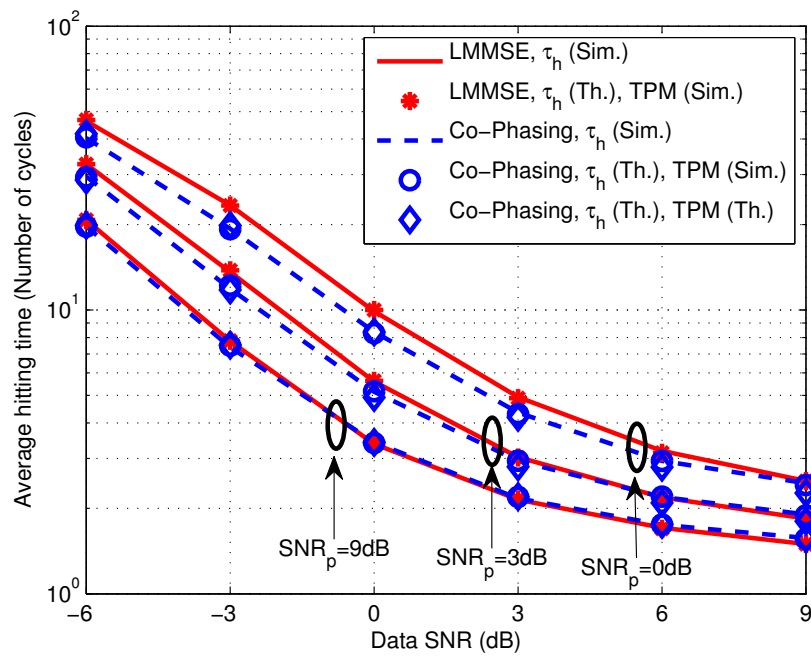


Figure 2.4: Average hitting time Vs. Data SNR, with $N = 8$, and for different pilot SNRs.

average hitting time is evaluated by averaging the time to hit the all-ones consensus state over the initial states '11111110', '11111100', and '11111000'. In Fig. 2.5, the average probability of accurate consensus is plotted as a function of the number of cycles of the update procedure, when the initial state across the nodes is '00011111'. The conclusions from the figure are similar to that of the average consensus duration: the performance improves with increasing data and pilot SNRs; at low to intermediate pilot SNRs, the co-phased combining outperforms the LMMSE-based scheme; and, for the co-phased combining scheme, the theoretical expressions in (2.19) match the simulation results. Also, the importance of accounting for the channel estimation errors in evaluating the relative performance of different consensus protocols is clear from the plot. At high pilot SNRs, the channel estimates are accurate, the two schemes offer similar performance, while at intermediate or lower pilot SNRs, the co-phasing scheme outperforms the LMMSE-based scheme.

Figure 2.6 shows the average probability of accurate consensus for various numbers of nodes, as a function of the number of consensus cycles. The probability of accurate consensus is much higher for $N = 22$ sensors with $\text{SNR}_p = 0$ dB and $\text{SNR}_d = 3$ dB compared to $N = 4$ sensors and a higher receive SNR, $\text{SNR}_p = 3$ dB and $\text{SNR}_d = 6$ dB. This is because of the linear scaling of the average effective SNR with the number of sensors. Also, for the co-phased combining scheme, with increase in the number of nodes, the theoretical curves matches well with simulations.

In developing the consensus protocol, the self-bit was ignored for simplicity of presentation. Figure 2.7 shows the second largest eigenvalue for the co-phased combining scheme when the sensors' own data bit is considered. The sum of votes estimate is

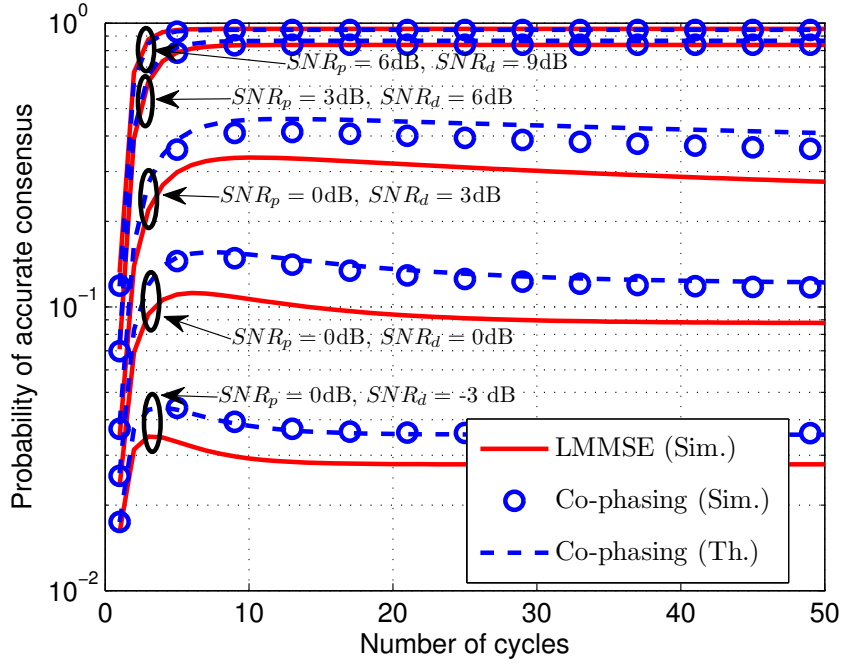


Figure 2.5: Probability of accurate consensus vs. number of consensus cycles, starting from an initial state of '00011111'.

computed by adding the self-bit with a scaling of $\sqrt{E_d}$ to (2.6). Accounting for the self-bit clearly improves the performance, but the loss due to the approximation gets smaller as the number of sensors is increased. Also, as data SNR increases, the sum of votes estimate improves. This leads to the second largest eigenvalue without the self-bit to be close to that with self-bit. Hence, when the SNR and the number of nodes are moderately large, it is reasonable to ignore the self-bit in evaluating the consensus performance.

Next, we consider the allocation of the pilot and data power to optimize the consensus performance. In Figs. 2.8 and 2.9, the average consensus duration and average hitting time of the co-phased combining scheme are plotted as a function of the ratio of data power to pilot power, under a total power constraint. The average consensus duration is maximum and the average hitting time is minimum for $\frac{E_d}{E_p} = 1.3$ and $\frac{E_d}{E_p} = 1.45$, when

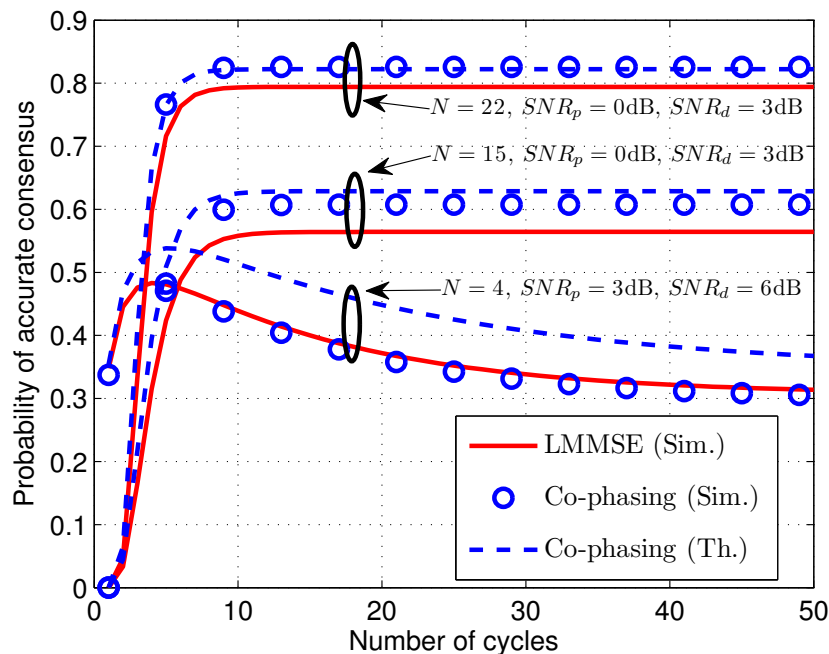


Figure 2.6: Probability of accurate consensus vs. number of consensus cycles, for number of nodes, $N = 4, 15,$ and 22 . The initial state of the network is the simple majority state, for example, the initial state of the 4 nodes network is '0111'.

the total power available is 6 dB and 9 dB, respectively. This indicates that, at higher total powers, the data symbol has to be given a larger share of the total power compared to the pilot symbol. At lower total powers, the best average consensus performance is obtained for nearly equal sharing of the available power. Similar conclusions are obtained from optimizing the other metrics such as the second largest eigenvalue or probability of accurate consensus; they are not presented here to avoid repetition.

Next, Fig. 2.10 shows the average probability of accurate consensus for the co-phased combining scheme when the path-loss (with path-loss exponent of 2) is also considered, along with the Rayleigh fading. A linear arrangement of 8 sensors that are uniformly spaced on a stretch of 10 m and a reference distance of 1 m is considered for the simulations. At higher transmit powers for pilot and data symbol, $E_p = 15$ dB and $E_d = 15$ dB,

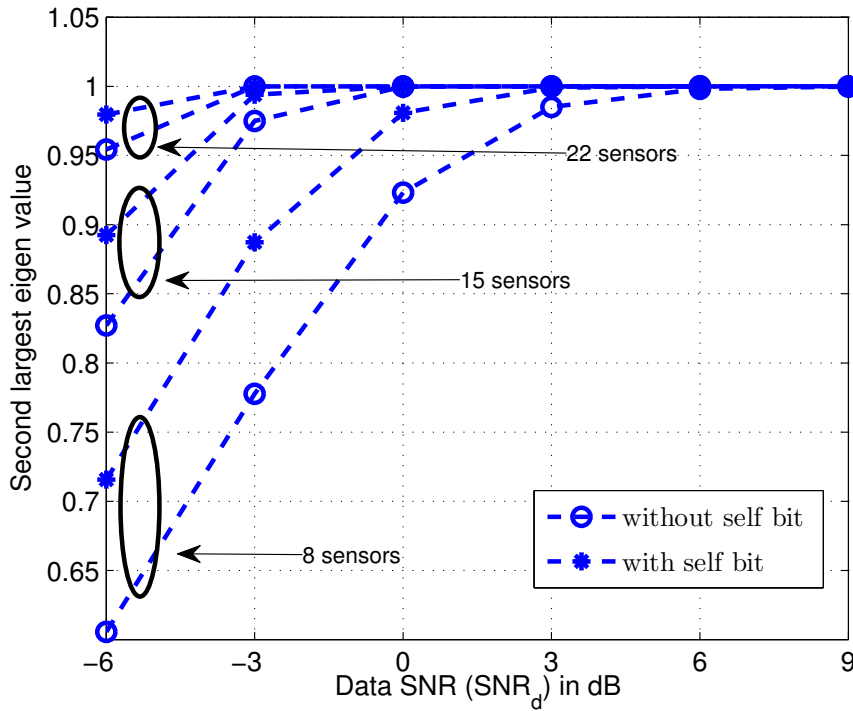


Figure 2.7: Second largest eigenvalue vs. Data SNR for the co-phased combining scheme at a pilot SNR of 0 dB, when the sensors' self-bit is taken into account.

the probability of accurate consensus is close to 1. Also, the network attains its consensus state within about 5 cycles.

Finally, in Fig. 2.11, we show the probability of accurate consensus performance of the co-phased combining scheme when the network is not fully connected. While estimating the sum of votes in (2.7), the weights β_{kl} are set to 0 for all those links which have a link gain less than a threshold η , where η is determined for a given link failure probability, $\Pr\{|h_{kl}| \leq \eta\} = q$. At high data and pilot SNRs, the performance deteriorates as the link failure probability increases, as expected. At lower SNRs, as the channels are more noisy, the performance is relatively robust to link failures.

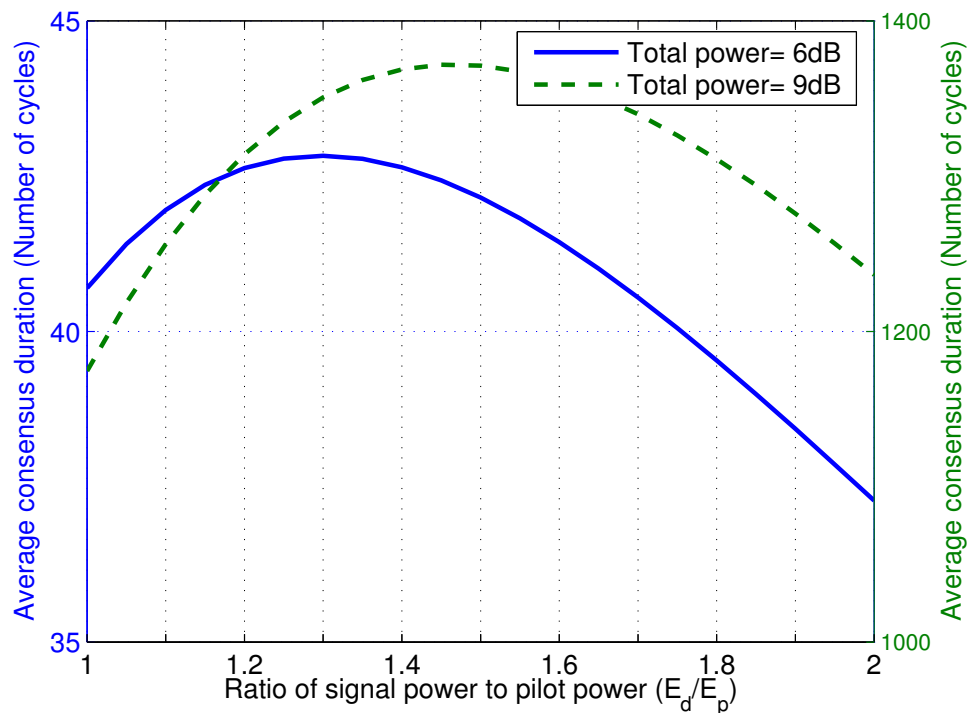


Figure 2.8: Average consensus duration vs. ratio of data power to pilot power under a total power constraint.

2.5 Conclusions

In this chapter, we considered a physical layer protocol for achieving majority-bit consensus, where a set of nodes exchange their current majority-bit estimates over multiple cycles. We contrasted two bit-update schemes: 1) LMMSE-based scheme and 2) Co-phased combining scheme, when the available CSI is estimated using pilot symbols sent from the nodes. We analytically evaluated several metrics that determine the average consensus performance, such as the average probability of detecting the correct majority bit, the average hitting time, and the average consensus duration, by employing a difference-of-Nakagami approximation for a combined effective channel. The results highlighted the importance of accounting for the effect of channel estimation

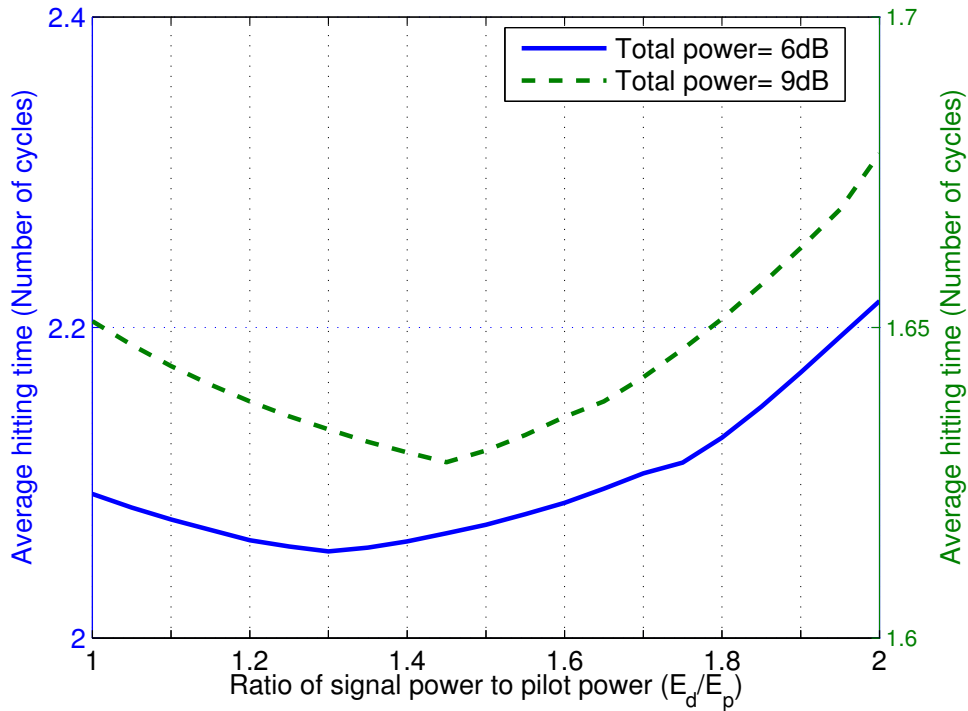


Figure 2.9: Average hitting time vs. ratio of data power to pilot power under a total power constraint.

errors on the performance. For example, at low to intermediate SNRs, the co-phased combining scheme outperforms the LMMSE-based scheme, although they offer very comparable performance under perfect channel state information. This is because of the lesser dependence of the co-phased combining scheme on channel estimates. We showed that optimizing the power allocation between the pilot and data symbols can result in a significant improvement in the consensus performance. We also presented extensive simulation results to validate the theoretical expressions and illustrate the various tradeoffs involved. Future work could consider extension of this study to non-binary (e.g., average) consensus problems.

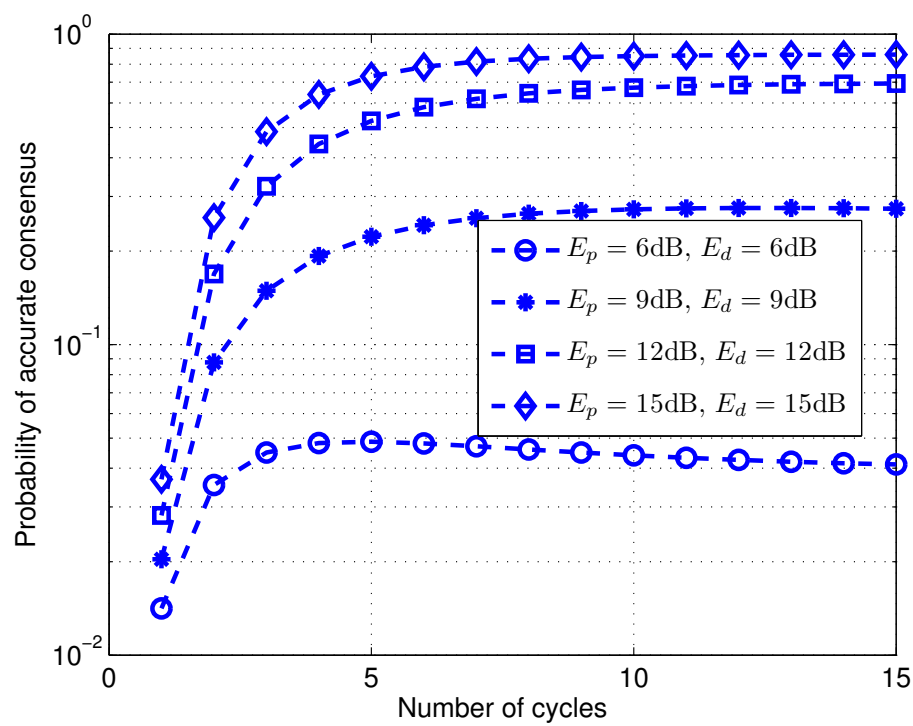


Figure 2.10: Probability of accurate consensus vs. number of consensus cycles for the co-phased combining scheme when the path-loss between sensors is taken into account. The probability of accurate consensus is averaged over all the initial states corresponding to 5 sensors with bit '1' and 3 sensors with bit '0'.

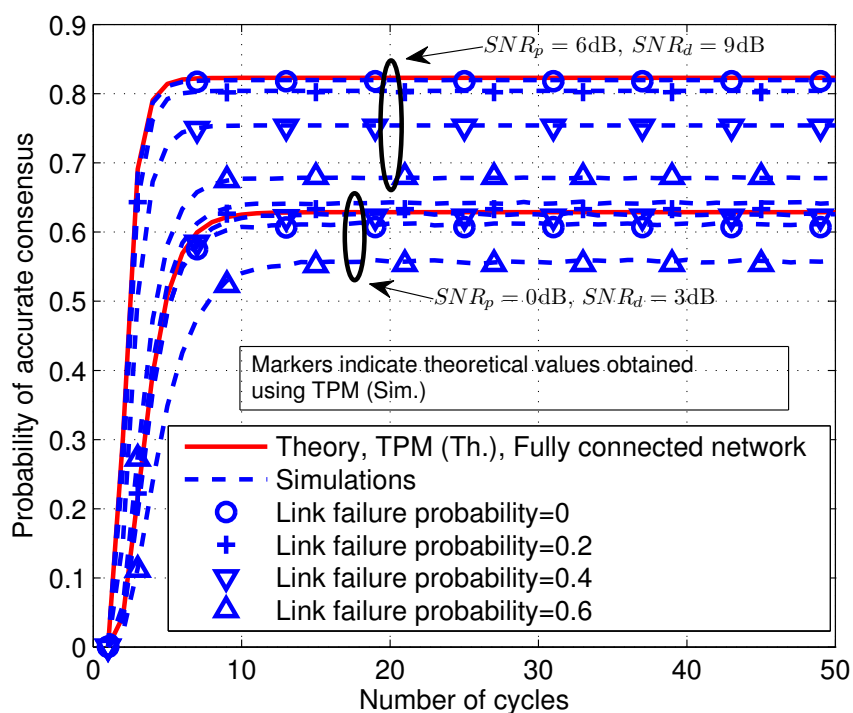


Figure 2.11: Probability of accurate consensus vs. number of consensus cycles for the co-phased combining scheme for an $N = 15$ sensor network which is not fully connected.

Chapter 3

Multiple Transmitter Localization and Communication Footprint Identification using Energy Measurements

Spectrum cartography, i.e., multiple transmitter localization and communication footprint identification, has applications in cognitive radio whitespace networking, spectrum enforcement, etc [72–74]. An accurate and fast method of obtaining up-to-date transmitter footprint information is necessary for frequency-agile networking and optimal routing of cognitive radios, while ensuring minimal interference to higher priority primary users. This work addresses this problem and explores an approach where a number of sensors are deployed in a given geographical area and their observations regarding presence of a transmitter is collected by a Fusion Center (FC) to construct the spectral usage map, as in [75]. The challenge is to devise algorithms for accurately constructing the spatial spectral usage map with a minimal number of transmissions from the sensors to the FC. Minimizing the number of transmissions helps in reducing the time taken as well as the energy efficiency in constructing the map.

Multiple transmitter localization is a recent topic of research. In [76], the authors assume the number of transmitters and their transmit powers as known, and propose localization algorithms which minimize the squared difference between the actual and predicted received powers at the sensor locations. In [77], the number of transmitters is estimated by minimizing the sum of Mean Square Error (MSE) in the location and power estimates. The above mentioned methods are based on transmitting the Receive Signal Strength (RSS) measurements from multiple sensors to a central node prior to location estimation. However, the spatial spectral usage map is inherently sparse due to the limited range of communication and the frequency reuse employed by many current-day systems. The aforementioned methods do not exploit this inherent sparsity of the spectral usage. An exception is [78], which considers the multiple target locations as sparse and uses an RSS based localization dictionary at each sensor to compressively measure the target locations. All the sensors broadcast their measurements to a central unit, where the sparse target vector is estimated. In [79], an RSS dictionary is used to solve the same problem for indoor environments. In [80], a cooperative approach for estimating the power spectral density due to multiple transmitters is proposed that exploits sparsity both due to the narrow-band nature of the transmissions as well as due to the sparsely located active transmitters. On the other hand, [75], [81] consider the localization of an uncooperative target with binary observations instead of using analog RSS measurements. Reference [81] compares centroid location estimation techniques from binary observations and concludes that the location estimate obtained using minimum enclosing circle (MEC) is the best technique.

This work considers the problem of multiple transmitter localization and footprint

identification using as few transmissions from the sensors as possible, when both the number of primary transmitters and their transmit powers are unknown. Also, sensors use one-bit on-off transmissions to convey quantized information to a central node instead of analog RSS measurements. The on-off transmission simplifies the sensor-to-FC communication, and as will be shown, it is sufficient for determining equal power contour footprints around the primary transmitter at any power level. Now, a straightforward scheme for constructing the spectral usage map is to query each of the sensors on the presence of primary transmitters in a round-robin manner, and cluster the sensors to find the primary transmitter footprint. This would require as many transmissions as the total number of sensors, since the subset of sensors that detect the primary is not known a priori. However, viewing the primary's usage footprint as sparse image, this work proposes two novel schemes based on Compressive Sensing (CS) for reducing the number of transmissions required for image recovery. In this approach, sensors simultaneously transmit their decision to the FC by pre-rotating the decision bit with a pseudo random binary phase shift. These phase shifts act as the elements of a virtual binary ensemble measurement matrix, which satisfies the restricted isometry property, allowing the use of CS-based methods for reconstructing the individual sensor decisions and reducing the number of transmissions required.

At the FC, the individual sensor decisions are reconstructed using fast sparse reconstruction techniques such as ℓ_1 minimization and Orthogonal Matching Pursuit (OMP) (e.g., [82, 83] and the references therein), and it is found that for this application, the computationally simpler OMP algorithm outperforms ℓ_1 minimization at moderate to high SNR. A novel algorithm for determining the number of primary transmitters is

proposed, and its performance is compared with the Calinski-Harbasz (CH) [84] and Hartigan [85] methods. Also, the design parameters such as the radius of the annulus within which sensors detect primary transmission, and the number of transmissions from the sensors required to enable CS reconstruction are determined based on a certain performance criterion. The performance improvement from the proposed methods is illustrated through both simulations and real-world experiments.

The transmission protocol briefly discussed above enables the FC to identify the alarming sensors. In the proposed method, there is no pilot overhead or channel estimation involved, as it is based on on-off keying. Also, this work considers dense deployment of sensors to ensure that a transmitter with a smaller transmit power is not missed. In this scenario, using multi-bit quantization increases the communication overhead, and hence a 1-bit quantization is used.

The next section presents the problem setup. In Sec. 3.2, the proposed approach for constructing primary's footprint usage map is discussed. In Sec. 3.3, the main design issues are addressed. In Sec. 3.4, the experimental results are presented. Concluding remarks are offered in Sec. 3.5.

3.1 Problem Setup

Consider a scenario (see Figure 1 (a)) where K active primary transmitters at unknown locations $l_i = (a_i, b_i)$ within an area \mathcal{A} are transmitting at unknown powers P_i . The goal is to find P_i and l_i quickly, using a low-bandwidth wireless sensor network consisting of L nodes deployed at known locations chosen uniformly at random within \mathcal{A} . The

knowledge of l_i and P_i would enable the CR network determine the *primary communication footprint*, given the minimum power at which a primary receiver can successfully receive the primary signal.

Under an isotropic signal decay model, the transmit power P_i and signal strength threshold-based detection at the sensors results in a corresponding circular region with *alarming radius* r_i around the i -th transmitter, within which the sensors detect it (such sensors are called *alarming sensors*) and communicate their decision to a FC. The path loss exponent η is assumed to be known. For simplicity, in the analysis to follow, the effect of multi-path fading and shadowing on the shape of the equal power contours around the primary transmitters is neglected. When the channel is fast varying, the effect of multi-path fading can be addressed by measuring energy at the sensors over multiple channel coherence intervals, due to which the effect of fading averages out. When the variance of shadowing parameter is small and the path loss exponent is large ($\eta = 4$ to 6 in urban environments [86]), the distortion to the circular footprint due to shadowing will also be small. The robustness of the proposed schemes to the presence of shadowing is also assessed via simulations in Sec. 3.4.

The communication radius of the primary transmitters could be different from the alarming radius. In such cases, the alarming radius is scaled appropriately based on the signal detection threshold at the sensors, to obtain the communication radius. Given that r_i is used simply as a proxy for determining P_i , it is reasonable to assume that the radio footprints are non-overlapping. That is, given the maximum transmit power of primary transmitters, P_{max} and the minimum distance between transmitters, d_{min} , one can choose the signal detection threshold employed by the sensors such that the

resulting alarming footprints are non-overlapping. The FC uses the composite received signal from the sensors to calculate l_i and P_i using a suitable algorithm (details will be presented shortly). The schemes considered here are based on simultaneous transmission from the sensor nodes, which requires symbol level synchronization across nodes. It is shown, via simulations, that the CS-based recovery is robust to both timing and frequency (of the order 100 ppm) offsets between the nodes. Also, under this model, the FC only determines the location of the alarming sensors and not their measured signal powers. This is not a drawback, since, given the primary receivers' signal detection thresholds, the alarming radius can be scaled to obtain the communication footprint of the primary network.

Since the two-dimensional spatial spectral usage map is inherently a sparse image, it can potentially be recovered using a small number of compressive measurements on the image. To do this, only a small subset of sensors that detect the presence of a signal at their location simultaneously transmit their 1-bit decision M times to the FC, and the remaining non-alarming sensors do not transmit. It is assumed that the channel stays fixed for the M transmissions.

Now, each time it is sent, the bit transmitted by each sensor is pre-rotated by a pseudo random binary phase that is known at the FC. The phase rotation employed by the i -th sensor at the j -th slot is represented by θ_{ji} , and these are realizations of independent bernoulli trials taking values 0 and π with probability 0.5 each, with $i \in \{1, 2, \dots, L\}$ and $j \in \{1, 2, \dots, M\}$. This pre-rotation is important, as it leads to a measurement matrix that is incoherent with the sparsifying basis, which in turn enables CS-based reconstruction algorithms to work. After identifying the alarming sensors at FC, the FC

localizes the primary transmitters and reconstructs the communication footprint.

Now, once the spatial spectral usage map is reconstructed at the FC, one needs an appropriate metric for evaluating the fidelity of the reconstruction. Some obvious metrics include the Mean Squared Error (MSE) in transmitter localization and the weighted sum of the MSE in the estimated transmitter locations and estimated transmitter powers. Since communication footprint reconstruction is the focus here, a more relevant metric is employed in this work: the ratio of the average error in the area of the reconstructed footprint to the area of the original image. Here, the average error is computed over the random noise, fading channel, and node placement statistics. The metric is calculated by considering the true and the reconstructed footprints, denoted \mathcal{I} and $\hat{\mathcal{I}}$, respectively, to be binary images consisting of a large number of pixels covering the area \mathcal{A} . Then, the relative error is computed as the Hamming distance between \mathcal{I} and $\hat{\mathcal{I}}$, normalized by the total number of pixels in \mathcal{A} .

3.2 Proposed Transmitter Localization and Communication Footprint Identification Schemes

The system model described in the previous section can be written as

$$y = \frac{1}{\sqrt{M}} \begin{bmatrix} x_1 e^{j\theta_{11}} & x_2 e^{j\theta_{12}} & \dots & x_L e^{j\theta_{1L}} \\ x_1 e^{j\theta_{21}} & x_2 e^{j\theta_{22}} & & x_L e^{j\theta_{2L}} \\ \vdots & & \ddots & \vdots \\ x_1 e^{j\theta_{M1}} & x_2 e^{j\theta_{M2}} & \dots & x_L e^{j\theta_{ML}} \end{bmatrix} \begin{bmatrix} h_1 \\ h_2 \\ \vdots \\ h_L \end{bmatrix} + w \quad (3.1)$$

where $y \in \mathbb{C}^M$ is the observation at the FC, h_i is the channel coefficient between sensor i and the FC, $x_i \in \{0, 1\}$ is the alarming state of sensor i , with $x_i = 1$ when the sensor is

alarming and 0 otherwise, $\theta_{ji} \in \{0, \pi\}$, $j = 1, 2, \dots, M$ represents the M pseudorandom phase shifts applied by sensor i at the M time instants, and the scaling by $1/\sqrt{M}$ is for power normalization. The additive noise $w \in \mathbb{C}^M$ is modeled as i.i.d. circularly symmetric complex Gaussian distributed with zero mean and variance σ_n^2 , and represents the thermal noise at the FC receiver. Rearranging the above,

$$y = \frac{1}{\sqrt{M}} \begin{bmatrix} +1 & -1 & \dots & +1 \\ -1 & +1 & \dots & +1 \\ & & \ddots & \\ +1 & +1 & \dots & -1 \end{bmatrix} \begin{bmatrix} x_1 h_1 \\ x_2 h_2 \\ \vdots \\ x_L h_L \end{bmatrix} + w. \quad (3.2)$$

The above representation is equivalent to the well-known compressive sensing measurement equation $y = \Phi s + w$, where Φ , the measurement matrix, is a bernoulli ensemble. Note that s is sparse because the number of primary transmitters is assumed to be small, only the small fraction of sensors that alarm transmit to the FC, and sensors are placed uniformly at random locations in \mathcal{A} .

Radio Map Reconstruction at the Fusion Center

Now, two schemes are proposed for reconstructing the map. In both schemes, the FC first reconstructs the sparse vector s from the compressed measurements y obtained from the received signals from the sensors using standard CS reconstruction techniques based on the ℓ_1 minimization or using the OMP algorithm [82,83]. The support of the recovered sparse vector is estimated by comparing the entries of the reconstructed vector to a small threshold, and this yields the set of alarming sensors. The support recovery performance is insensitive to the exact value of the threshold, since, by design, the

sparse vector recovery is successful with high probability. The FC then uses a clustering algorithm on the set of alarming sensors to estimate the number of active transmitters and their communication footprints. The two proposed schemes are illustrated in Fig. 3.1.

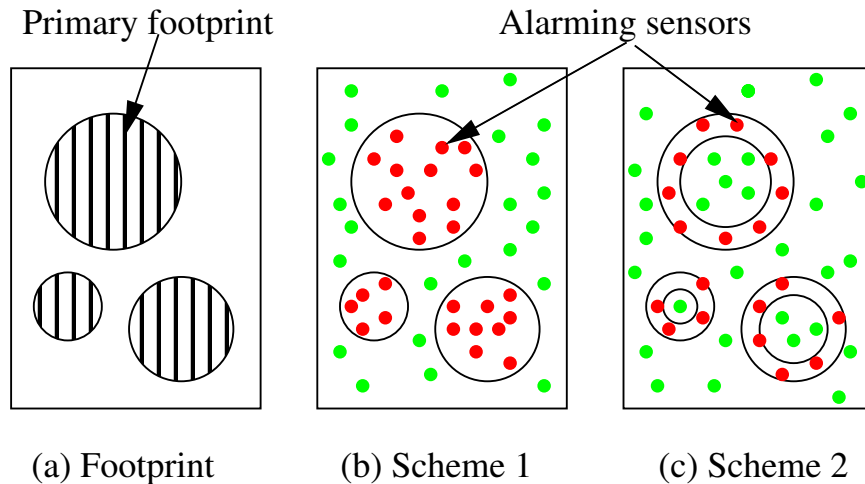


Figure 3.1: Primary footprint and alarming area in reconstruction schemes, *Scheme 1* and *Scheme 2*.

Scheme 1

In this scheme, the alarming sensors are the ones that detect a signal strength exceeding a threshold. These sensors transmit a “1” to the FC, with the pseudo-random sign change at each transmission. The alarming sensors can be assumed to lie within disjoint circular regions with radii depending on the primary transmit powers, due to the assumptions stated above. After the FC finds the locations of the alarming sensors using CS reconstruction, it uses the well-known K -means algorithm [87] to cluster them. The centroid of the cluster is treated as an estimate of the location of the primary transmitter and the alarming radius is estimated as the distance of the farthest alarming sensor of the cluster. A method for determining K , the number of transmitters, is proposed in

the next section. An approximate lower bound on MSE in localization for *Scheme 1* is found to be $A/2\pi L$ (see Appendix B.1).

Scheme 2

In this scheme, only the sensors that measure the primary power in a range between an upper and a lower threshold transmit a “1” to the FC, again with the pseudo-random sign changes. So, the reconstructed map consists of the locations of alarming sensors that lie in an annulus around each primary transmitter. The width and radius of the annulus depend on the primary transmission power and the detection thresholds. Having only the sensors in an annulus transmit is advantageous from the point of view of promoting sparsity, due to which the map can be reconstructed with fewer transmissions from the sensors compared to *Scheme 1*. Again, the K -means clustering algorithm is employed to cluster the alarming sensors and to determine the number of active transmitters. However, it turns out that the K -means centroid is a poor estimate of the transmitter location. Hence, a trilateration and a circular regression based approach is proposed here for estimating the primary transmitter locations.

The trilateration method is implemented as follows. After clustering using the K -means algorithm, a representative received power (the mean power in the annulus) is associated with all alarming sensors. Trilateration is performed by drawing an equi-power contour around every alarming sensor in a given cluster. This results in a set of contour intersections near the K -means centroid. The mean of these intersection points is used as the estimate of the transmitter location. The alarming radius of the transmitter can be estimated as in *Scheme 1*.

In the circular regression approach, the best fitting circle (in the MSE sense) is fit to

the points in a given annulus. Thus, if the primary transmitter is at (a, b) and the annulus has a mean radius r , the circular regression approach determines (a, b) and r to minimize $J(a, b, r) \triangleq \sum_i d_i^2$, where $d_i \triangleq \sqrt{(a_i - a)^2 + (b_i - b)^2} - r$, and (a_i, b_i) are the coordinates of the i -th point in the cluster. Differentiating $J(a, b, r)$ with respect to a, b and r , we get

$$\sum_{i=1}^N \frac{d_i(a_i - a)}{d_i + r} = \sum_{i=1}^N \frac{d_i(b_i - b)}{d_i + r} = \sum_{i=1}^N d_i = 0. \quad (3.3)$$

From the last equality above, $r = \frac{\sum_i \sqrt{(a_i - a)^2 + (b_i - b)^2}}{N}$, where N is the number of points in the cluster. An initial value of r is calculated with K -means centroid as the initial transmitter location. Then, any off-the-shelf algorithm such as the steepest descent algorithm can be used to estimate the transmitter location (a, b) . Finally, the radius of the footprint is estimated as the distance to the farthest point in the cluster, as before.

In summary, the proposed schemes employ M consecutive 1-bit transmissions from alarming sensors to the FC using pseudo-random phase shifts, followed by CS-based recovery of the alarming sensor locations by considering the received symbols as compressive measurements. Then, the K -means algorithm is used to cluster the alarming sensor locations. This is followed by transmitter localization using trilateration or circular regression methods to obtain the estimates of the number of primary transmitters, their locations and communication footprints.

3.3 Design Issues

3.3.1 Estimation of the Number of Primary Transmitters

The K -means clustering algorithm requires K , the number of clusters (i.e., the number of primary transmitters) as its input. To do this, various methods have been proposed in the literature that rely on intra-cluster and inter-cluster distance dissimilarity metrics computed from the data. In [88], a comparative study of these methods was presented, and it was found that the Hartigan method [85] and Calinski and Harbasz (CH) method [84] are the best ones. Note that, in the scenario under consideration, the clusters are circular or annulus-shaped. This information can be used to define a metric which robustly identifies the number of clusters. When the desired cluster is a narrow annulus, it is intuitively better to consider the distance between the points and the nearest point on a circular fit to the points within a cluster as the metric, instead of the distance to the centroid, as in past methods. The proposed algorithm is presented in Table 3.1. Although the method is described for *Scheme 2*, it is found to work well for *Scheme 1* also.

3.3.2 Sensor Detection Thresholds

The signal power thresholds for detecting primary signals at the sensors has to be determined, for a given number of sensors deployed, L , and the number of transmissions, M , from sensors to the FC. The procedure for setting the thresholds for *Schemes 1* and *2* is discussed in the following subsections.

Table 3.1: Algorithm for estimating the number of transmitters

<i>Step 1</i>	Initialize $K = 1$ transmitter.
<i>Step 2</i>	Perform K -means clustering. Fit K circles with the K -means centroids (a_i, b_i) as the centers, and the farthest point from the center in each cluster as radius r_i , for $i = 1, 2, \dots, K$.
<i>Step 3</i>	Compute the average distance metric $\mathcal{M} \triangleq \sum_{i=1}^K \frac{1}{N_i} (\sum_{j=1}^{N_i} r_i - \sqrt{(x_{ji} - a_i)^2 + (y_{ji} - b_i)^2})$, where N_i is the number of sensors in cluster i , and (x_{ji}, y_{ji}) is the location of the j -th sensor in cluster i .
<i>Step 4</i>	Increment K . Repeat <i>Step 2</i> and <i>Step 3</i> until the first minimum of \mathcal{M} is obtained.
<i>Step 5</i>	Output the K that corresponds to the first minimum.

Scheme 1

Suppose that the design requirement is to detect any transmitter emitting a power of at least P_{min} with a probability at least $1 - p_m$. Also suppose that the recovery of the sparse vector is required to succeed with probability at least $1 - p_{fsr}$. Now, the alarming radius of the i -th transmitter with power P_i is $r_i = d(P_i/\tau)^{1/\eta}$, where τ is the signal power threshold for detection at the sensors, d is a reference distance, and η is the path loss exponent. When L sensors are deployed uniformly in an area A , the probability that no sensor falls in the alarming area of a transmitter employing P_{min} power is $(1 - \pi r_{min}^2/A)^L$, where $r_{min} \triangleq d(P_{min}/\tau)^{1/\eta}$. The $1 - p_m$ requirement on this probability leads to the constraint

$$\tau \leq \left(\frac{\pi d^2}{A(1 - p_m^{1/L})} \right)^{\eta/2} P_{min} \triangleq \tau_b. \quad (3.4)$$

Recall that *Scheme 1* requires the alarming discs to be non-overlapping. Given the

maximum primary transmit power P_{max} and the minimum distance d_{min} between primary transmitters, this leads to the constraint

$$\tau \geq \left(\frac{2d}{d_{min}} \right)^\eta P_{max} \triangleq \tau_{a,1}. \quad (3.5)$$

Let K_{max} denote the number of alarming sensors when T_{max} transmitters are emitting the highest possible power P_{max} . Then, the sparse recovery requirement results in $M = O(K_{max} \log(L/K_{max}))$ number of transmissions to the FC. Then, τ needs to be chosen such that the sparse vector recovery succeeds with probability $\geq 1 - p_{fsr}$. In other words, the probability of more than K_{max} sensors falling in the alarming area should be $\leq p_{fsr}$, i.e.,

$$\sum_{i=K_{max}+1}^L \binom{L}{i} p_a^i (1-p_a)^{L-i} \leq p_{fsr}, \quad (3.6)$$

where $p_a \triangleq (\pi d^2 T_{max} / A) (P_{max} / \tau)^{2/\eta}$, is the probability that a sensor deployed falls in the alarming area. Numerically solving (3.6) for equality and choosing the largest solution $\leq \tau_b$ gives another upper bound on τ , say, $\tau \geq \tau_{a,2}$. Let $\tau_a \triangleq \max(\tau_{a,1}, \tau_{a,2})$. Thus, the sensor threshold is constrained to lie in the range $\tau_a \leq \tau \leq \tau_b$. Experimentally, it has been found that the relative error in reconstructing the communication footprint is a relatively insensitive function of the exact value of τ , provided it satisfies $\tau_a \leq \tau \leq \tau_b$. Hence, any τ in this range would yield roughly the same performance. This will be discussed in Sec. 3.4.

Scheme 2

The parameters that need to be designed here are τ_i and τ_o , the thresholds that determines the inner and outer circles of the annulus, respectively. For a transmitter with

power P_i , the inner and outer radii of alarming sensors are given by $r_i = d(P_i/\tau_i)^{1/\eta}$ and $r_o = d(P_i/\tau_o)^{1/\eta}$. Also, when the transmit power is P_{max} (similarly, P_{min}), denote the inner and outer radii by $r_{i,max}$ and $r_{o,max}$ (similarly, $r_{i,min}$ and $r_{o,min}$).

Now, since the localization algorithms in *Scheme 2* depend on approximating an annulus by a circle, the relative width of the annulus is held fixed to some value, say δ . Since this constraint needs to be satisfied for all possible transmitter powers, the first constraint is given by

$$\frac{r_{o,max} - r_{i,max}}{r_{i,max}} = \delta \Rightarrow \rho \triangleq \frac{\tau_i}{\tau_o} = (1 + \delta)^\eta. \quad (3.7)$$

Next, as in the previous subsection, the parameters need to be chosen to guarantee an upper bound on the probability of missing a transmitter, when the transmit power is P_{min} . This results in the constraint

$$\tau_o \leq \left(\frac{\pi d^2 (\rho^{2/\eta} - 1)}{A(1 - p_m^{1/L})} \right)^{\eta/2} \frac{P_{min}}{\rho} \triangleq \tau_b. \quad (3.8)$$

where p_m is the upper bound on the probability of missing a transmitter, which is given as a design requirement.

Third, one needs to ensure that the number of sensors that alarm are such that the sparse reconstruction techniques work. This leads to the constraint given by (3.6), but with p_a redefined as $p_a \triangleq (\pi d^2 T_{max} (\rho^{2/\eta} - 1)/A)(P_{max}/\rho\tau_o)^{2/\eta}$. As in the previous section, (3.6) can be numerically solved to obtain a lower bound on τ_o . Finally, the value of τ_o can be chosen empirically as the value between its lower and upper bounds that gives a minimum relative error in reconstructed footprint area; this will be illustrated in the experimental results shown in the next section.

3.4 Simulation Results

3.4.1 Monte-Carlo Simulations

The proposed schemes are simulated for footprint identification over a rectangular area having three active primary transmitters. The three transmitters are located in a (60×80) rectangular area \mathcal{A} at positions $(17, 67)$, $(42, 62)$, and $(25, 25)$ with transmit radius 7, 8 and 15, respectively. Here, for ease of presentation, no distinction is made between the actual radius of communication and the alarming radius in *Scheme 1*. Thus, in the radio map considered, the spectrum is occupied in 23% of the total area. For *Scheme 2*, the thresholds are chosen such that the width of the annulus is 3 units and the inner alarming radius is 4, 5 and 12 for the three transmitters. L sensors are deployed uniformly at random locations in the area and the alarming sensors are determined using a path loss model with $\eta = 2$ and an appropriate upper and lower energy thresholds (in *Scheme 2*) or only a lower threshold (in *Scheme 1*). The channel coefficients from the sensors to the FC are assumed to be drawn from an i.i.d. zero-mean, unit variance complex normal distribution and are assumed to be constant for the M transmissions. At the FC, the recovered complex sparse vector is quantized to a binary vector before clustering the sensors that detect the primary. The transmit power is set such that the average received SNR is 4dB per alarming sensor.

Figure 3.2 shows the results of the three metrics in identifying the number of primary transmitters. The algorithm proposed in Table 3.1 is compared with the CH and Hartigan methods in terms of their ability to find the number of clusters using 1000 instantiations of the sensor locations. The y -axis in the plot shows the metric corresponding to the method used (for e.g., with the Hartigan method, it corresponds to the Hartigan

index), along with the 99% confidence interval bars. It is found that the Hartigan and the CH methods fail to identify the true number of clusters in most instantiations of sensors for this configuration of primary transmitters, as they do not take advantage of the circular shape of the alarming areas.

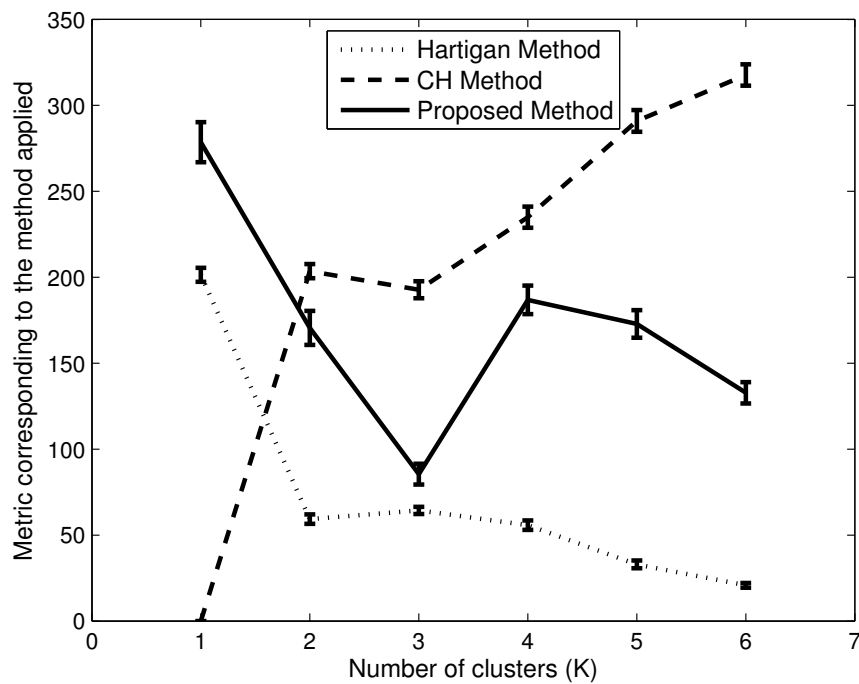
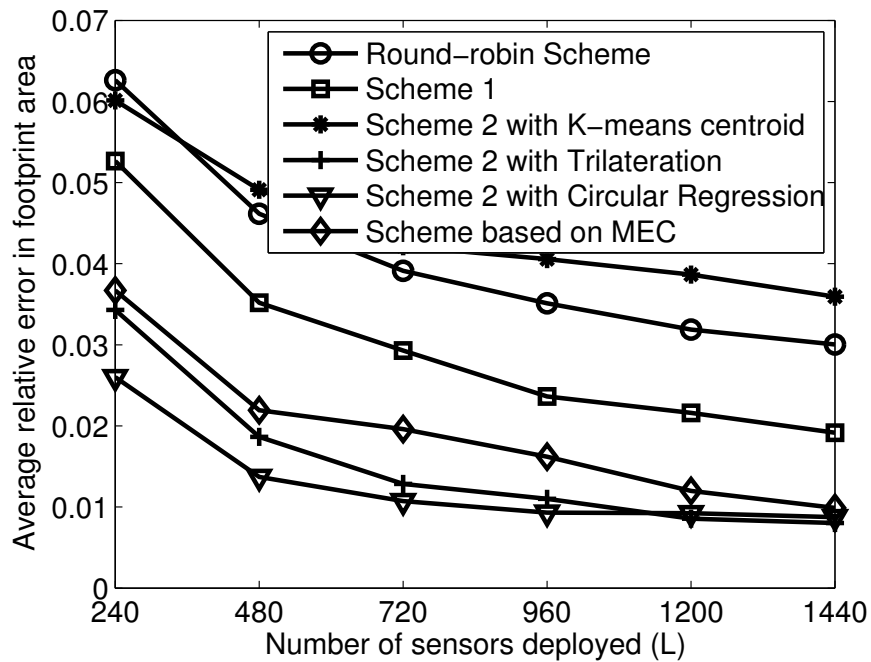


Figure 3.2: Identification of number of clusters using CH, Hartigan and proposed methods. The CH and Hartigan methods use the peak point and the first point with metric less than 100, respectively, to determine the number of clusters. Here, the true number of clusters is 3.

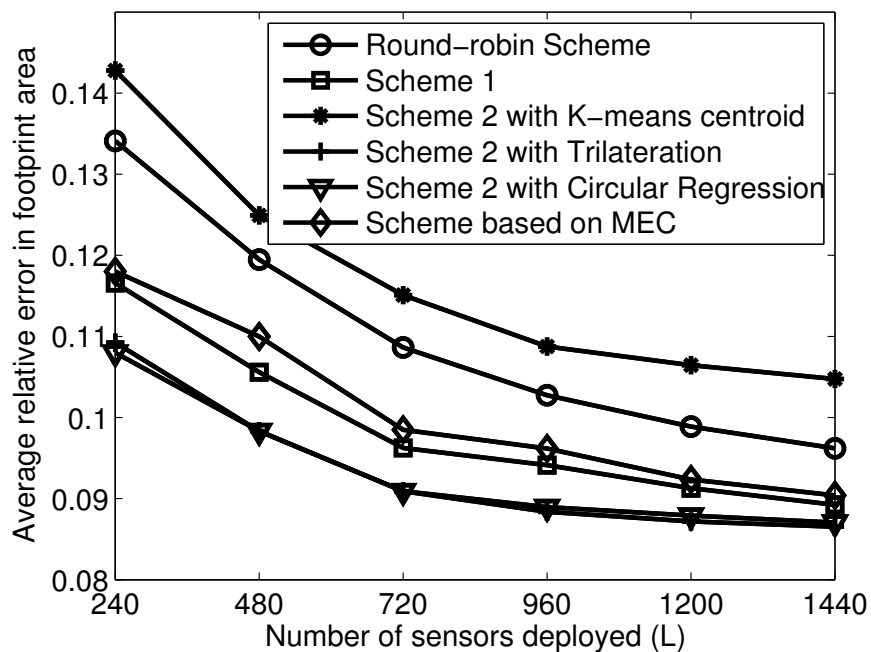
Figure 3.3(a) shows the performance comparison of the schemes versus L . In this case, as L increases, more sensors transmit on average, requiring a corresponding increase in M to ensure the CS recovery of the alarming sensor locations at the FC. The round-robin case is simulated using this value of M as the number of sensors deployed, to keep the comparison fair at each value of L , in terms of the number of transmissions to the FC. It is seen that the proposed schemes outperform the round-robin scheme. Also, the

performance improvement obtained from trilateration or circular regression methods relative to the K -means method for finding the centroid in *Scheme 2* is clear from the graph. The performance of *Scheme 2* is superior to all other schemes considered including the MEC based scheme [81]. Note that the probability of missing a transmitter is negligible here, because although the alarming radius of the lowest-power transmitter covers only 3.2% of the area A , the L considered is large, of the order of several hundreds. Figure 3.3(b) shows the performance of the schemes when the combined path loss and lognormal shadowing model is considered. Each unit on the rectangular area corresponds to $10m$ and the transmitter powers at a reference distance of $1m$ is chosen as $-3.1dBm$, $-1.9dBm$, and $3.4dBm$, respectively, which corresponds to the scenario in Fig. 3.3(a) with the path loss model. The shadowing parameter is assumed as $\sigma_s^2 = 4$ in the dB scale. The spatial correlation of the random shadowing is taken as $2^{-d_{ij}/d_{corr}}$, where d_{ij} is the distance between points i and j , and d_{corr} is the decorrelation distance, chosen as $20m$ [89]. Although there is a performance degradation in all the schemes, relative performance of the schemes is unchanged, with *Scheme 2* outperforming the other schemes. Also, the performance of the MEC based scheme degrades compared to other schemes. Thus, the proposed schemes are robust to the distortion introduced in the circular footprint due to the lognormal shadowing process.

Next, the efficacy of the different CS reconstruction methods as a function of the SNR is studied for *Scheme 2* with a deployment of $L = 960$ sensors and 122 alarming sensors. Figure 3.4 shows the percentage success of support recovery out of 1000 simulation runs versus the number of measurements. The sparse vector can be correctly reconstructed



(a)



(b)

Figure 3.3: Comparison of the round-robin scheme, *Scheme 1* and *Scheme 2*, considering (a) the path loss model and (b) a combined path loss and log-normal shadowing model. The trilateration and circular regression methods of *Scheme 2* outperform the *K*-means based centroid estimation and MEC based centroid estimation methods.

with high probability using OMP, with an SNR of 4dB per sensor and about 336 measurements at the FC. The relative error in area does not vary significantly with SNR beyond 4dB, as these schemes depend primarily on correct support recovery. Note that the greedy-search nature of the OMP algorithm implies that the few erroneous support locations identified by the OMP may still happen to fall in the annulus area, whereas, if ℓ_1 fails, it typically fails completely. Also, the success rate of the OMP has a greater dependency on the actual values of the non-zero locations than the ℓ_1 minimization. Due to these two factors, the OMP performs better than the ℓ_1 at higher SNR.

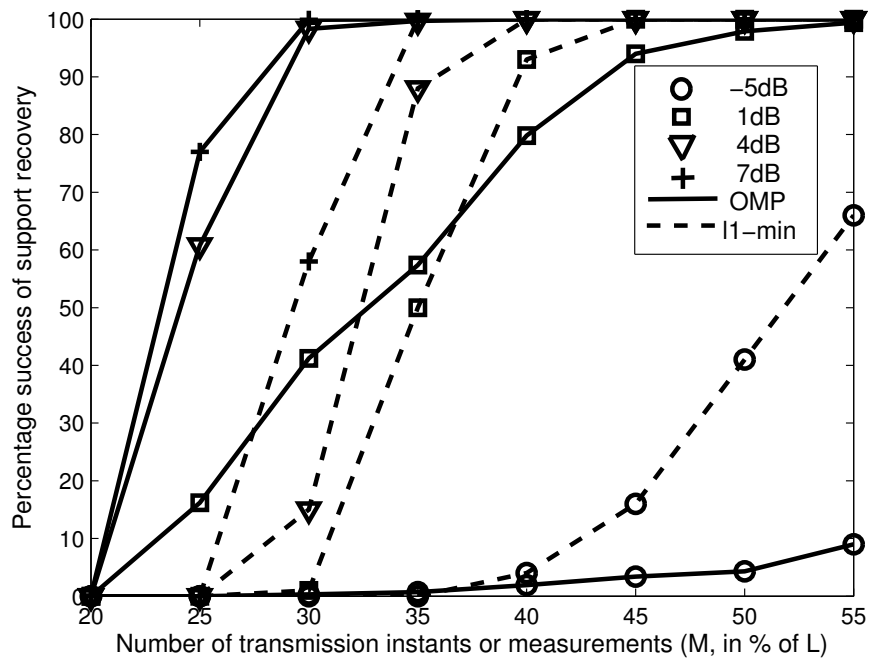


Figure 3.4: Percentage success of support recovery for ℓ_1 and OMP based CS reconstruction Vs. number of transmission instants (M) for different values of the SNR per sensor.

The procedure to select the sensor thresholds discussed in Section 3.3 is empirically evaluated and the results are listed in Tables 3.2 and 3.3. For these simulations, the transmitters were assumed to be present at positions (15, 20), (45, 20), (15, 60), and

(45, 60) of the (60×80) area. The design parameters are listed in the table; they are chosen to make the thresholds of the two schemes comparable, facilitating the comparison of their performance. Table 3.2 shows relative error in area for three different values of thresholds between τ_a and τ_b chosen through proposed design procedure, when all T_{max} transmitters are emitting at their maximum powers. In both *Scheme 1* and *Scheme 2*, for a given choice of L and M , as the threshold increases the relative area error decreases when the communication radius is roughly equal to alarming radius. On the other hand, if the alarming radius is small compared to the communication radius (which helps in CS-based recovery with a small number of transmissions), the scaling error in reconstructing the communication footprint will be large. This makes the relative error in footprint reconstruction roughly insensitive to the value of the threshold. A similar behavior is observed when the relative area error is averaged over transmitter powers being drawn from $\mathcal{U}(P_{min}, P_{max})$; this is shown in Table 3.3. This shows that any threshold value chosen in the range identified in Sec. 3.3 performs roughly equally well.

Power Budget Calculation

Here, a numerical example is provided to show that the total power used by the sensors for M transmissions in the proposed CS scheme is significantly lower than that of a round-robin scheme. Consider the setup with three primary transmitters in the (60×80) area as mentioned above, with on-off keying by the sensors. For purposes of comparison, let a failed recovery correspond to three or more errors by the support recovery algorithm. In the round-robin scheme, if 960 sensors are deployed, an SNR per sensor of 14dB ensures a probability of bit error of about $P_e = 10^{-3}$ with on-off keying, making

Table 3.2: **Evaluation of the threshold selection procedure when all $T_{max} = 4$ transmitters are emitting at $P_{max} = -1dBm$ power.** Design parameters: minimum transmit power for *Scheme 1*, P_{min} , ($-10dBm$ for *Scheme 1* and $-7dBm$ for *Scheme 2*); probability of failure of support recovery, $p_{fsr} = 0.1$; probability of missing a transmitter, $p_m = 0.15$; relative width of annulus in *Scheme 2*, $\rho = 2.0$; number of sensors, $L = 960$; number of transmissions from sensors to FC, M , (440 for *Scheme 1* and 300 for *Scheme 2*); threshold corresponding to the boundary of the communication footprint (\mathcal{F}_c) = $-20dBm$. Alarming footprint (\mathcal{F}_a).

Power threshold for <i>Scheme 1</i> (in dBm)	τ_a	$\frac{\tau_a + \tau_b}{2}$	τ_b
	-17.40	-15.90	-14.79
Relative error for <i>Scheme 1</i> with \mathcal{F}_a	0.043	0.031	0.024
Relative error for <i>Scheme 1</i> with \mathcal{F}_c	0.074	0.073	0.079
Power threshold corresponding to the outer circle of the annulus for <i>Scheme 2</i> (in dBm)	τ_a	$\frac{\tau_a + \tau_b}{2}$	τ_b
	-17.32	-15.87	-14.79
Relative error for <i>Scheme 2</i> with \mathcal{F}_a	0.035	0.026	0.020
Relative error for <i>Scheme 2</i> with \mathcal{F}_c	0.063	0.066	0.065

it comparable to the sparse technique in terms of support recovery performance. With 120 sensors alarming, the round robin scheme requires a total transmission power of $14dB \times 120$, i.e., about $35dB$.

The proposed *Scheme 2* requires a total power of about $4dB$ per sensor over the $M = 336$ transmissions for successful recovery with the OMP algorithm. This corresponds to a power requirement of $4dB \times 120$ or about $25dB$, as against the $35dB$ required by the round-robin scheme. From Figure 3.3, the relative error in the primary footprint area performance of the round-robin scheme with 960 sensors is in fact worse than that of *Scheme 2*. Hence, the power requirement of *Scheme 2* is significantly lower than that of the round-robin scheme.

Table 3.3: Evaluation of the threshold selection procedure when $T_{max} = 4$ transmitters are emitting powers drawn from $\mathcal{U}(P_{min}, P_{max})$. Design parameters are as in Table 3.2.

Power threshold for <i>Scheme 1</i> (in dBm)	τ_a	$\frac{\tau_a + \tau_b}{2}$	τ_b
	-17.40	-15.90	-14.79
Relative error for <i>Scheme 1</i> with \mathcal{F}_a	0.046	0.040	0.035
Relative error for <i>Scheme 1</i> with \mathcal{F}_c	0.082	0.093	0.075
Power threshold corresponding to the outer circle of the annulus for <i>Scheme 2</i> (in dBm)	τ_a	$\frac{\tau_a + \tau_b}{2}$	τ_b
	-17.32	-15.87	-14.79
Relative error for <i>Scheme 2</i> with \mathcal{F}_a	0.038	0.035	0.029
Relative error for <i>Scheme 2</i> with \mathcal{F}_c	0.072	0.098	0.088

Effect of Timing and Frequency Offsets Between the Nodes

First, we consider timing offsets between the nodes. A relatively small timing offset between the sensors translates to a phase offset of $\Delta_1, \Delta_2, \dots, \Delta_L$ for each of the M transmissions. Larger offsets lead to a constant degradation of signal power from each of the sensors in addition to the phase rotation; however, its effect can be handled exactly in the manner described below. Then, the system model can be represented as

$$y = \frac{1}{\sqrt{M}} \begin{bmatrix} x_1 e^{j(\theta_{11} + \Delta_1)} & x_2 e^{j(\theta_{12} + \Delta_2)} & \dots & x_L e^{j(\theta_{1L} + \Delta_L)} \\ x_1 e^{j(\theta_{21} + \Delta_1)} & x_2 e^{j(\theta_{22} + \Delta_2)} & & x_L e^{j(\theta_{2L} + \Delta_L)} \\ \vdots & & \ddots & \vdots \\ x_1 e^{j(\theta_{M1} + \Delta_1)} & x_2 e^{j(\theta_{M2} + \Delta_2)} & \dots & x_L e^{j(\theta_{ML} + \Delta_L)} \end{bmatrix} \begin{bmatrix} h_1 \\ h_2 \\ \vdots \\ h_L \end{bmatrix} + w. \quad (3.9)$$

When the phase shifts $\theta_{ji} \in \{0, \pi\}$ form a pseudorandom sequence, the above equation can be rewritten as follows:

$$y = \frac{1}{\sqrt{M}} \begin{bmatrix} +1 & -1 & \dots & +1 \\ -1 & +1 & \dots & +1 \\ & & \ddots & \\ +1 & +1 & \dots & -1 \end{bmatrix} \begin{bmatrix} x_1 h_1 e^{j\Delta_1} \\ x_2 h_2 e^{j\Delta_2} \\ \vdots \\ x_L h_L e^{j\Delta_L} \end{bmatrix} + w. \quad (3.10)$$

Note that, in order to find the alarming sensors, we only need to recover the *support* (i.e., the locations of the nonzero entries) of the unknown vector s from $y = \Phi s + w$, and not s itself. This support is unaltered by the phase offsets, and hence the proposed CS-based recovery method is robust to synchronization errors in the form of timing offsets between the nodes.

Next, we consider the effect of frequency offsets between the nodes. This does cause a perturbation in the compressive sensing measurement matrix. The IEEE 802.15.4 standard specifies a crystal accuracy of ± 40 ppm [90, 91]. Assuming a worst case frequency deviation of δf ppm, the maximum phase offset at the end of M transmissions is $\Delta_{max} \triangleq \frac{2\pi M \delta f}{10^6}$. We have simulated the effect of the frequency offset on footprint reconstruction by considering a phase error for each transmission of the sensors chosen uniformly in the interval $[0, \Delta_{max}]$ for various values of M and δf . The results for *Scheme 1* and *Scheme 2* are shown in Tables 3.4 and 3.5, respectively. The proposed methods are thus indeed robust to frequency offsets between the nodes.

Table 3.4: Percentage success of support recovery for OMP based CS reconstruction in presence of synchronization errors for *Scheme 1*, with $L = 960$.

M	δf (in ppm)				
	0	40	80	120	160
500	99	97	97	92	88
530	100	100	98	94	90
560	100	100	100	95	92
590	100	100	100	100	95

Finally, we also note that a theoretical study of the effect of perturbation on the measurement matrices has been carried out in [92]. Here, the authors consider a perturbation on measurement matrix Φ of the form $\hat{\Phi} = \Phi + E$, and derive restricted isometry

Table 3.5: Percentage success of support recovery for OMP based CS reconstruction in presence of synchronization errors for *Scheme 2*, with $L = 960$.

M	δf (in ppm)				
	0	40	80	120	160
270	96	93	92	88	87
300	100	100	99	98	96
330	100	100	100	100	98
360	100	100	100	100	100

property (RIP) constants for stable recovery. These results establish that the CS recovery methods are robust to small perturbations in the measurement matrix.

3.4.2 Experimental Results

To verify the feasibility of the proposed schemes on real-world data, an experiment was conducted in a $100\text{m} \times 160\text{m}$ football field in the Indian Institute of Science campus (the aerial view is shown in Fig. 3.5). The football field was free of interference and was suitable for simulating the free-space path loss model, but, it was surrounded by trees and walls leading to the possible reflections. Two Cisco Aironet 1242AG Series Wi-Fi Access-Points (APs) with a transmit power of 24dBm, operating on the 11th channel of the 2.4GHz band was used as the transmitter and a laptop with a Wi-Fi card was used as the receiver. The APs were placed at coordinates (50, 50) and (50, 110) relative to the center of the field, and the received power was measured at 200 randomly chosen locations over the field. The average power at a reference distance of $r_0 = 1\text{m}$ from the AP was -23dBm . It was observed that most of the measured power values were close to the corresponding calculated values obtained with a path loss exponent of two. Also, since only two transmitters were active, $T_{max} = 2$ and $P_{max} = -23\text{dBm}$ was used to



Figure 3.5: Aerial view of the football field showing the placement of Wi-Fi AP.

design the thresholds for both schemes. For a given p_m , p_{fsr} , L , M , and P_{min} , the sensor threshold levels were chosen using the discussed design procedure for *Scheme 1* and *Scheme 2*, and $\rho = 1.9$ was used in the case of *Scheme 2*.

The transmissions from the sensors to the fusion center were carried out through computer simulations, to facilitate easy comparison of the different methods using the same measured data. To evaluate the performance using $L \leq 200$ sensors, 500 independent instantiations of the subset of L out of 200 sensors were chosen uniformly from among

all possible subsets. For each instantiation, the thresholds are chosen based on the proposed design procedure, with the number of transmissions $M = 70$ and the number of sensors $L = 140$. The results are tabulated in Table 3.6. As in the case of synthetic data, it is found that the relative area error decreases with decreasing alarming radius. Also, the RMSE in localization is tabulated. In case of *Scheme 1*, the RMSE roughly follows the lower bound given by $\sqrt{A/2\pi L}$.

Table 3.6: **Evaluation of threshold selection procedure with experimental data.** Design parameters: number of transmitters, $T_{max} = 2$; maximum transmit power, $P_{max} = -23dBm$; minimum transmit power, P_{min} , ($-30dBm$ for *Scheme 1* and $-27.44dBm$ for *Scheme 2*); probability of failure of support recovery, $p_{fsr} = 0.1$; probability of missing a transmitter, $p_m = 0.15$; relative width of annulus in *Scheme 2*, $\rho = 1.9$; number of sensors, $L = 140$; number of transmissions from sensors to FC, M , (89 for *Scheme 1* and 80 for *Scheme 2*).

Power threshold for <i>Scheme 1</i> (in <i>dBm</i>)	τ_a	$\frac{\tau_a + \tau_b}{2}$	τ_b
	-51.58	-50.14	-49.06
Relative error for <i>Scheme 1</i>	0.053	0.045	0.044
RMSE for <i>Scheme 1</i>	5.12	4.46	4.30
Lower bound on RMSE for <i>Scheme 1</i>	4.26	4.26	4.26
Power threshold corresponding to the outer circle of the annulus for <i>Scheme 2</i> (in <i>dBm</i>)	τ_a	$\frac{\tau_a + \tau_b}{2}$	τ_b
	-52.60	-50.47	-49.05
Relative error for <i>Scheme 2</i>	0.049	0.034	0.029
RMSE for <i>Scheme 2</i>	3.22	2.96	2.93

3.5 Conclusions

This work proposed two novel CS based schemes for fast multiple transmitter localization and communication footprint estimation. The schemes were based on multiple simultaneous 1-bit transmissions from sensors to the FC using pseudo-random phase shifts, followed by CS-based recovery of the alarming sensor locations. Then, the alarming sensor locations were clustered using the K -means algorithm, and a novel circular

fitting technique was used to determine the number of primary transmitters. This was followed by transmitter localization using trilateration or circular regression methods to finally obtain the estimates of the number of primary transmitters, their locations and communication footprints. It was seen that the proposed schemes require fewer number of transmissions and lower power at a given fidelity level. Of the proposed schemes, *Scheme 2* performed the best in terms of the average relative error in transmitter footprint identification, for a given upper bound on the probability of missing a transmitter. The admissible range for the sensing thresholds in the two schemes was obtained using design constraints that ensured a lower bound on the probability of missing a primary transmitter and the probability of the success of the sparse vector recovery is satisfied. Two popular sparse recovery algorithms, the OMP and ℓ_1 minimization were compared, and it was found that at higher SNRs, the OMP performed better than ℓ_1 in terms of the percentage of successful recovery. The efficacy of the proposed schemes were illustrated using Monte-Carlo simulations and real-life measurements in a simple experimental setup.

Chapter 4

Target Self-Localization Using Beacon Nodes: A Column Matching Algorithm and Performance Analysis

Indoor target localization is challenging because of the unavailability of satellite-based global positioning system (GPS) in an indoor environment. Over the past two decades, there has been extensive work on using specialized infrastructure (e.g., infrared based systems [93], ultrasound waves based systems [94, 95]) for indoor localization. However, recent advances in the field of wireless sensor networks has enabled the low-cost infrastructure deployment for specific applications like intrusion detection systems, fire alarm systems, etc. In this work, deployment of a set of low-cost beacon nodes (tiny motes [96], bluetooth low energy (BLE) beacons [97]) is considered to enable the self-localization of a target node based on received signal strength (RSS) measurements from the beacons. We are particularly interested in algorithms that require very little computing capability at the target node.

In the literature, several approaches have been explored for indoor localization. One

of the early proposals was the active badge system [93], which relies on the deployment of infrared based transmitters and receivers. Similarly, Cricket [94] and BAT [95] used ultrasound waves, and LANDMARC [98] was based on RFID technology. The RF fingerprinting based approaches (like RADAR [99], HORUS [100]) use WiFi access points as transmitters and measure the received signal strengths at various locations, and then use this radio fingerprint to identify the target location. In RADAR, the target location is identified by matching the observed RSS with a database. HORUS, which has better performance compared to RADAR, uses a stochastic description of the RSS map and employs maximum likelihood estimation which needs very high computing power, usually performed on a server machine. In [101], [102] and [103], the authors consider range-free coarse-grained localization, where the centroid of the locations of the anchor nodes heard is used to estimate the target location. The coarse-grained localization approach is simple in implementation compared to RADAR and HORUS, as it avoids the need for creating and maintaining the radio fingerprint, but at the cost of poor localization. In [104], the authors conduct an experimental study of fine-grained fingerprinting based localization using BLE devices as beacon nodes. It is found that RSS values fluctuate due to fast fading, which makes RSS based localization a particularly challenging problem. Thus, solving the inverse problem of mapping RSS measurements to location estimates is a computationally challenging task when accurate location estimates are desired. To this end, in this work, we propose a virtual-grid based localization technique based on connecting the inverse problem to non-adaptive group testing, and draw on the computationally efficient recovery algorithms in the latter field.

Motivation: An application of interest is tracking the position of a target, say, a worker

on the factory floor, or a doctor/nurse in a hospital, within an area of interest. Knowledge of the movement patterns of factory workers or hospital staff can lead to streamlining of the process and is also useful for implementing safety systems such as warning against entering hazardous areas, etc. To this end, a set of beacon nodes (motes) are deployed in the area of interest. These motes periodically broadcast their location and identification number (id) to assist in the localization process. An application running on the target device (e.g., a mobile phone) attempts to 'read' the beacons. Based on the subset of beacons it is able to read, the target estimates its location. Such an approach of decentralized coordination requires no additional hardware to be carried by the targets (e.g., it can be implemented as an application running on a smart phone), and is cost-effective given the availability of low-cost tiny motes that can be used as beacon nodes. Another application of interest is in the geo-location database approach for enabling cognitive radio (CR) spectrum access. Here, a white space device (WSD) communicates its location to a central database and obtains information to set its parameters for secondary access of the licensed band. To this end, the self-localization of a WSD is a crucial step in enabling CR operation. In this case, a set of cellular base-stations or the Wi-fi access points (in case of a fully connected city) can act as beacon nodes to enable localization.

Proposed Approach: We divide the area of interest, denoted by \mathcal{A} , into a rectangular grid whose size depends on the desired target localization error. Then, the problem of target localization reduces to that of determining the grid point that, among all the candidate grid locations, best explains the measurement (reading) of the beacon nodes at the target. We relate this problem to that of testing the grid cells for the presence of

the target node and propose a column-matching algorithm [105] for self-localization of the target node at a given accuracy level. The column-matching algorithm is a computationally inexpensive algorithm proposed in the context of non-adaptive group testing (NGT) [106]. In doing so, we provide a bridge connecting the vast areas of target localization and group testing, that can be useful in many different applications.

On the analytical side, we leverage results from stochastic geometry and order statistics to determine the minimum spatial density of beacon nodes required to achieve a desired localization performance. Stochastic geometry is a powerful tool that has recently been used in wireless communications for performance analysis when the transmitters and receivers are located randomly [107]. Our main contributions in this context are as follows:

1. We propose a novel measurement scheme for enabling target self-localization using received power readings from a set of low-power beacon nodes.
2. We propose the use of multiple power thresholds at the target along with a grid-based localization framework for reducing the number of nodes to be deployed and achieving a desired localization accuracy. Roughly speaking, the number of nodes deployed can be traded-off for the number of measurements (power thresholds) per node, provided the different power thresholds are chosen judiciously.
3. We mathematically relate the problem of target self-localization to that of testing grid cells for the presence of the target. Based on this connection, we propose to use a computationally efficient column-matching based algorithm popular in the context of NGT literature, for target self-localization.

4. We analyze the localization performance by considering the spacings between the successive intersections of the power contours of the beacons on the grid cells. The tools from order statistics and Poisson point processes are utilized to characterize the length of the spacings, and in turn, this is used to determine the density of nodes required to localize the target to a desired level of accuracy.

The proposed approach and results obtained are validated via Monte Carlo simulations as well as experimental data collected at the Robert Bosch Centre for Cyber Physical Systems, Indian Institute of Science, Bangalore. The results show that proposed algorithm is a promising approach for beacon-based target self-localization.

The next section discusses the system model and problem setup. In section 4.2, the proposed localization algorithm is discussed. Section 4.3 presents the analytical procedure for determining the number of motes that need to be deployed. In section 4.4, simulation and experimental results are provided to illustrate the performance of the proposed algorithms. Section 4.5 concludes the chapter.

Notations: Boldface capital letters denote matrices, boldface small letters denote vectors, and $(.)^t$ denotes the transpose of a matrix. The notation $\text{supp} \{\max\{\mathbf{z}\}\}$ represents the set of indices for which the corresponding entry of \mathbf{z} equals the maximum value in \mathbf{z} .

4.1 System Model and Problem Setup

Consider a passive target located at (x_t, y_t) in a geographical area denoted by \mathcal{A} . To facilitate the self-localization of the target node, a set of K beacon nodes $b_1, b_2, \dots, b_i, \dots, b_K$ are deployed uniformly at random locations in and around \mathcal{A} . The transmissions from

each beacon node conveys its identity and location. The target node first determines the subset of beacons it is able to receive the ids from. Then, the target node computes a binary vector based on the RSS, as explained below. This binary information of the measurements from the beacon nodes, along with an offline collected database of the RF footprint of beacon readings over the area \mathcal{A} is used to localize the target, i.e., to estimate (x_t, y_t) . Alternatively, if the well known path loss model for RF signal propagation is applicable in the area \mathcal{A} , it could be employed to construct the RF footprint database. For simplicity of exposition, in the sequel, we consider the path loss model for RF signal propagation. When a beacon node b_i transmits with a power P_0 , the RSS value observed at the target node, denoted by $P_{rx,i}$ is given by $P_{rx,i} \triangleq \min(P_0, P_0(d_0/d_i)^\eta)$, where η is the path loss exponent, d_0 is a reference distance, and d_i is the distance between b_i and the target node. The target node compares the RSS value $P_{rx,i}$ with M predetermined intervals, $\{\mathcal{I}^{(j)} \triangleq (P_{th}^{(j-1)}, P_{th}^{(j)}] : j = 1, \dots, M, P_{th}^{(0)} = P_0\}$, and sets the *reading* (denoted by $y_i^{(j)}$) corresponding to b_i and $\mathcal{I}^{(j)}$ using the following rule:

$$y_i^{(j)} \triangleq \begin{cases} 1, & P_{th}^{(j-1)} > P_{rx,i} \geq P_{th}^{(j)} \\ 0, & \text{else.} \end{cases} \quad (4.1)$$

That is, the vector $[y_i^{(1)}, y_i^{(2)}, \dots, y_i^{(M)}]_t$ is a binary vector with either all zeros (if b_i is not “visible” at the target), or with a single 1 corresponding to the threshold interval in which the received power at the target lies. In this fashion, the target node aggregates all the $y_i^{(j)}$ s to form a binary decision vector $\mathbf{y} \triangleq [y_i^{(j)}] \in \{0, 1\}^{T \times 1}$, where $T \triangleq KM$ is the total number of measurements at the target.

The geographical area \mathcal{A} is divided in to a rectangular grid of size $L_1 \times L_2$. Under the above setup, the goal in this chapter is to determine the grid or a subset of the grid

locations that are closest to the target location among the $C \triangleq L_1 L_2$ possible candidate locations, using the binary observation vector y .

Our performance measure is the probabilistic accuracy with which the location estimate is within a given small number of grid cells near the actual location. That is, it is possible that the localization algorithm could identify a set of nearby grid locations as the ones that best explain the reading at the target. We seek guarantees of the form: the maximum localization error is within (say) 1 m with 99% probability, if the target is uniformly distributed on \mathcal{A} . By deploying sufficient number of beacon nodes, the localization uncertainty can be made to meet the desired accuracy level. Thus, we have two problems at hand: to come up with an algorithm to identify the grid location(s) corresponding to the binary reading y at the target node, and to analytically characterize the relationship between the number of beacon nodes and the localization accuracy.

Note that, along with the beacon nodes deployed in the area of interest \mathcal{A} , the nodes deployed in the vicinity of \mathcal{A} also help in localization of the target. This enables the target localization to the desired accuracy uniformly all over the grid in \mathcal{A} with reduced node density. For example, if a room in the building is the area of interest, then the beacon nodes deployed in the adjoining rooms/corridor help in localization along with the nodes in the room. Also, the target can be localized with reduced accuracy in the region surrounding the area of interest.

4.2 A Column Matching Algorithm for Localization

In this section, we cast the target localization problem as the one of testing the grid cells for the presence of target. Our starting point is the measurement model described in

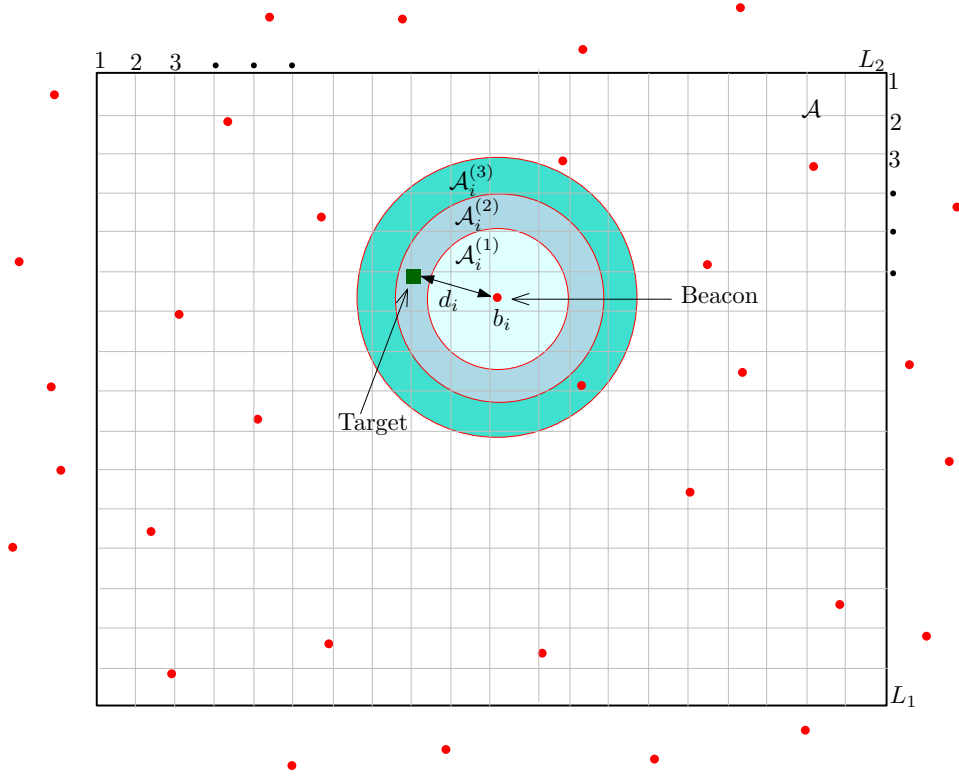


Figure 4.1: Illustration of the measurement process for target sensor localization. Red dots represent the beacon nodes and green square block represents the target node.

the previous section and pictorially shown in Fig. 4.1. The measurement procedure described in the previous section is mathematically equivalent to *testing* for the presence of the target node in one of the concentric annuli around the beacons, with each annulus corresponding to a different threshold interval at the target. That is, for the test corresponding to j^{th} threshold interval of the i^{th} beacon's signal, the grid cells in the annulus $\mathcal{A}_i^{(j)}$ are tested. This can be represented by the test vector $\mathbf{a}_i^{(j)} \in \{0, 1\}^{1 \times C}$, where $C \triangleq L_1 L_2$ is the total number of grid cells. In $\mathbf{a}_i^{(j)}$, the entries corresponding to the cells being tested are set to 1 and the remaining entries are set to 0. Thus, the measurement process can be written as

$$\mathbf{y} = \mathbf{A}\mathbf{x}, \quad (4.2)$$

where $\mathbf{A} \in \{0, 1\}^{T \times C}$ is the test matrix formed by stacking the row vectors $\mathbf{a}_i^{(j)}$, and $\mathbf{x} \in \{0, 1\}^{C \times 1}$ indicates the true position of the target. The unknown vector \mathbf{x} has one of its elements being set to 1: this corresponds to the cell where the target is present.

Under this setup, the problem of target localization reduces to that of identifying the position of the '1' in the vector \mathbf{x} , using the reading \mathbf{y} obtained at the target. Since we consider the case where the number of beacons is $\ll C$, the above is an under-determined system of linear equations, and we seek the sparsest solution. We propose to employ the column matching algorithm from the group testing literature (e.g., [105]) to identify the location of the "1" in \mathbf{x} , i.e., the target location. The column-matching algorithm attempts to match the columns of \mathbf{A} with test result vector \mathbf{y} . In particular, any column of \mathbf{A} that has maximum number of entries where the 1s coincide with \mathbf{y} is a potential target location, i.e.,

$$\mathcal{K} = \text{supp} \{ \max \{ \mathbf{A}^t \mathbf{y} \} \}, \quad (4.3)$$

where \mathcal{K} is the set of defective items (ones). Note that, in the target localization problem, the goal is to identify a single entry of 1, as an estimate of the target location. However, when multiple grid cells receive the beacon transmissions in the same RSS intervals, multiple grid cells could return the same reading, and it is not possible to uniquely localize the target within a grid cell. In such a scenario, the centroid of the grid cells corresponding to '1's in \mathbf{x} is used to identify the target location. The probability of localizing the target within a grid cell can be increased by increasing the number of tests, $T = KM$. The trade-off between K , M , and the accuracy of localization is studied via analysis and experiments.

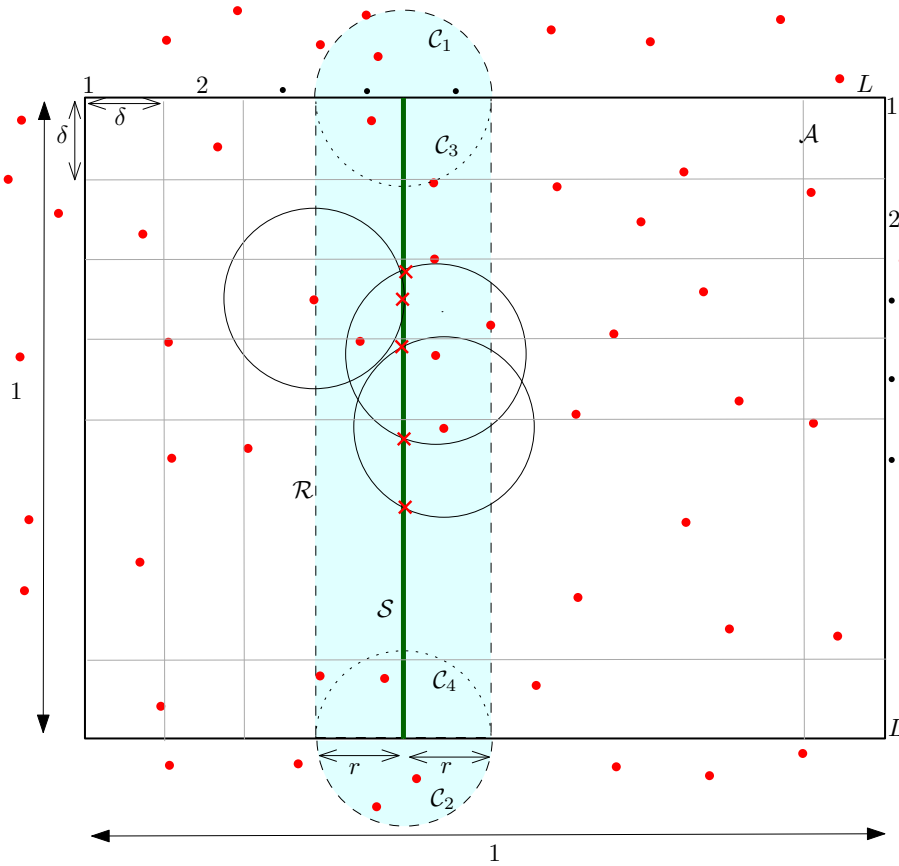


Figure 4.2: Illustration of the beacon power contours intersecting line segment S . The power contours of the beacon nodes located in the cyan colored strip intersect S .

4.3 Performance Analysis

As discussed above, the goal is to localize the target within its actual grid cell with high probability. In other words, each grid cell is uniquely identified by a distinct set of intersections from annuli corresponding to different beacon transmissions and power threshold intervals. Thus, to analyze the localization performance, it becomes important to study these intersections on the grid cells and quantify their spacings. This analysis aids in determining the minimum number of beacon nodes required.

4.3.1 Probability of Localizing the Target within a Grid Cell

Suppose the locations of the beacon nodes form a Poisson point process (PPP) Φ of intensity λ on the \mathbb{R}^2 plane. Consider a target located uniformly at random in the area of interest \mathcal{A} . For concreteness, as depicted in Fig. 4.2, \mathcal{A} is taken to be a square area of dimension 1×1 , divided into a $L \times L$ square grid, with each grid cell of size $\delta \times \delta$, i.e. $\delta \triangleq \frac{1}{L}$. To simplify the exposition, consider a single power threshold $P_{th}^{(1)}$ at the target, and let the communication radius of the beacon nodes corresponding to $P_{th}^{(1)}$ be r . That is, the received power at the target is greater than or equal to $P_{th}^{(1)}$ for the beacon nodes that are located within a distance of r from the target. The first step in our analysis is to determine the locations of the intersections of the beacon power contours of radius r on any vertical/horizontal line segment \mathcal{S} of length 1 in \mathcal{A} . These intersections are important for determining the localization accuracy, because a target present in the spacing between a pair of successive intersections can be localized within the spacing. To quantify the length of these spacings, it is required to determine the distribution of the intersections on \mathcal{S} . This is presented in Lemma 3.

Lemma 3. *When the beacon nodes are distributed as PPP with intensity λ , the number of beacon nodes with power contours of radius r intersecting \mathcal{S} is Poisson distributed with mean $\mu_1 = \lambda(2r + \pi r^2)$. The total number of such intersections N on the line segment \mathcal{S} is approximately Poisson distributed with mean $\mu = 4\lambda r$.*

Proof. As in Fig. 4.2, consider a region \mathcal{R} formed by a rectangular strip of size $1 \times 2r$ and two semi-circular strips \mathcal{C}_1 and \mathcal{C}_2 of radius r . The beacon nodes that lie in this region intersect the line segment \mathcal{S} . Thus, the average number of beacon nodes that intersect

\mathcal{S} is

$$\mu_1 = \lambda(\text{Area of } \mathcal{R}) = \lambda(2r + \pi r^2). \quad (4.4)$$

Since the number of points of the point process Φ that lie in the region \mathcal{R} is Poisson distributed, the number of beacon nodes intersecting \mathcal{S} is Poisson distributed.

Further, for $r \leq 1/2$, the nodes that lie in the region \mathcal{R} but not in $\mathcal{C}_1, \mathcal{C}_2, \mathcal{C}_3$, and \mathcal{C}_4 intersect \mathcal{S} twice, whereas, the nodes that lie in $\mathcal{C}_1, \mathcal{C}_2, \mathcal{C}_3$, and \mathcal{C}_4 intersect only once. Thus, the mean of the number of intersections on \mathcal{S} is given by

$$\begin{aligned} \mu &= 2\lambda(\text{Area of } \mathcal{R} - \text{Sum of area of } \mathcal{C}_1, \mathcal{C}_2, \mathcal{C}_3 \text{ and } \mathcal{C}_4) \\ &\quad + \lambda(\text{Sum of area of } \mathcal{C}_1, \mathcal{C}_2, \mathcal{C}_3 \text{ and } \mathcal{C}_4), \end{aligned} \quad (4.5)$$

$$= 2\lambda(2r - \pi r^2) + \lambda(2\pi r^2) = 4\lambda r. \quad (4.6)$$

For $r > 1/2$, following a similar procedure, it can be shown that $\mu = 4\lambda r$.

The beacon nodes that intersect twice on \mathcal{S} leads to dependent intersecting points. However, this dependency is weak for a sufficiently large r , as the proportion of circles intersecting once will be more than the ones intersecting twice. Thus, it can be deduced that the number of intersections N on \mathcal{S} is approximately Poisson distributed with mean $4\lambda r$. \square

In practice, due to fading, beacon power contours are random shapes (see section 4.1 of [108] for a discussion on the Poisson-ness of independent random shapes), this further reduces the dependent intersections.

As a consequence, conditioned on the number of intersections N , say, given $N = n$, the

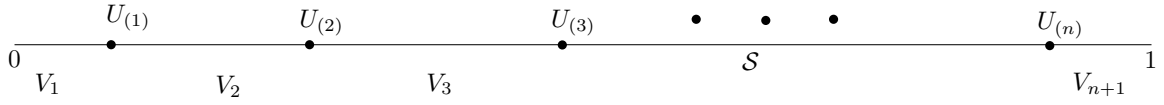


Figure 4.3: Depiction of the intersections on line segment \mathcal{S} as uniform ordered variates and their spacings.

location of intersections U_1, U_2, \dots, U_n on the line segment \mathcal{S} are distributed as uniform and independent in the range $[0, 1]$. Suppose that $0 \leq U_{(1)} \leq U_{(2)} \leq \dots \leq U_{(n)} \leq 1$ represent the order statistics of the independent uniform random variates (r.v.s) (see Fig. 4.3). Let the spacing between any two successive ordered r.v.s be $V_i \triangleq U_{(i)} - U_{(i-1)}$, $i = 1, 2, \dots, n + 1$, where $V_{n+1} = 1 - U_{(n)}$ and $V_1 = U_{(1)}$. Each of these spacings V_1, V_2, \dots, V_{n+1} should be made smaller than the grid cell size with sufficiently high probability. Equivalently, the largest of these spacings,¹ the ordered r.v. $V_{(n+1)}$ must be confined within the grid cell size with high probability. So, it is required to evaluate the quantity $\Pr(V_{(n+1)} \leq \delta)$: this is presented in Lemma 4.

Lemma 4. *The cumulative distribution function (cdf) of the largest among the spacings between successive ordered uniform r.v.s in the range $[0, 1]$ is given by*

$$\Pr(V_{(n+1)} \leq \delta) = 1 - \sum_{k=1}^{\min(n+1, L-1)} (-1)^{k-1} \binom{n+1}{k} (1 - k\delta)^n, \quad (4.7)$$

where $n \geq 0$, $\delta \in (0, 1)$ and $\delta \triangleq \frac{1}{L}$.

Proof. This is derived in section 6.4 of [109]. For the sake of completeness, a brief sketch of the proof is provided here. Using the well-known Boole's formula, the probability of

¹In this work, the notation U_i denote the unordered random variables, while $U_{(i)}$ denotes the i^{th} random variable ordered in increasing order. The same notation is used for the random variables V_i also.

the occurrence of at least one of the events $V_i > \delta$ can be expressed as

$$\begin{aligned} Pr \left\{ \bigcup_{i=1}^{n+1} (V_i > \delta) \right\} &= \sum_i Pr(V_i > \delta) - \sum_{i < j} Pr(V_i > \delta, V_j > \delta) \\ &+ \dots + (-1)^n Pr(V_1 > \delta, V_2 > \delta, \dots, V_{n+1} > \delta). \end{aligned} \quad (4.8)$$

To evaluate equation (4.8), the joint distribution of k events $V_1 > \delta, V_2 > \delta, \dots, V_k > \delta$ is given by [109]

$$Pr(V_1 > \delta, V_2 > \delta, \dots, V_k > \delta) = (1 - k\delta)^n, \text{ for } k\delta < 1, \quad (4.9)$$

and the distribution in (4.9) is symmetrical in V_i (i.e., V_i s are exchangeable in the joint distributions). Thus, along with the fact that the union event $\bigcup_{i=1}^{n+1} (V_i > \delta)$ is the same as $(V_{(n+1)} > \delta)$, (4.8) can be expressed as

$$Pr(V_{(n+1)} > \delta) = \sum_{k=1}^{\min(n+1, L-1)} (-1)^{k-1} \binom{n+1}{k} (1 - k\delta)^n. \quad (4.10)$$

Hence, the cdf of the largest spacing is given by (4.7). \square

The number of intersections N is Poisson distributed, thus, the average probability of the event $V_{(N+1)} \leq \delta$ is derived by taking expectation over N . This is presented in Theorem 1.

Theorem 1. *The average probability of the largest spacing between successive intersections being less than or equal to the size of the grid cell, when the number of intersections N is Poisson distributed with mean μ , is given by*

$$\mathbb{E} [Pr(V_{(N+1)} \leq \delta)] = 1 - \sum_{k=1}^{L-1} \frac{e^{-k\delta\mu} [\mu(1 - k\delta) + k] [-\mu(1 - k\delta)]^{k-1}}{k!} \quad (4.11)$$

where $\delta \triangleq \frac{1}{L}$.

Proof. The term $\mathbb{E} [Pr(V_{(N+1)} > \delta)]$ is given by

$$\begin{aligned} \mathbb{E} [Pr(V_{(N+1)} > \delta)] &= \sum_{n=0}^{\infty} Pr(V_{(n+1)} > \delta) Pr(N = n) \\ &= \sum_{n=0}^{\infty} \sum_{k=1}^{\min(n+1, L-1)} (-1)^{k-1} \binom{n+1}{k} (1 - k\delta)^n \frac{e^{-\mu} \mu^n}{n!}. \end{aligned} \quad (4.12)$$

Changing the order of summation, we get the following equivalent expression:

$$\mathbb{E} [Pr(V_{(N+1)} > \delta)] = \sum_{k=1}^{L-1} \sum_{n=k-1}^{\infty} (-1)^{k-1} \binom{n+1}{k} (1 - k\delta)^n \frac{e^{-\mu} \mu^n}{n!}. \quad (4.13)$$

This can be further simplified as follows

$$\begin{aligned} \mathbb{E} [Pr(V_{(N+1)} > \delta)] &= e^{-\mu} \sum_{k=1}^{L-1} \frac{(-1)^{k-1}}{k!} \sum_{n=k-1}^{\infty} \frac{(n+1)}{(n+1-k)!} [\mu(1 - k\delta)]^n, \\ &= e^{-\mu} \sum_{k=1}^{L-1} \frac{(-1)^{k-1}}{k!} \left[\sum_{n=k-1}^{\infty} \frac{(n+1-k)}{(n+1-k)!} [\mu(1 - k\delta)]^n \right. \\ &\quad \left. + \sum_{n=k-1}^{\infty} \frac{k}{(n+1-k)!} [\mu(1 - k\delta)]^n \right]. \end{aligned} \quad (4.14)$$

The inner summation terms are Taylor series expansions of the scaled exponential function in $\mu(1 - k\delta)$, so (4.14) can be expressed as

$$\mathbb{E} [Pr(V_{(N+1)} > \delta)] = e^{-\mu} \sum_{k=1}^{L-1} \frac{(-1)^{k-1}}{k!} [[\mu(1 - k\delta)]^k + k[\mu(1 - k\delta)]^{k-1}] e^{\mu(1-k\delta)}. \quad (4.15)$$

Further, equation (4.15) is used to obtain the average probability of largest spacing given in (4.11). \square

Next, consider multiple thresholds $P_{th}^{(1)} > P_{th}^{(2)} > \dots > P_{th}^{(M)}$ at the target, and let the corresponding communication radii of the beacons be $r_1 < r_2 < \dots < r_M$. Then,

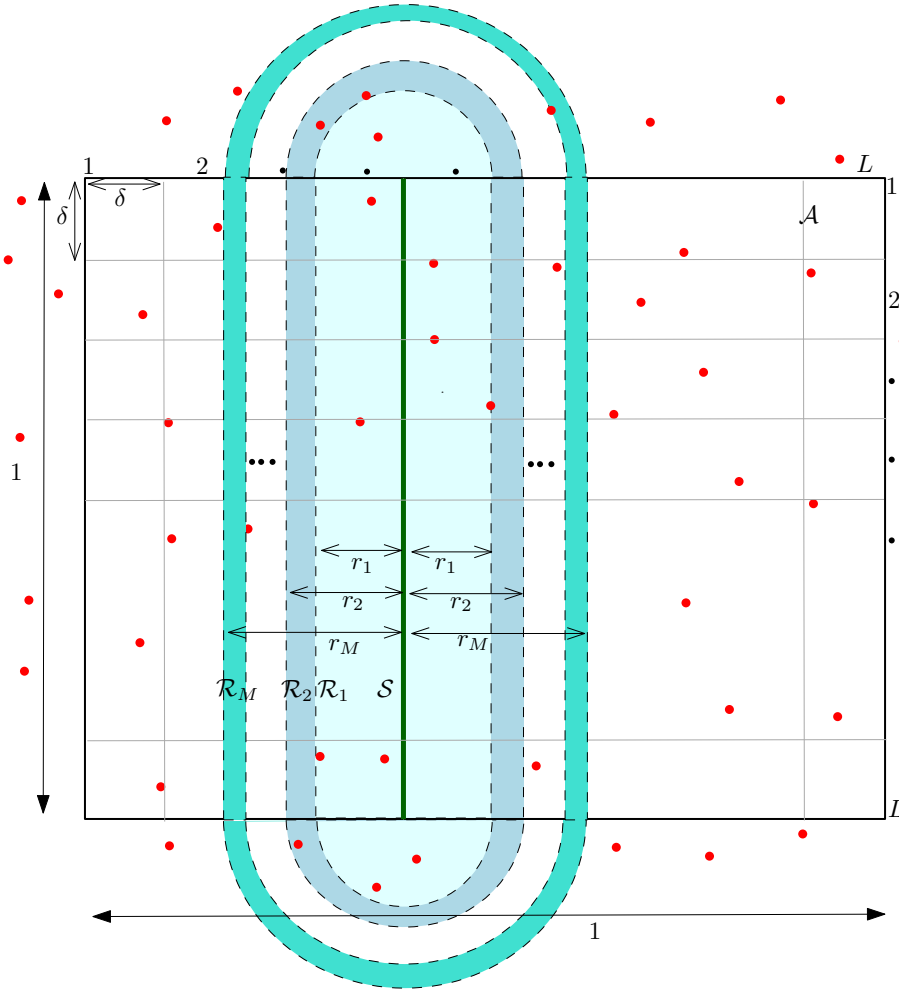


Figure 4.4: Illustration of the multiple power contours from beacons intersecting line segment S .

as a sequel to Lemma 3, the average number of intersections on the line segment S is presented in Lemma 5.

Lemma 5. *When the beacon nodes' M power contours of radii $r_1 < r_2 < \dots < r_M$ intersect S , the average number of intersections on S is given by $\mu = 4\lambda\bar{r}M$, where $\bar{r} = \frac{\sum_{j=1}^M r_j}{M}$ is the average radius.*

Proof. As shown in Fig. 4.4, for any node present in the region $\mathcal{R}_1, \mathcal{R}_2, \dots, \mathcal{R}_M$, the

number of power contours that intersect the line segment \mathcal{S} is $M, M - 1, \dots, 1$, respectively. Therefore, using Lemma 3, the average number of intersections on \mathcal{S} is given by

$$\begin{aligned}\mu &= 4\lambda[r_1M + (r_2 - r_1)(M - 1) + \dots + (r_M - r_{M-1})] \\ &= 4\lambda \sum_{j=1}^M r_j \\ &= 4\lambda\bar{r}M,\end{aligned}\tag{4.16}$$

where $\bar{r} = \frac{\sum_{j=1}^M r_j}{M}$ is the average radius. \square

The average probability of largest spacing being less than or equal to the size of the grid cell for the M threshold case can be obtained by substituting $\mu = 4\lambda\bar{r}M$ in equation (4.11). As discussed earlier in Lemma 3, in the M threshold scenario too, multiple intersections of the same beacon node on \mathcal{S} causes dependent intersections. However, in this case, the width of the annuli can be chosen in a planned manner based on the size of the grid cell. As we will see from simulations in the next section, this structured choice of the widths of the annuli reduces the number of intersections required on \mathcal{S} , thereby reducing the node density required to achieve the desired localization accuracy.

To gain intuitive understanding, an approximation to $\mathbb{E} [Pr(V_{(N+1)} \leq \delta)]$ in (4.11) is derived as follows. The average probability $\mathbb{E} [Pr(V_{(N+1)} > \delta)]$ in (4.15) is derived using the principle of inclusion and exclusion as represented by Boole's formula in (4.8). Because of this, for the right choice of μ for a given δ , $\mathbb{E} [Pr(V_{(N+1)} > \delta)]$ can be upper bounded by the first term of the summation in (4.15), i.e.,

$$\mathbb{E} [Pr(V_{(N+1)} > \delta)] \leq e^{-\delta\mu}[\mu(1 - \delta) + 1].\tag{4.17}$$

Therefore, a lower bound on $\mathbb{E} [Pr(V_{(N+1)} \leq \delta)]$ is given by

$$\mathbb{E} [Pr(V_{(N+1)} \leq \delta)] \geq 1 - e^{-\delta\mu} [\mu(1 - \delta) + 1]. \quad (4.18)$$

For a small δ (< 0.2) and relatively large μ (> 10), $\mu(1 - \delta) + 1 \approx \mu\delta(L - 1) \approx \mu$, thus, the R.H.S. of (4.17) can be further simplified as

$$\mathbb{E} [Pr(V_{(N+1)} \leq \delta)] \approx 1 - \mu e^{-\delta\mu} = 1 - (4\lambda\bar{r}M)e^{-\delta(4\lambda\bar{r}M)}. \quad (4.19)$$

For the choice of parameters considered, it is found through simulations that (4.19) is a good approximation to (4.11). From (4.19), it is clear that the parameters λ , \bar{r} and M can be traded off for each other to achieve a given average probability of localizing within a grid cell. For e.g., λ or \bar{r} can be reduced by half by doubling M and vice-versa. Also, for a fixed δ , the average probability tends to 1 exponentially with increase in μ , since the exponential term in (4.19) is dominant for sufficiently large μ . Similarly, for a fixed μ , as grid cell size δ is increased, the average probability of localizing within a grid cell approaches unity exponentially fast.

4.3.2 Optimal Beacon Density

The number of beacon nodes are chosen such that the average probability of detecting the target within the grid, equation (4.11), is at least p , where p is a design parameter. Alternatively, the node density can be obtained by using the approximation in (4.19) and setting it to be at least p . For a given p , numerically solving (4.11) or (4.19) for equality, the density of the number of intersections μ can be obtained, and substituted in $\lambda = \frac{\mu}{4\bar{r}M}$ to obtain the node density. The proposed design procedure is validated in

the next section.

4.4 Numerical Results

4.4.1 Monte Carlo Simulations

For the simulations, we consider a square area \mathcal{A} of size (a, a) . The area \mathcal{A} is divided into grids of sizes $(5, 5)$, $(10, 10)$, $(20, 20)$, etc., and the location of the target node is chosen uniformly at random over \mathcal{A} . The locations of the beacon nodes form a PPP of intensity λ on the \mathbb{R}^2 plane. The M power thresholds at the target are chosen such that the annulus width is equal to the size of the grid cell. In the offline phase, the test matrix \mathbf{A} is evaluated for a free-space path loss model ($\eta = 2$). In the online phase, the column-matching algorithm in (4.3) is used to identify the target locations. The simulations are performed by considering 10000 location instantiations, with identifying target location to an accuracy of single grid cell for 90% of instantiations as the performance criterion.

As discussed in section 4.3.1, the product of the node density and the beacon radius (λr) indicates the number of intersections on the line segment \mathcal{S} . When a single power threshold is considered at the target, Fig. 4.5 shows the required λr product to localize within a grid cell with probability $p = 0.9$ vs beacon radius for desired grid cells of size $\delta = 0.2, 0.1,$ and 0.05 . The required λr product nearly doubles as the grid cell size is reduced by half. For all the three cases, it is observed that the required λr product is slightly more than the theoretical value satisfying (4.11). As explained earlier, this is because of the dependent intersections of the power contours of the beacon nodes that intersect twice on the line segment \mathcal{S} . However, the gap between the theoretical and simulation curves reduces with increasing radius, also with, reducing grid cell size, as

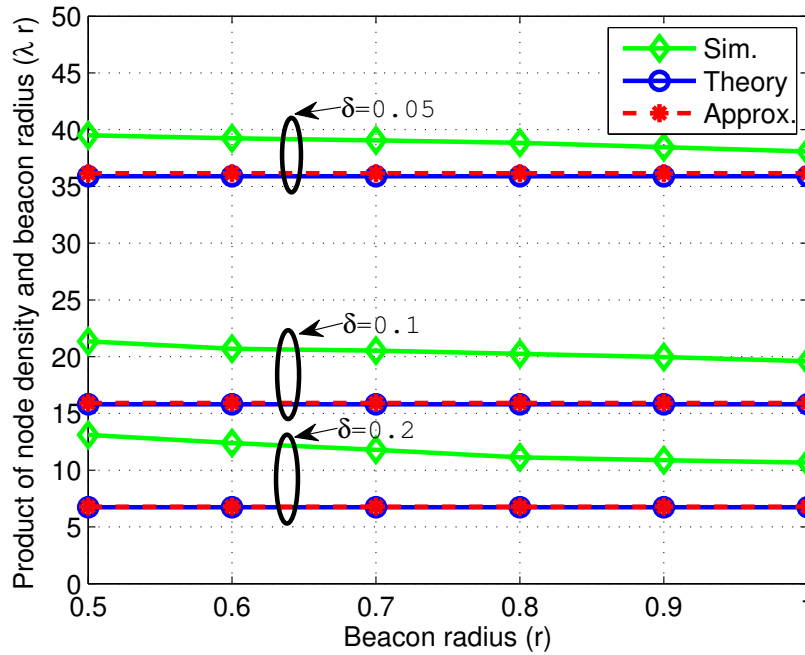


Figure 4.5: Product of the node density and beacon radius required to localize the target within a grid cell with probability 0.9 vs beacon radius for various dimensions of grid cell, when the target node employs single power threshold.

the proportion of number of beacon nodes intersecting twice reduces as compared to nodes intersecting once, making the analysis more accurate. The λr product obtained by theoretical expression (4.11) and its approximation (4.19) captures the behavior well, although there is a gap between the theoretical and experimental results.

Figure 4.6 validates the derived minimal beacon density required for various grid cell dimensions, when multiple power threshold intervals are considered at the target. As discussed above, for single threshold case, the optimal beacon density recommended by theory is slightly less than the experimental value. Although, similar to single threshold scenario, the power contours of a subset of the beacon nodes make dependent intersections on the line segment \mathcal{S} , the possibility of exploiting multiple thresholds leads to a different behavior in optimal beacon density required. Because

of the planned choice of annulus width equal to grid cell size, the number of nodes required to localize the target within a grid cell is slightly less than as prescribed by theory, making it a conservative design. As the grid cell size increases, the proposed design procedure matches well with the simulation as the proportion of planned intersections on S reduces.

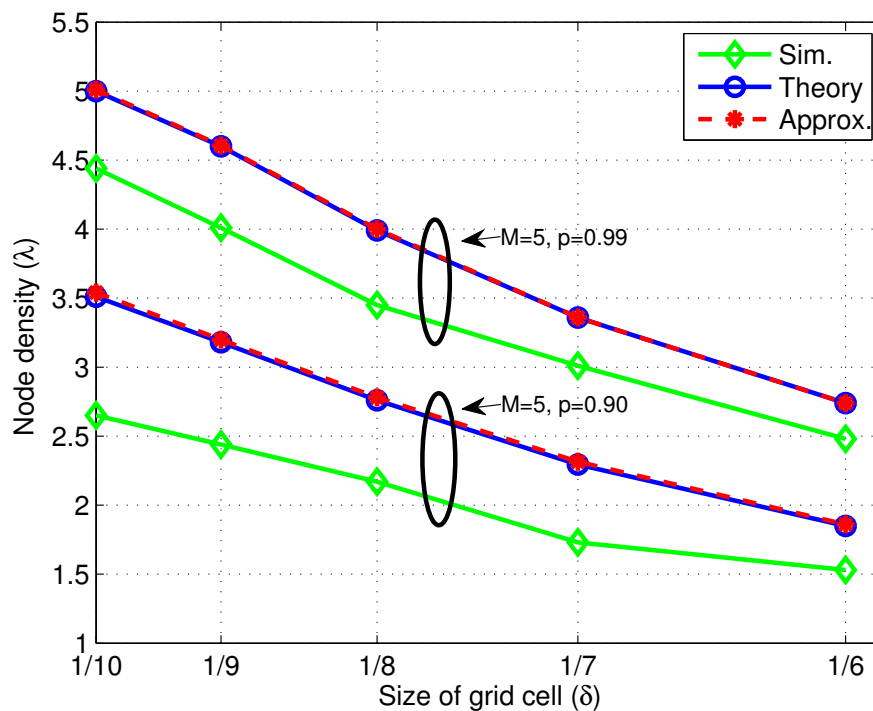


Figure 4.6: Node density required to localize the target within a grid cell with probability p vs the grid cell size, when the beacon node employs $M = 5$ threshold intervals. The average beacon radius \bar{r} is 0.9 and the annulus width is equal to grid cell size δ .

In Fig. 4.7, the probability of localizing the target within a grid cell is plotted for product of node density and number of threshold levels (λM). For $M = 1$, the average probability achieved is slightly less than the theoretical value because of the dependent intersections of the power contours intersecting twice on S . Whereas, for $M = 2$ and 5, where the intersections on S are structured due to the annuli width being set equal to

the size of the grid cell, the average probability attained is higher than the theoretical value. Thus, for the multiple threshold scenario, the proposed design procedure is a conservative design. Also, as described earlier, the average probability approaches 1 nearly in an exponential manner as node density increases as it is approximately given by $1 - (4\lambda\bar{r}M)e^{-\delta(4\lambda\bar{r}M)}$.

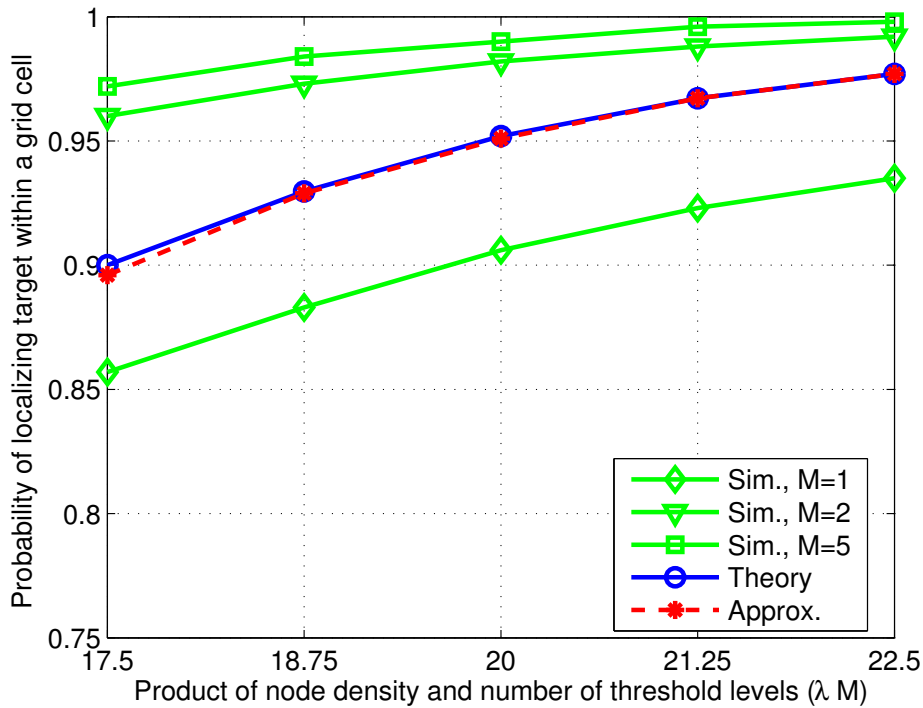


Figure 4.7: Probability of localizing the target within a grid cell vs product of the node density and number of threshold intervals. The average beacon radius \bar{r} is 0.9, the grid cell size δ is 0.1 and the annulus width is equal to grid cell size δ .

The MSE in localization vs number of beacon nodes for various values of threshold intervals (M) is shown in Fig. 4.8. The MSE is indirectly related to the average probability that the largest spacing between the intersections is less than the grid cell size (eqn. (4.19)). Thus, the MSE for the proposed approach decreases as $e^{-\delta\mu}$ as the node density increases. In Fig. 4.8, the decrease in MSE is nearly linear on the logarithmic scale, as

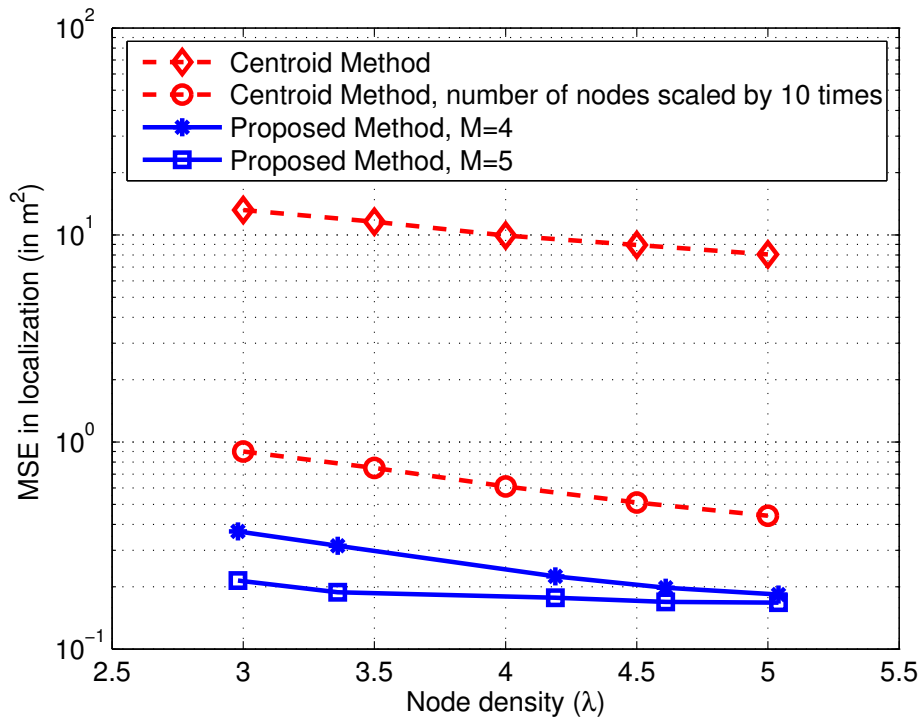


Figure 4.8: MSE in localization vs number of beacon nodes for different power levels on a 10×10 grid, with each grid cell of area 1 m^2 . The dimensions of area of interest \mathcal{A} is $10\text{m} \times 10\text{m}$. For the proposed method, the average beacon radius is 9m and the annulus width is 1m .

exponential term is dominant. Also, the MSE decreases as the number of power thresholds M increases, since $\mu = 4\lambda\bar{r}M$. It is clear that the proposed method outperforms the centroid based method [101], even when the number nodes in the area of interest is scaled by 10 times.

Table 4.1 lists the localization accuracy achieved for various combinations of number of beacon nodes (K) and number of threshold intervals at target (M). For a given grid size, roughly the same number of tests ($T = KM$) are required to identify the target location to the accuracy of one grid cell with probability at least 90%. This illustrates that the beacon node density can be exchanged with the number of threshold intervals to achieve the same performance. Note that, in this case, the node density can be further

reduced by increasing the average beacon radius and the annulus width.

Table 4.1: Localization accuracy to within 1, 2, or 3 or more grid cells for various combinations of number of beacon nodes, K , and number of power levels per beacon node, M . The average beacon radius is 0.27 and the annulus width is 0.07.

Grid Size	K	M	T	Localization Accuracy (in %)		
				1 grid cell	2 grid cells	3 or more grid cells
10×10	19	5	95	90.5	6.1	3.4
	24	4	96	90.4	6.7	2.9
	35	3	105	90.5	6.7	2.8
20×20	27	5	135	91.2	4.9	3.9
	36	4	144	90.9	5.0	4.1
	52	3	156	89.9	6.3	3.8

4.4.2 Experimental Results

The proposed scheme is also evaluated with experimental data collected in an indoor environment. As shown in Fig. 4.9, a room of size $5\text{m} \times 3\text{m}$ is divided into 15 grid cells, each of dimension $1\text{m} \times 1\text{m}$. Four different setups of 4, 5, 6 and 7 beacon nodes are considered, with beacons placed along the perimeter of the room. The beacon nodes transmit their ids on the bluetooth low energy (BLE) 2.4 GHz band at a power of $P_0 = -23$ dBm. A commercial off-the-shelf (COTS) mobile phone with BLE capability is used as the target node. At each grid location, multiple number of RSS measurements are made per beacon node. Later, 60% of the measured data is used as training data and the rest of the available data is used as the test data. At any grid cell, the RSS measurements from a given beacon node are averaged and compared with predetermined threshold intervals to build the binary test matrix \mathbf{A} . The MSE performance with experimental data is plotted in Fig. 4.10. The plot reaffirms that using multiple threshold

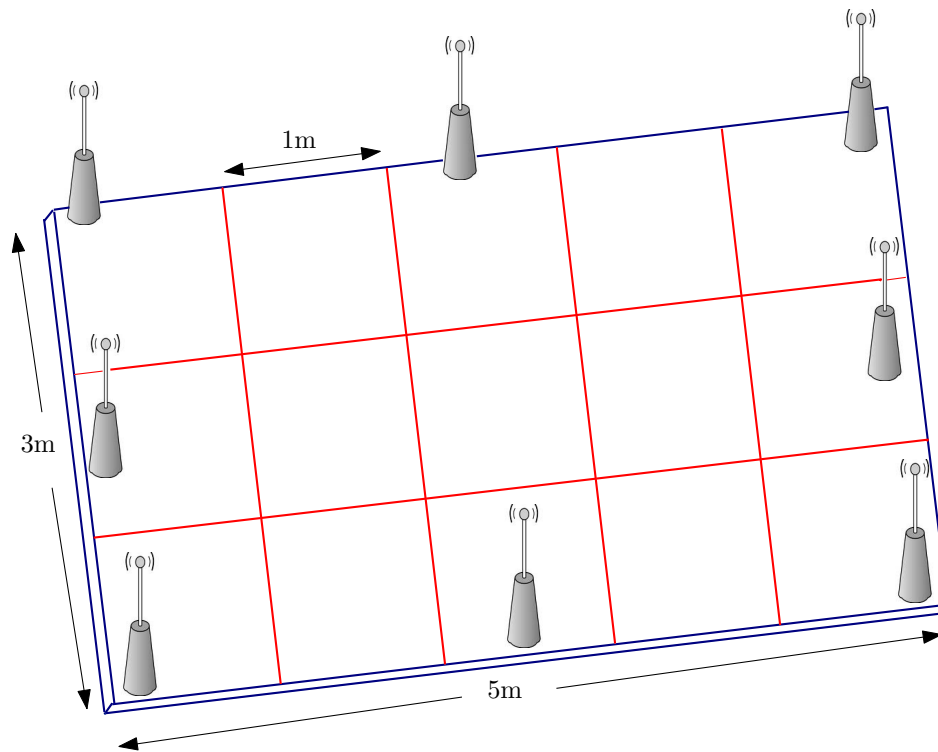


Figure 4.9: Depiction of the experimental setup, with beacon nodes placed along the boundary of the room.

intervals improves the performance. It can be observed that using two threshold intervals instead of one decreases the MSE in localization by 0.7m^2 .

4.5 Conclusion

This work considered target localization with the help of beacon nodes. The target node localizes itself by comparing the received power from these beacon nodes with a set of predetermined threshold intervals. The problem of localization was cast as the one where the cells were tested for the presence of the target. The column matching algorithm from group testing was used to localize the target. The average probability of localizing the target within a grid cell was derived. This was used to determine the

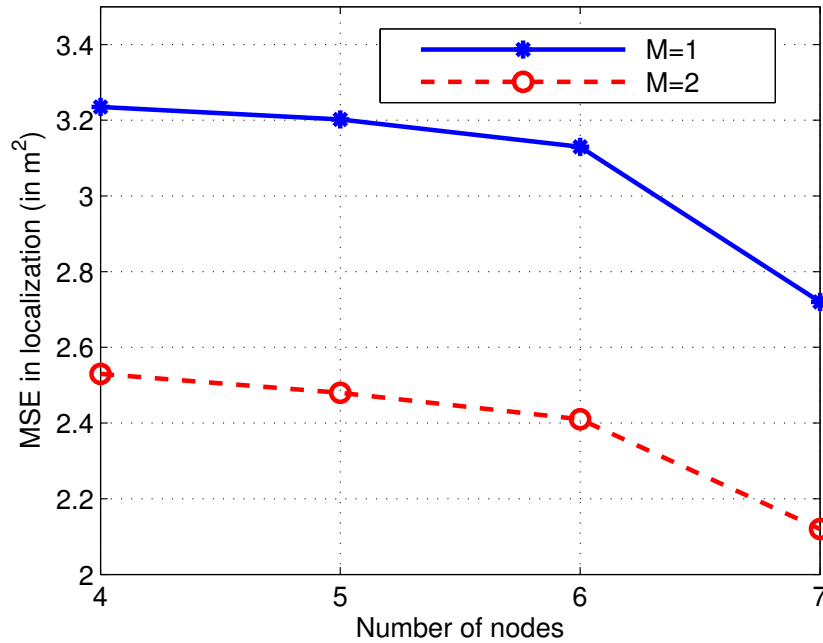


Figure 4.10: MSE in localization vs number of beacon nodes for experimental setup.

required optimal node density to localize the target within a grid cell with high probability. For the multiple threshold scenario, the minimum node density recommended by the proposed design procedure based on upper bounding the probability of failing to localize the target to a single grid cell was found to be slightly higher than the experimental value, thus, making it a conservative design. It was shown that the average probability of localizing the target within a grid cell approaches 1 exponentially with increase in node density, beacon radius or the number of threshold intervals. Empirically, it was shown that, for a 10×10 grid, the proposed approach with 5 threshold intervals has almost two orders of magnitude better MSE performance compared to the centroid-based method. Also, the proposed method of using multiple power thresholds was validated with experimental data collected using BLE nodes as beacons and a

COTS mobile as a target. The experimental results demonstrated the efficacy of the proposed approach in target localization to a desired accuracy level. Only a small number of beacon nodes need to be deployed and very small (binary) computational resources are required at the mobile phone (target) to estimate its location.

Chapter 5

Conclusion

This thesis presented physical layer algorithms based on binary data fusion for three applications in the context of cognitive radios. First, in the context of cooperative spectrum sensing, the problem of achieving majority consensus by exchanging binary messages between nodes over fading wireless channels was addressed. Next, the task of creating spatial spectrum occupancy maps was accomplished by treating it as the problem of localizing and identifying communication footprints of primary transmitters. Finally, a column matching based algorithm was proposed for self-localization of a target (white space device). The performance of the proposed solutions was analyzed with the help of appropriate stochastic tools.

The problem of physical layer binary consensus was considered in chapter 2. Here, a set of nodes are required to come to agreement on the majority of their initial binary decisions (bits) by exchanging and updating their bits over the fading wireless channels. The nodes broadcast their bits in round-robin manner, and at the end of the cycle each node updates its bit by using a sum of votes estimate. A simple co-phased combining scheme, where the sum of votes is the sum of phase-shifted received samples, was

proposed, and compared and contrasted with an LMMSE based scheme. The LMMSE based scheme considers a weighted linear combination of co-phased received samples as the sum of votes estimate, with weights obtained by solving an LMMSE problem of estimating the sum of votes. The LMMSE weights depend on the knowledge of channel magnitudes in addition to their phases, and are not optimal under channel estimation errors.

As in the literature on consensus problems, the evolution of the network consensus was modeled as a first order Markov chain (MC). For the co-phased combining scheme, the average transition probability matrix (TPM) of the MC was derived using the average probability of detecting bit '1' conditioned on the number of nodes voting '1', whereas, this quantity was not tractable for the LMMSE based scheme. To derive the average probability of detecting bit '1', the sum of weighted Rayleigh random variables (r.v.) was approximated by a Nakagami r.v., and then, the probability density function (pdf) for the difference of two Nakagami r.v.s was derived. Later, this pdf was used to obtain the average probability of detecting bit '1'.

The MC for these two schemes was shown to be, irreducible and aperiodic, implying that there are no absorbing states. Therefore, expressions for quantities such as average consensus duration and average hitting time were derived. These quantities are important for determining the stopping time for the consensus procedure. Along with these quantities, the second largest eigen value of the TPM and the probability of accurate consensus were used as performance metrics.

It was found that the computationally inexpensive co-phased combining scheme outperforms the LMMSE based scheme at low-to-moderate SNRs, besides being mathematically tractable. It was also shown that optimizing the power between data and pilot symbols gives significant performance gains. Allocation of transmit powers across the consensus cycles based on the knowledge of the link qualities is a subject for future study.

In chapter 3, two novel schemes for fast multiple transmitter localization and communication footprint estimation were proposed. The schemes were based on multiple simultaneous 1-bit transmissions from sensors to the FC using pseudo-random phase shifts, followed by compressive sensing (CS) based recovery of the alarming sensor locations. Then, the alarming sensor locations were clustered using the K -means algorithm, and a novel circular fitting technique was used to determine the number of primary transmitters. This was followed by transmitter localization using trilateration or circular regression methods to finally obtain the estimates of the number of primary transmitters, their locations and communication footprints.

It was seen that the proposed schemes require fewer number of transmissions and lower transmit power to reconstruct the map at a given fidelity. Of the proposed schemes, *Scheme 2*, which was based on the sensors on the boundary of the footprint being the alarming sensors, was the best performing scheme in terms of the average relative error in transmitter footprint identification. Two popular sparse recovery algorithms, the OMP and ℓ_1 minimization based recovery were compared, and it was found that at higher SNRs, the OMP performs better than ℓ_1 in terms of the percentage of successful recovery. The efficacy of the proposed schemes were illustrated using

Monte-Carlo simulations and real-world measurements in a simple experimental setup.

Chapter 4 considered the problem of target self-localization with the help of beacon nodes. The target node localizes itself by comparing the received power from these beacon nodes with a set of predetermined threshold intervals. The problem of localization was cast as the one where the cells were tested for the presence of the target. The advantage of putting the problem in this framework is that it then becomes one of group testing, where, in each test, subsets of individuals (grid locations) are tested for the presence of defective individuals (targets). This, in turn, allowed us to draw on the vast literature on group testing for devising target localization algorithms. To illustrate this, the column matching algorithm from group testing was used to localize the target.

The average probability of localizing the target within a grid cell was derived by using the tools from Poisson point processes and order statistics. This was used to determine the minimum required node density to localize the target within a grid cell with high probability. The proposed design procedure was found to be a conservative design for the multiple threshold scenario, that is, to achieve the desired localization accuracy, the minimal beacon density recommended is slightly higher than the experimental value. This is because of the planned choice of the width of the annuli based on the size of the grid cell.

It was shown that the average probability of localizing the target within a grid cell approaches 1 exponentially with node density, beacon radius or the number of threshold intervals. Empirically, it was shown that the proposed method significantly outperforms the baseline of centroid based localization. Further, the method naturally allows for sensing errors or noise, by using the algorithms from noisy group testing. Also,

the proposed method of using multiple power thresholds was validated with experimental data collected using BLE nodes as beacons and a COTS mobile as a target. The experimental results successfully demonstrated the efficacy of the proposed approach in target localization to a desired accuracy level.

Appendix A

A.1 Proof of Lemma 1

Note that, $\mathbb{E}[H_p^2] = \mathbb{E}[(\sum_{s_k \in \mathcal{K}} |H_{kl}| \cos \tilde{\theta}_{kl})^2]$ has i.i.d. summand terms. Hence, it can be expressed as

$$\mathbb{E}[H_p^2] = K\mathbb{E}[G_{kl}^2] + K(K-1)(\mathbb{E}[G_{kl}])^2. \quad (\text{A.1})$$

In [67], the first and second moments of G_{kl} are evaluated as

$$\mathbb{E}[G_{kl}] = \sqrt{\frac{\pi\sigma^2}{4}} \sqrt{\frac{\gamma_p\sigma^2}{1+\gamma_p\sigma^2}}, \quad \mathbb{E}[G_{kl}^2] = \frac{\sigma^2(1+2\gamma_p\sigma^2)}{2+2\gamma_p\sigma^2}. \quad (\text{A.2})$$

Substituting the above expressions in (A.1) leads to (2.10).

Next, the variance of H_p^2 is given by

$$\text{Var}[H_p^2] = \mathbb{E}[H_p^4] - (\mathbb{E}[H_p^2])^2. \quad (\text{A.3})$$

As the terms G_{kl} are i.i.d., we have

$$\begin{aligned}
\mathbb{E}[H_p^4] &= K\mathbb{E}[G_{kl}^4] + 3K(K-1)(\mathbb{E}[G_{kl}^2])^2 \\
&\quad + K(K-1)(K-2)(K-3)(\mathbb{E}[G_{kl}])^4 \\
&\quad + 6K(K-1)(K-2)(\mathbb{E}[G_{kl}])^2\mathbb{E}[G_{kl}^2] \\
&\quad + 4K(K-1)\mathbb{E}[G_{kl}^3]\mathbb{E}[G_{kl}].
\end{aligned} \tag{A.4}$$

The third and fourth moment of G_{kl} ,

$$\mathbb{E}[G_{kl}^3] = \frac{3\sigma^4\sqrt{\gamma_p\pi}}{4\sqrt{1+\gamma_p\sigma^2}}, \text{ and} \tag{A.5}$$

$$\mathbb{E}[G_{kl}^4] = 2\sigma^4 - \frac{\sigma^4}{4} \frac{5+4\gamma_p\sigma^2}{(1+\gamma_p\sigma^2)^2} \tag{A.6}$$

are derived in [110, 111]. The expressions in (A.5), (A.6) along with (A.2) and (2.10) are used to obtain the expression for $Var[H_p^2]$.

A.2 The Probability Density Function of the Difference of Two Nakagami Random Variables

The pdf of the difference of two independent Nakagami r.v.s is

$$f_H(h) = \int_0^\infty f_{H_p}(h+h_n) f_{H_n}(h_n) dh_n, \text{ for } h \geq 0. \tag{A.7}$$

Substituting for the pdf of Nakagami r.v.s and then by completing the squares, (A.7) can be expressed as

$$f_H(h) = \frac{4 \left(\frac{m_1}{\Omega_1}\right)^{m_1} \left(\frac{m_2}{\Omega_2}\right)^{m_2} e^{-\frac{h^2 m_1 m_2}{m}}}{\Gamma(m_1)\Gamma(m_2)} \int_0^\infty (h + h_n)^{2m_1-1} (h_n)^{2m_2-1} e^{-\frac{m}{\Omega} \left(h_n + \frac{m_1 \Omega_2 h}{m}\right)^2} dh_n, \quad (\text{A.8})$$

where $m \triangleq m_1 \Omega_2 + m_2 \Omega_1$ and $\Omega \triangleq \Omega_1 \Omega_2$. By changing the variable of integration to $u \triangleq \sqrt{\frac{m}{\Omega}} \left(h_n + \frac{m_1 \Omega_2 h}{m}\right)$, (A.8) is expressed as

$$f_H(h) = \frac{4 \left(\frac{m_1}{\Omega_1}\right)^{m_1} \left(\frac{m_2}{\Omega_2}\right)^{m_2} e^{-\frac{h^2 m_1 m_2}{m}}}{\Gamma(m_1)\Gamma(m_2) \left(\frac{m}{\Omega}\right)^{m_1+m_2-\frac{1}{2}}} \int_{\frac{m_1 \Omega_2 h}{\sqrt{m\Omega}}}^\infty \left(u + \frac{m_2 \Omega_1 h}{\sqrt{m\Omega}}\right)^{2m_1-1} \left(u - \frac{m_1 \Omega_2 h}{\sqrt{m\Omega}}\right)^{2m_2-1} e^{-u^2} du. \quad (\text{A.9})$$

The parameters $2m_1$ and $2m_2$ are rounded-off to their corresponding nearest integers. Then, using the binomial expansion for power terms, the pdf of the effective channel can be simplified as

$$f_H(h) = \frac{2 \left(\frac{m_1}{\Omega_1}\right)^{m_1} \left(\frac{m_2}{\Omega_2}\right)^{m_2} e^{-\frac{h^2 m_1 m_2}{m}}}{\Gamma(m_1)\Gamma(m_2) \left(\frac{m}{\Omega}\right)^{m_1+m_2-\frac{1}{2}}} \sum_{i=0}^{2m_1-1} \sum_{j=0}^{2m_2-1} \binom{2m_1-1}{i} \binom{2m_2-1}{j} \left(\frac{m_2 \Omega_1 h}{\sqrt{m\Omega}}\right)^{2m_1-1-i} \left(\frac{-m_1 \Omega_2 h}{\sqrt{m\Omega}}\right)^{2m_2-1-j} \Gamma\left(\frac{i+j+1}{2}, \frac{(m_1 \Omega_2 h)^2}{m\Omega}\right), \text{ for } h \geq 0, \quad (\text{A.10})$$

where $\Gamma(\cdot, \cdot)$ is the upper incomplete gamma function. For $h < 0$, $f_H(h)$ can be evaluated by swapping the parameters m_1, Ω_1 with m_2, Ω_2 , respectively.

A.3 Derivation of \bar{p}_l for the Co-phased Combining Scheme

The \bar{p}_l in (2.9) can be expressed as

$$\bar{p}_l = \int_{-\infty}^{\infty} \int_{-\frac{h\sqrt{E_d}}{\sigma_v}}^{\infty} \frac{1}{\sqrt{2\pi}} e^{-v^2/2} f_H(h) dv dh. \quad (\text{A.11})$$

By setting the variable of integration as $x \triangleq v\sigma_v/h\sqrt{E_d}$ and changing the order of integration, (A.11) can be expressed as

$$\bar{p}_l = \frac{\sqrt{E_d}}{\sqrt{2\pi}\sigma_v} \int_{-1}^{\infty} \underbrace{\int_{-\infty}^{\infty} h e^{-h^2 x^2 E_d / 2\sigma_v^2} f_H(h) dh}_{\triangleq I_1} dx. \quad (\text{A.12})$$

By substituting (A.8) for $f_H(h)$, $h \geq 0$, and then using (6.455) from [112], the integral I_1 between the limits 0 and ∞ can be evaluated as

$$\frac{2 \left(\frac{m_1}{\Omega_1}\right)^{m_1} \left(\frac{m_2}{\Omega_2}\right)^{m_2} \left(\frac{\Omega}{m}\right)^{m_1+m_2-\frac{1}{2}}}{\Gamma(m_1)\Gamma(m_2)} \sum_{i=0}^{2m_1-1} \sum_{j=0}^{2m_2-1} \binom{2m_1-1}{i} \binom{2m_2-1}{j} \left(\frac{m_2\Omega_1}{\sqrt{m\Omega}}\right)^{2m_1-1-i} (-1)^{2m_2-1-j} \\ \frac{\left(\frac{m_1\Omega_2}{\sqrt{m\Omega}}\right)^{2m_2-i} \Gamma(m_1 + m_2 + \frac{1}{2}) {}_2F_1\left(1, m_1 + m_2 + \frac{1}{2}; m_1 + m_2 - \frac{i+j-2}{2}; \frac{x^2\gamma_d + \frac{m_1 m_2}{m}}{\frac{x^2\gamma_d}{2} + \frac{m_1}{\Omega_1}}\right)}{(2m_1 + 2m_2 - i - j) \left(\frac{x^2\gamma_d}{2} + \frac{m_1}{\Omega_1}\right)^{m_1+m_2+\frac{1}{2}}}, \quad (\text{A.13})$$

where ${}_2F_1$ is the Gauss hypergeometric function and $\gamma_d = E_d/\sigma_v^2$. Following the similar procedure, I_1 can be evaluated between the limits $-\infty$ and 0. The two expressions can now be substituted in (A.12) to evaluate \bar{p}_l .

A.4 Second Largest Eigenvalue of the Average TPM for $N = 3$ Sensors

It can be shown that the second largest eigenvalue of the average TPM is $1 - 2\bar{p}^{(1)}$ when $N = 3$ sensors are involved in achieving consensus. Let, p_0, p_1 and p_2 denote the probability of detecting bit '1' at a sensor when two other sensors transmit bits '(0, 0)', '(0, 1)', and '(1, 1)', respectively. Then, by combining equivalent states (for e.g., state '001' is equivalent to '100' and '010'), the average TPM is given by

$$\bar{\mathbf{P}} = \begin{bmatrix} p_2^3 & 3p_0p_2^2 & 3p_0^2p_2 & p_0^3 \\ p_1^2p_2 & p_1^2p_0 + 2p_1^2p_2 & p_1^2p_2 + 2p_1^2p_0 & p_1^2p_0 \\ p_1^2p_0 & p_1^2p_2 + 2p_1^2p_0 & p_1^2p_0 + 2p_1^2p_2 & p_1^2p_2 \\ p_0^3 & 3p_0^2p_2 & 3p_0p_2^2 & p_2^3 \end{bmatrix}. \quad (\text{A.14})$$

The average TPM, $\bar{\mathbf{P}}$ is a centro-symmetric matrix [113], i.e.,

$$\bar{\mathbf{P}} = \begin{bmatrix} A & B \\ JBJ & JAJ \end{bmatrix}, \quad (\text{A.15})$$

where J is a counter-identity matrix, and

$$A = \begin{bmatrix} p_2^3 & 3p_0p_2^2 \\ p_1^2p_2 & p_1^2p_0 + 2p_1^2p_2 \end{bmatrix}, \text{ and } B = \begin{bmatrix} 3p_0^2p_2 & p_0^3 \\ p_1^2p_2 + 2p_1^2p_0 & p_1^2p_0 \end{bmatrix}. \quad (\text{A.16})$$

For such an average TPM, it is known that $\bar{\mathbf{P}}$ is similar to

$$C = \begin{bmatrix} A - BJ & 0 \\ 0 & A + BJ \end{bmatrix}. \quad (\text{A.17})$$

Thus, the eigenvalues of $\bar{\mathbf{P}}$ are same as that of $A - BJ$ and $A + BJ$. The eigenvalues of $A - BJ$ are found to be 1 and $\frac{3}{4} - 3p_0p_2$ and eigenvalues of $A + BJ$ are $1 - 2p_0$ and

$(1-2p_0)(\frac{1}{4}-p_0p_2)$. The second largest eigenvalue is $1-2p_0$, which is the same as $1-2\bar{p}^{(1)}$.

A.5 Derivation of $\bar{p}^{(M)}$ and $\bar{p}^{(1)}$ for the Co-phased Combining Scheme

When the bits b_1 to b_N are $+1$, $|\mathcal{K}| \triangleq |\mathcal{S} \setminus \{s_l\}| = N - 1$ and the effective channel H can be approximated by a Nakagami r.v. with parameters m_1 and Ω_1 . So, the average probability $\bar{p}^{(M)}$ in (2.9) can be expressed as

$$\bar{p}^{(M)} = \int_0^\infty \int_{-\frac{h\sqrt{E_d}}{\sigma_v}}^\infty \frac{1}{\sqrt{2\pi}} e^{-v^2/2} \frac{2}{\Gamma(m_1)} \left(\frac{m_1}{\Omega_1}\right)^{m_1} h^{2m_1-1} e^{-m_1 h^2/\Omega} dv dh. \quad (\text{A.18})$$

By setting the variable of integration as $x \triangleq v\sigma_v/h\sqrt{E_d}$ and changing the order of integration, (A.18) can be expressed as

$$\bar{p}^{(M)} = \sqrt{\frac{2\gamma_d}{\pi}} \frac{1}{\Gamma(m_1)} \left(\frac{m_1}{\Omega_1}\right)^{m_1} \int_{-1}^\infty \underbrace{\int_0^\infty h^{2m_1} e^{-h^2(\frac{x^2\gamma_d}{2} + \frac{m_1}{\Omega_1})} dh}_{\triangleq I_2} dx. \quad (\text{A.19})$$

The integral I_2 can be solved using (3.326) from [112] and substituted in (A.19) to obtain

$$\bar{p}^{(M)} = \sqrt{\frac{\gamma_d}{2\pi}} \frac{1}{\Gamma(m_1)} \left(\frac{m_1}{\Omega_1}\right)^{m_1} \int_{-1}^\infty \frac{\Gamma(m_1 + 0.5)}{\left(\frac{x^2\gamma_d}{2} + \frac{m_1}{\Omega_1}\right)^{m_1+0.5}} dx. \quad (\text{A.20})$$

Further, the integral in (A.20) can be expressed as

$$\bar{p}^{(M)} = \sqrt{\frac{\gamma_d}{2\pi}} \frac{\Gamma(m_1 + 0.5)}{\Gamma(m_1)} \left(\frac{m_1}{\Omega_1}\right)^{m_1} \left[\frac{x}{(m_1/\Omega_1)^{m_1+0.5}} {}_2F_1 \left(0.5, m_1 + 0.5; 1.5; -\frac{\gamma_d x^2}{2m_1/\Omega_1} \right) \right]_{-1}^\infty. \quad (\text{A.21})$$

This leads to

$$\bar{p}^{(M)} = 0.5 + \sqrt{\frac{\gamma_d}{2\pi}} \frac{\Gamma(m_1 + 0.5)}{\Gamma(m_1) \sqrt{m_1/\Omega_1}} {}_2F_1 \left(0.5, m_1 + 0.5; 1.5; -\frac{\gamma_d}{2m_1/\Omega_1} \right). \quad (\text{A.22})$$

When the bits b_1 to b_N are 0, $|\mathcal{K}^c| \triangleq |\mathcal{S} \setminus \{\mathcal{K}, s_l\}| = N - 1$ and the effective channel H can be approximated by the negative of a Nakagami r.v. with parameters m_2 and Ω_2 .

The average probability $\bar{p}^{(1)}$ is given by

$$\bar{p}^{(1)} = 1 - \bar{p}^{(M)}. \quad (\text{A.23})$$

Therefore, replacing the parameters m_1 and Ω_1 by m_2 and Ω_2 , respectively, $\bar{p}^{(1)}$ can be expressed as

$$\bar{p}^{(1)} = 0.5 - \sqrt{\frac{\gamma_d}{2\pi}} \frac{\Gamma(m_2 + 0.5)}{\Gamma(m_2) \sqrt{m_2/\Omega_2}} {}_2F_1 \left(0.5, m_2 + 0.5; 1.5; -\frac{\gamma_d}{2m_2/\Omega_2} \right). \quad (\text{A.24})$$

A.6 Proof that the Average Probability \bar{P}_{ij} is Strictly Positive

The probability that the system changes from $\phi^{(j)}$ to $\phi^{(i)}$ at an arbitrary time t is given by

$$\bar{P}_{ij} = \prod_{l=1}^N \left[b_l^{(i)} \bar{p}_l^{(j)} + (1 - b_l^{(i)}) (1 - \bar{p}_l^{(j)}) \right], \quad (\text{A.25})$$

i.e., it is the product of the N probability terms. We will consider the least of these probabilities, the probability that a node s_l detects bit ‘1’ in the current cycle when all other nodes have bit ‘0’ in the previous cycle. This probability, $\bar{p}^{(1)}$, is derived in (A.24), and it can be verified that, the second term of (A.24) is strictly smaller than 0.5. Thus,

the least of the probabilities, $\bar{p}^{(1)}$ is strictly greater than zero, and therefore, $\bar{P}_{ij} > 0$.

Appendix B

B.1 Approximate Mean Square Error in Localization

Consider a rectangular region of area A on which L sensors are deployed uniformly at random locations (X_i, Y_i) , and a transmitter is located at a random location (X_s, Y_s) . For a given sensing threshold, let the random variable m denote the number of sensors within a radius of d around (X_s, Y_s) . Then, the location of the transmitter is estimated as $(\sum_{i=1}^m X_i/m, \sum_{i=1}^m Y_i/m)$. For simplicity, the edge effects of the circular area around the transmitter falling outside the area A is neglected in this analysis, which is valid when A is large compared to d^2 . The MSE in localization is

$$MSE = \mathbb{E}_m \left\{ \frac{1}{m^2} \mathbb{E}_{X_i, Y_i} \left\{ \sum_{i=1}^m (X_s - X_i)^2 + \sum_{i=1}^m (Y_s - Y_i)^2 \right\} \right\}. \quad (\text{B.1})$$

If r and θ are the polar representation of $(X_s - X_i, Y_s - Y_i)$, defined such that $X_s - X_i = r \cos \theta$, $Y_s - Y_i = r \sin \theta$, then θ is uniformly distributed in $(0, 2\pi)$ and r is distributed such that $r = \sqrt{z}d$ where z is uniformly distributed on $[0, 1]$. Hence, r has probability density function $f(r) = 2r/d^2$ for $r \in [0, d]$ and zero elsewhere. Thus, the MSE becomes

$$MSE = \mathbb{E}_m \left\{ \frac{1}{m^2} \mathbb{E}_r \{mr^2\} \right\} = \mathbb{E}_m \left\{ \frac{1}{m} \right\} \frac{d^2}{2}. \quad (\text{B.2})$$

Note that the above expectation is taken over all $m > 0$. Clearly, m is binomial distributed, with parameters $p \triangleq \pi d^2/A$ and L . Unfortunately, evaluating the expectation of $1/m$ for large L in closed form is hard, but a good approximation is obtained by using the simple lower bound: $\mathbb{E}_m \{1/m\} \geq 1/\mathbb{E}_m \{m\}$. Now, since $\mathbb{E}_m \{m\} = L\pi d^2/A$, one obtains

$$MSE \approx \frac{A}{2\pi L}. \quad (\text{B.3})$$

Bibliography

- [1] Ofcom, "Spectrum management strategy," Ofcom, Tech. Rep., Oct. 2013. [Online]. Available: http://stakeholders.ofcom.org.uk/binaries/consultations/spectrum-management-strategy/summary/spectrum_management_strategy.pdf
- [2] FCC Spectrum Policy Task Force, "Report of the spectrum efficiency working group," FCC, Tech. Rep., Nov. 2002. [Online]. Available: <http://www.fcc.gov/sptf/reports.html>
- [3] Q. Zhao and B. M. Sadler, "A survey of dynamic spectrum access," *IEEE Signal Processing Mag.*, vol. 24, no. 3, pp. 79–89, May 2007.
- [4] J. Mitola and G. Q. Maguire Jr, "Cognitive radio: making software radios more personal," *IEEE Pers. Commun.*, vol. 6, no. 4, pp. 13–18, Aug. 1999.
- [5] J. Mitola, "Cognitive radio, licentiate proposal," Ph.D. dissertation, Royal Institute of Technology, Stockholm, Sweden, Aug. 1999.
- [6] —, "Cognitive radio for flexible mobile multimedia communications," in *Proc. IEEE Int. Workshop. Mob. Multimedia Commun.*, Nov. 1999, pp. 3–10.

- [7] K. S. Gilhousen, I. M. Jacobs, R. Padovani, A. J. Viterbi, J. LA Weaver, and C. E. Wheatley III, "On the capacity of a cellular cdma system," *IEEE Trans. Veh. Technol.*, vol. 40, no. 2, pp. 303–312, May 1991.
- [8] M. Z. Win and R. A. Scholtz, "Impulse radio: How it works," *IEEE Commun. Lett.*, vol. 2, no. 2, pp. 36–38, Feb. 1998.
- [9] R. Menon, R. M. Buehrer, and J. H. Reed, "Outage probability based comparison of underlay and overlay spectrum sharing techniques," in *Proc. IEEE Int. Symp. on Dynamic Spectrum Access Netw.*, Nov. 2005, pp. 101–109.
- [10] L. Piazzo and J. Romme, "Spectrum control by means of the TH code in UWB systems," in *Proc. IEEE Veh. Technol. Conf. (Spring)*, vol. 3, Apr. 2003, pp. 1649–1653.
- [11] J. Wang, "Narrowband interference suppression in time hopping impulse radio," in *Proc. IEEE Veh. Technol. Conf. (Fall)*, vol. 3, Sep. 2004, pp. 2138–2142.
- [12] C. Rose, S. Ulukus, and R. D. Yates, "Wireless systems and interference avoidance," *IEEE Trans. Wireless Commun.*, vol. 1, no. 3, pp. 415–428, July 2002.
- [13] J. Ibrahim, R. Menon, and R. M. Buehrer, "UWB sequence optimization for enhanced energy capture and interference mitigation," in *Proc. IEEE Military Commun. Conf.*, Oct. 2005, pp. 2086–2092.
- [14] S. M. Kay, *Fundamentals of Statistical Signal Processing: Detection Theory*, vol. 2. Prentice Hall Upper Saddle River, NJ, USA:, 1998.

- [15] "IEEE 802.22 standard." [Online]. Available: <http://standards.ieee.org/about/get/802/802.22.html>
- [16] D. Cabric, S. M. Mishra, and R. W. Brodersen, "Implementation issues in spectrum sensing for cognitive radios," in *Proc. Asilomar Conf. on Signals, Syst., and Comput.*, vol. 1, Nov. 2004, pp. 772–776.
- [17] S. Haykin, D. J. Thomson, and J. H. Reed, "Spectrum sensing for cognitive radio," *Proceedings of the IEEE*, vol. 97, no. 5, pp. 849–877, May 2009.
- [18] D. Bhargavi and C. R. Murthy, in *Proc. Int. Workshop Signal Process. Advances in Wireless Commun.*, June 2010, pp. 1–5.
- [19] E. Axell, G. Leus, E. G. Larsson, and H. V. Poor, "State-of the art and recent advances, spectrum sensing for cognitive radio," *IEEE Signal Processing Mag.*, vol. 29, no. 3, pp. 101–106, May 2012.
- [20] H. Urkowitz, "Energy detection of unknown deterministic signals," *Proceedings of the IEEE*, vol. 55, no. 4, pp. 523–531, Apr. 1967.
- [21] F. F. Digham, M.-S. Alouini, and M. K. Simon, "On the energy detection of unknown signals over fading channels," *IEEE Trans. Commun.*, vol. 55, no. 1, pp. 21–24, Jan. 2007.
- [22] N. Hoven, R. Tandra, and A. Sahai, "Some fundamental limits on cognitive radio," *Wireless Foundations EECS, Univ. of California, Berkeley*, 2005.
- [23] E. Axell and E. G. Larsson, "Optimal and sub-optimal spectrum sensing of OFDM

- signals in known and unknown noise variance," *IEEE J. Select. Areas Commun.*, vol. 29, no. 2, pp. 290–304, Feb. 2011.
- [24] R. Tandra and A. Sahai, "SNR walls for signal detection," *IEEE J. Sel. Topics Signal Process.*, vol. 2, no. 1, pp. 4–17, Feb. 2008.
- [25] S. Chaudhari, V. Koivunen, and H. V. Poor, "Autocorrelation-based decentralized sequential detection of OFDM signals in cognitive radios," *IEEE Trans. Signal Processing*, vol. 57, no. 7, pp. 2690–2700, July 2009.
- [26] Z. Lei and F. Chin, "OFDM signal sensing for cognitive radios," in *Proc. Int. Symp. Personal, Indoor and Mobile Radio Commun.*, Sep. 2008, pp. 1–5.
- [27] S. Enserink and D. Cochran, "A cyclostationary feature detector," in *Proc. Asilomar Conf. on Signals, Syst., and Comput.*, vol. 2, Oct. 1994, pp. 806–810.
- [28] W. A. Gardner, A. Napolitano, and L. Paura, "Cyclostationarity: Half a century of research," *Elsevier Signal processing*, vol. 86, no. 4, pp. 639–697, Apr. 2006.
- [29] W. Zhang, R. K. Mallik, and K. Letaief, "Optimization of cooperative spectrum sensing with energy detection in cognitive radio networks," *IEEE Trans. Wireless Commun.*, vol. 8, no. 12, pp. 5761–5766, Dec. 2009.
- [30] S. Maleki, S. P. Chepuri, and G. Leus, "Optimization of hard fusion based spectrum sensing for energy-constrained cognitive radio networks," *Elsevier Physical Commun.*, vol. 9, pp. 193–198, Dec. 2013.
- [31] S. Chaudhari, J. Lundén, and V. Koivunen, "BEP walls for collaborative spectrum

- sensing,” in *Proc. IEEE Int. Conf. Acoust. Speech and Signal Processing*, May 2011, pp. 2984–2987.
- [32] FCC Spectrum Policy Task Force, “Second report and order and memorandum opinion and order,” FCC, Tech. Rep., Nov. 2008. [Online]. Available: http://hraunfoss.fcc.gov/edocs_public/attachmatch/FCC-08-260A1.pdf
- [33] —, “Second memorandum opinion and order,” FCC, Tech. Rep., Sep. 2010. [Online]. Available: http://hraunfoss.fcc.gov/edocs_public/attachmatch/FCC-10-174A1.pdf
- [34] Ofcom, “The future role of spectrum sharing for mobile and wireless data services,” Ofcom, Tech. Rep., Apr. 2014. [Online]. Available: http://stakeholders.ofcom.org.uk/binaries/consultations/spectrum-sharing/statement/spectrum_sharing.pdf
- [35] Electrical Engg. Dept., IIT Mumbai, “Affordable broadband in india using backhaul in tv white space,” Tech. Rep., 2014. [Online]. Available: <https://www.ee.iitb.ac.in/tvws/>
- [36] G. Naik, S. Singhal, A. Kumar, and A. Karandikar, “Quantitative assessment of tv white space in india,” in *Proc. Nat. Conf. Commun.*, Mar. 2014, pp. 1–6.
- [37] W. Zhang, R. Mallik, and K. Letaief, “Optimization of cooperative spectrum sensing with energy detection in cognitive radio networks,” *IEEE Trans. Wireless Commun.*, vol. 8, no. 12, pp. 5761–5766, Dec. 2009.

- [38] S. Ashrafi, M. Malmirchegini, and Y. Mostofi, "Binary consensus for cooperative spectrum sensing in cognitive radio networks," in *Proc. IEEE Global Commun. Conf.*, Dec. 2011, pp. 1–6.
- [39] P. Grover, A. Goldsmith, and A. Sahai, "Fundamental limits on the power consumption of encoding and decoding," in *Proc. IEEE Int. Symp. Inf. Theory*. IEEE, July 2012, pp. 2716–2720.
- [40] J. N. Tsitsiklis, "Problems in decentralized decision making and computation," Ph.D. dissertation, Dept. Electr. Eng. Comput. Sci., Massachusetts Inst. Technol., Cambridge, MA, Nov. 1984.
- [41] D. Kempe, A. Dobra, and J. Gehrke, "Gossip-based computation of aggregate information," in *Proc. IEEE Symp. Foundations of Comput. Sci.*, Oct. 2003, pp. 482–491.
- [42] L. Xiao and S. Boyd, "Fast linear iterations for distributed averaging," *Systems & Control Letters*, vol. 53, no. 1, pp. 65–78, Sep. 2004.
- [43] R. Olfati-Saber and R. M. Murray, "Consensus problems in networks of agents with switching topology and time-delays," *IEEE Trans. Automat. Contr.*, vol. 49, no. 9, pp. 1520–1533, Sep. 2004.
- [44] V. D. Blondel, J. M. Hendrickx, A. Olshevsky, and J. N. Tsitsiklis, "Convergence in multiagent coordination, consensus, and flocking," in *Proc. IEEE Conf. Decision and Contr.*, Dec. 2005, pp. 2996–3000.

- [45] S. Boyd, A. Ghosh, B. Prabhakar, and D. Shah, "Gossip algorithms: design, analysis and applications," in *Proc. IEEE Int. Conf. Comput. Commun.*, vol. 3, Mar. 2005, pp. 1653–1664.
- [46] —, "Randomized gossip algorithms," *IEEE Trans. Inform. Theory*, vol. 52, no. 6, pp. 2508–2530, June 2006.
- [47] B. Nazer, A. Dimakis, and M. Gastpar, "Local interference can accelerate gossip algorithms," *IEEE J. Sel. Topics Signal Process.*, vol. 5, no. 4, pp. 876–887, Aug. 2011.
- [48] A. Kashyap, T. Başar, and R. Srikant, "Quantized consensus," *Automatica*, vol. 43, no. 7, pp. 1192–1203, July 2007.
- [49] T. C. Aysal, M. Coates, and M. Rabbat, "Distributed average consensus using probabilistic quantization," in *Proc. IEEE Workshop on Stat. Signal Processing*, Aug. 2007, pp. 640–644.
- [50] S. Kar and J. M. Moura, "Distributed consensus algorithms in sensor networks: Quantized data and random link failures," *IEEE Trans. Signal Processing*, vol. 58, no. 3, pp. 1383–1400, Mar. 2010.
- [51] F. Bénézit, P. Thiran, and M. Vetterli, "Interval consensus: From quantized gossip to voting," in *Proc. IEEE Int. Conf. Acoust. Speech and Signal Processing*, Apr. 2009, pp. 3661–3664.
- [52] M. Draief and M. Vojnovic, "Convergence speed of binary interval consensus," in *Proc. IEEE Int. Conf. Comput. Commun.*, Mar. 2010, pp. 1–9.

- [53] F. Bénézit, P. Thiran, and M. Vetterli, "The distributed multiple voting problem," *IEEE J. Sel. Topics Signal Process.*, vol. 5, no. 4, pp. 791–804, Aug. 2011.
- [54] Y. Wang and P. M. Djuric, "Reaching consensus on a binary state by exchanging binary actions," in *Proc. IEEE Int. Conf. Acoust. Speech and Signal Processing*. IEEE, Mar. 2012, pp. 3297–3300.
- [55] —, "A gossip method for optimal consensus on a binary state from binary actions," *IEEE J. Sel. Topics Signal Process.*, vol. 7, no. 2, pp. 274–283, Apr. 2013.
- [56] A. Abdaoui and T. Elfouly, "Distributed binary consensus algorithm in wireless sensor networks with faulty nodes," in *Proc. IEEE GCC Conf. and Exhib.*, Nov. 2013, pp. 495–500.
- [57] J. George and A. Swami, "Binary consensus through binary communication," in *Proc. IEEE Conf. Decision and Contr.*, Dec. 2014, pp. 721–726.
- [58] R. Olfati-Saber, E. Franco, E. Frazzoli, and J. S. Shamma, "Belief consensus and distributed hypothesis testing in sensor networks," in *Proc. Networked Embedded, Sensing and Contr.* Springer, Jul. 2006, vol. 331, pp. 169–182.
- [59] Z. Li, F. R. Yu, and M. Huang, "A distributed consensus-based cooperative spectrum-sensing scheme in cognitive radios," *IEEE Trans. Veh. Technol.*, vol. 59, no. 1, pp. 383–393, Jan. 2010.
- [60] K. Chan, A. Swami, Q. Zhao, and A. Scaglione, "Consensus algorithms over fading channels," in *Proc. IEEE Military Commun. Conf.*, Nov. 2010, pp. 549–554.

- [61] Y. Mostofi, "Binary consensus with Gaussian communication noise: A probabilistic approach," in *Proc. IEEE Conf. Decision and Contr.*, Dec. 2007, pp. 2528–2533.
- [62] Y. Ruan and Y. Mostofi, "Binary consensus with soft information processing in cooperative networks," in *Proc. IEEE Conf. Decision and Contr.*, Dec. 2008, pp. 3613–3619.
- [63] Y. Mostofi and M. Malmirchegini, "Binary consensus over fading channels," *IEEE Trans. Signal Processing*, vol. 58, no. 12, pp. 6340–6354, Dec. 2010.
- [64] B. Chen, R. Jiang, T. Kasetkasem, and P. Varshney, "Channel aware decision fusion in wireless sensor networks," *IEEE Trans. Signal Processing*, vol. 52, no. 12, pp. 3454–3458, Dec. 2004.
- [65] Y. Zou, J. Zhu, B. Zheng, and Y.-D. Yao, "An adaptive cooperation diversity scheme with best-relay selection in cognitive radio networks," *IEEE Trans. Signal Processing*, vol. 58, no. 10, pp. 5438–5445, Oct. 2010.
- [66] Y. Zou, Y.-D. Yao, and B. Zheng, "Cognitive transmissions with multiple relays in cognitive radio networks," *IEEE Trans. Wireless Commun.*, vol. 10, no. 2, pp. 648–659, Feb. 2011.
- [67] K. V. K. Chaythanya, R. Annavajjala, and C. R. Murthy, "Comparative analysis of pilot-assisted distributed cophasing approaches in wireless sensor networks," *IEEE Trans. Signal Processing*, vol. 59, no. 8, pp. 3722–3737, Aug. 2011.
- [68] R. Cogburn, "The ergodic theory of markov chains in random environments,"

- Zeitschrift für Wahrscheinlichkeitstheorie und verwandte Gebiete*, vol. 66, no. 1, pp. 109–128, May 1984.
- [69] S. M. Ross, *Introduction to probability models*. Academic Press, 2006.
- [70] R. A. Horn and C. R. Johnson, *Matrix analysis*. Cambridge University Press, 1990.
- [71] D. Aldous and J. A. Fill, “Reversible Markov chains and random walks on graphs,” 2002, unfinished monograph, recompiled 2014, available at <http://www.stat.berkeley.edu/~aldous/RWG/book.html>.
- [72] C. Sandvig, “Cartography of the electromagnetic spectrum: A review of wireless visualization and its consequences,” in *Proc. Telecommun. Policy Research Conf. Commun. Information and Internet Policy*, 2006.
- [73] A. Alaya-Feki, S. Ben Jemaa, B. Sayrac, P. Houze, and E. Moulines, “Informed spectrum usage in cognitive radio networks: Interference cartography,” in *Proc. Int. Symp. Personal, Indoor and Mobile Radio Commun.*, Sep. 2008, pp. 1–5.
- [74] G. Mateos, J. Bazerque, and G. Giannakis, “Spline-based spectrum cartography for cognitive radios,” in *Proc. Asilomar Conf. on Signals, Syst., and Comput.*, Nov. 2009, pp. 1025–1029.
- [75] R. Niu and P. Varshney, “Target location estimation in sensor networks with quantized data,” *IEEE Trans. Signal Processing*, vol. 54, no. 12, pp. 4519–4528, Dec. 2006.
- [76] J. K. Nelson, M. R. Gupta, J. E. Almodovar, and W. H. Mortensen, “A quasi EM method for estimating multiple transmitter locations,” *IEEE Signal Processing Lett.*, vol. 16, no. 5, pp. 354–357, May 2009.

- [77] A. O. Nasif and B. L. Mark, "Measurement clustering criteria for localization of multiple transmitters," in *Proc. Conf. on Inform. Sci. and Syst.*, Mar. 2009, pp. 341–345.
- [78] V. Cevher, M. Duarte, and R. G. Baraniuk, "Distributed target localization via spatial sparsity," in *Proc. Euro. Signal Proc. Conf.*, Aug. 2008, pp. 1–5.
- [79] C. Feng, S. Valaee, and Z. Tan, "Multiple target localization using compressive sensing," in *Proc. IEEE Global Commun. Conf.*, Nov. 2009, pp. 1–6.
- [80] J. A. Bazerque and G. B. Giannakis, "Distributed spectrum sensing for cognitive radio networks by exploiting sparsity," *IEEE Trans. Signal Processing*, vol. 58, no. 3, pp. 1847–1862, Mar. 2010.
- [81] A. Shoari and A. Seyedi, "Localization of an uncooperative target with binary observations," in *IEEE Int. Workshop on Signal Process. Advances in Wireless Commun.*, June 2010, pp. 1–5.
- [82] S. S. Chen, D. L. Donoho, and M. A. Saunders, "Atomic decomposition by basis pursuit," *SIAM Rev.*, vol. 43, no. 1, pp. 129–159, Jan. 2001.
- [83] J. A. Tropp and A. C. Gilbert, "Signal recovery from random measurements via orthogonal matching pursuit," *IEEE Trans. Inform. Theory*, vol. 53, no. 12, pp. 4655–4666, Dec. 2007.
- [84] T. Caliński and J. Harabasz, "A dendrite method for cluster analysis," *Communication in Statistics-Simulation and Computation*, vol. 3, no. 1, pp. 1–27, 1974.
- [85] J. A. Hartigan, *Clustering algorithms*. John Wiley & Sons, Inc., 1975.

- [86] A. Goldsmith, *Wireless Communications*. Cambridge University Press, 2005.
- [87] S. P. Lloyd, "Least squares quantization in PCM," *IEEE Trans. Inform. Theory*, vol. 28, no. 2, pp. 129–137, Mar. 1982.
- [88] G. W. Milligan and M. C. Cooper, "An examination of procedures for determining the number of clusters in a data set," *Springer Psychometrika*, vol. 50, no. 2, pp. 159–179, June 1985.
- [89] M. Gudmundson, "Correlation model for shadow fading in mobile radio systems," *IET Electronics letters*, vol. 27, no. 23, pp. 2145–2146, 1991.
- [90] "IEEE 802.15.4 standard." [Online]. Available: <http://standards.ieee.org/about/get/802/802.15.html>
- [91] "Chipcon AS SmartRF CC2420 Preliminary Datasheet." [Online]. Available: <http://www.datasheetarchive.com/CC2420-datasheet.html>
- [92] M. Herman and T. Strohmer, "General deviants: An analysis of perturbations in compressed sensing," *IEEE J. Sel. Topics Signal Process.*, vol. 4, no. 2, pp. 342–349, Apr. 2010.
- [93] R. Want, A. Hopper, V. Falcao, and J. Gibbons, "The active badge location system," *ACM Trans. Inf. Sys.*, vol. 10, no. 1, pp. 91–102, Jan. 1992.
- [94] N. B. Priyantha, A. Chakraborty, and H. Balakrishnan, "The cricket location-support system," in *Proc. ACM Int. Conf. Mob. Comp. Net.*, Aug. 2000, pp. 32–43.
- [95] A. Ward, A. Jones, and A. Hopper, "A new location technique for the active office," *IEEE Pers. Commun.*, vol. 4, no. 5, pp. 42–47, Oct. 1997.

- [96] Crossbow Technology, Inc., "Micaz mote data sheet." [Online]. Available: http://www.openautomation.net/uploadsproductos/micaz_datasheet.pdf
- [97] "Estimote beacons." [Online]. Available: <http://estimote.com/api>
- [98] L. M. Ni, Y. Liu, Y. C. Lau, and A. P. Patil, "LANDMARC: indoor location sensing using active RFID," *Springer Journ. Wireless Netw.*, vol. 10, no. 6, pp. 701–710, Nov. 2004.
- [99] P. Bahl and V. N. Padmanabhan, "RADAR: An in-building RF-based user location and tracking system," in *Proc. IEEE Int. Conf. Comp. Commun.*, Mar. 2000, pp. 775–784.
- [100] M. Youssef and A. Agrawala, "The HORUS WLAN location determination system," in *Proc. ACM Int. Conf. Mobile Sys. Appl. Serv.*, June 2005, pp. 205–218.
- [101] N. Bulusu, J. Heidemann, and D. Estrin, "GPS-less low-cost outdoor localization for very small devices," *IEEE Pers. Commun.*, vol. 7, no. 5, pp. 28–34, Oct. 2000.
- [102] T. He, C. Huang, B. M. Blum, J. A. Stankovic, and T. Abdelzaher, "Range-free localization schemes for large scale sensor networks," in *Proc. ACM Int. Conf. on Mob. Comp. Netw.*, Sep. 2003, pp. 81–95.
- [103] V. Vivekanandan and V. W. Wong, "Concentric anchor beacon localization algorithm for wireless sensor networks," *IEEE Trans. Veh. Technol.*, vol. 56, no. 5, pp. 2733–2744, Sep. 2007.
- [104] R. Faragher and R. Harle, "Location fingerprinting with bluetooth low energy beacons," *IEEE J. Select. Areas Commun.*, vol. 33, no. 11, pp. 2418–2428, Nov. 2015.

- [105] C. L. Chan, S. Jaggi, V. Saligrama, and S. Agnihotri, "Non-adaptive group testing: explicit bounds and novel algorithms," *arXiv preprint arXiv:1202.0206*, 2012.
- [106] R. Dorfman, "The detection of defective members of large populations," *The Annals of Mathematical Statistics*, vol. 14, no. 4, Dec. 1943.
- [107] J. G. Andrews, R. K. Ganti, M. Haenggi, N. Jindal, and S. Weber, "A primer on spatial modeling and analysis in wireless networks," *IEEE Commun. Mag.*, vol. 48, no. 11, pp. 156–163, Nov. 2010.
- [108] P. V. Hall, *Introduction to the Theory of Coverage Processes*. John Wiley and Sons, Inc., 1988.
- [109] H. A. David and H. N. Nagaraja, *Order Statistics*. John Wiley and Sons, Inc., 2003.
- [110] A. Manesh, C. R. Murthy, and R. Annavajjala, "Design and analysis of distributed co-phasing with arbitrary constellations," in *Proc. IEEE Int. Conf. Commun.*, Jun. 2013, pp. 5780–5785.
- [111] —, "Physical layer data fusion via distributed co-phasing with general signal constellations," *IEEE Trans. Signal Processing*, vol. 63, no. 17, pp. 4660–4672, Sep. 2015.
- [112] I. S. Gradshteyn and I. M. Ryzhik, *Table of integrals, series, and products*. Academic Press, 2007.

-
- [113] J. R. Weaver, "Centrosymmetric (cross-symmetric) matrices, their basic properties, eigenvalues, and eigenvectors," *The American Mathematical Monthly*, vol. 92, no. 10, pp. 711–717, Dec. 1985.